1986

Electrochemistry of stress corrosion cracking of brass

M. Moustafa Said Seleet
Iowa State University

Recommended Citation

Seleet, M. Moustafa Said, "Electrochemistry of stress corrosion cracking of brass " (1986). *Retrospective Theses and Dissertations*. 8038.
https://lib.dr.iastate.edu/rtd/8038

INFORMATION TO USERS

This reproduction was made from a copy of a manuscript sent to us for publication and microfilming. While the most advanced technology has been used to photograph and reproduce this manuscript, the quality of the reproduction is heavily dependent upon the quality of the material submitted. Pages in any manuscript may have indistinct print. In all cases the best available copy has been filmed.

The following explanation of techniques is provided to help clarify notations which may appear on this reproduction.

1. Manuscripts may not always be complete. When it is not possible to obtain missing pages, a note appears to indicate this.
2. When copyrighted materials are removed from the manuscript, a note appears to indicate this.
3. Oversize materials (maps, drawings, and charts) are photographed by sectioning the original, beginning at the upper left hand corner and continuing from left to right in equal sections with small overlaps. Each oversize page is also filmed as one exposure and is available, for an additional charge, as a standard 35mm slide or in black and white paper format.*
4. Most photographs reproduce acceptably on positive microfilm or microfiche but lack clarity on xerographic copies made from the microfilm. For an additional charge, all photographs are available in black and white standard 35mm slide format.*

*For more information about black and white slides or enlarged paper reproductions, please contact the Dissertations Customer Services Department.

UMI University Microfilms International

8615086

Seleet, M. Moustafa Said

ELECTROCHEMISTRY OF STRESS CORROSION CRACKING OF BRASS

Iowa State University PH.D. 1986

University
Microfilms
International 300 N. Zeeb Road, Ann Arbor, MI 48106

Electrochemistry of stress corrosion cracking of brass

by

M. Moustafa Said Seleet

A Dissertation Submitted to the
Graduate Faculty in Partial Fulfillment of the
Requirements for the Degree of
DOCTOR OF PHILOSOPHY

Department: Chemistry
Major: Physical Chemistry

Approved:

Signature was redacted for privacy.

In Charge of Major Work

Signature was redacted for privacy.

For the Major Department

Signature was redacted for privacy.

For the Graduate College

Iowa State University
Ames, Iowa

1986

TABLE OF CONTENTS

INTRODUCTION

Stress Corrosion Cracking of Brass in Ammoniacal Solutions

The brass industry has been troubled since its beginning with the stress corrosion cracking (SCC) of various forms of brass. SCC was called "season cracking" because of its resemblance in appearance to the cracking of wood during seasoning; however, this term is misleading since SCC is a result of internal strains localized in effect by corrosive action [1]. It was known that brasses stored in a dry, and clean atmosphere, although carrying high internal strains, cracked only after a long time, while a damp atmosphere was especially active in producing such cracking, particularly if it carried ammonia vapor from decaying organic matter [2]. Past experience indicated also that cracking was more frequent in brasses carrying a higher percent of zinc, Zn. The effect of Zn-content on the number and kind of phases in brass alloy is shown in the phase diagram of brass, Figure 1. Although it has been generally accepted that corrosion is an inevitable factor, the few articles that appeared in the beginning of this century were all devoted to studying the effect of internal stresses and how to release them [3,4]. Thompson and Tracy [5] observed that the addition of zinc, phosphorous, arsenic, antimony, silicon, nickel or aluminum to copper results in alloys that are subject to SCC in a moist ammoniacal atmosphere. They identified two modes of cracking, intercrystalline and transcrystalline. However, no failure mechanisms were discussed.

Extensive systematic study of SCC of brass was initiated by Mattsson's work, published in 1961 [6]. By that time, the potential/pH diagrams were introduced by Pourbaix [7]. The potential/pH diagram of a certain metal, in some systems, defines the stability regions of different possible forms of this metal produced by its possible chemical and electrochemical reactions with the system at different values of potential and pH. The theoretical basics of the potential/pH diagram construction are discussed in Appendix A. The potential/pH diagrams for most of the elements were constructed by Pourbaix; however, it is important to note that they are restricted to binary systems of pure elements with water, e.g., $Cu-H_2O$, $Zn-H_2O$. So, where additional species (e.g., NH_3, CN^-) are present, the potential/pH diagram must be modified to include the possible reactions of these species with the element under consideration.

Mattsson [6] constructed the potential/pH diagrams for the ternary systems: $Cu-NH_3-H_2O$ and $Zn-NH_3-H_2O$ (Figures 2a,b). He used these diagrams to explain his observations of the relationship between the time-to-crack of brass samples in ammoniacal copper sulphate solutions and the pH of the solution. The chemical reactions used by Mattsson to construct the potential/pH diagrams are shown in Appendix B. To initiate the brass cracking, stress was created in the brass samples by shaping them into loops, where only the outer surface of the loop was under tensile stress. The disadvantage of the loop method, used also by Thompson [8], is the inability to determine or vary the applied stresses.

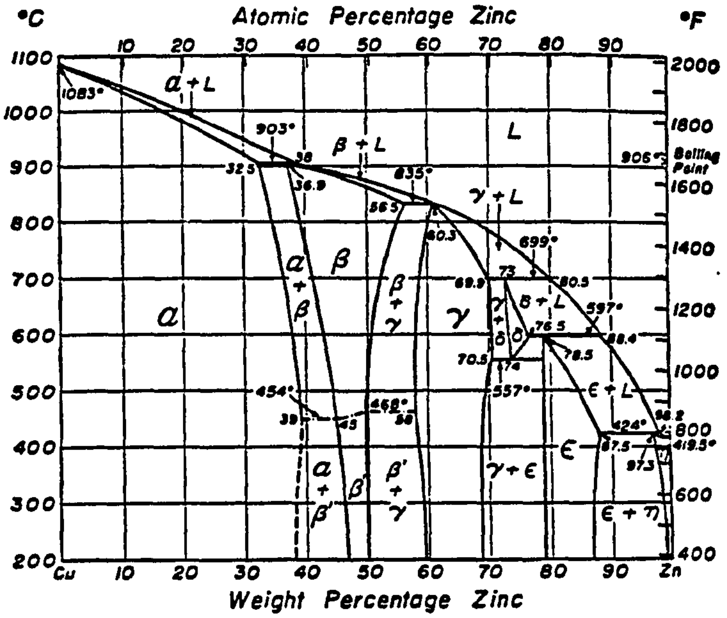

Figure 1. Phase diagram of copper-zinc alloys

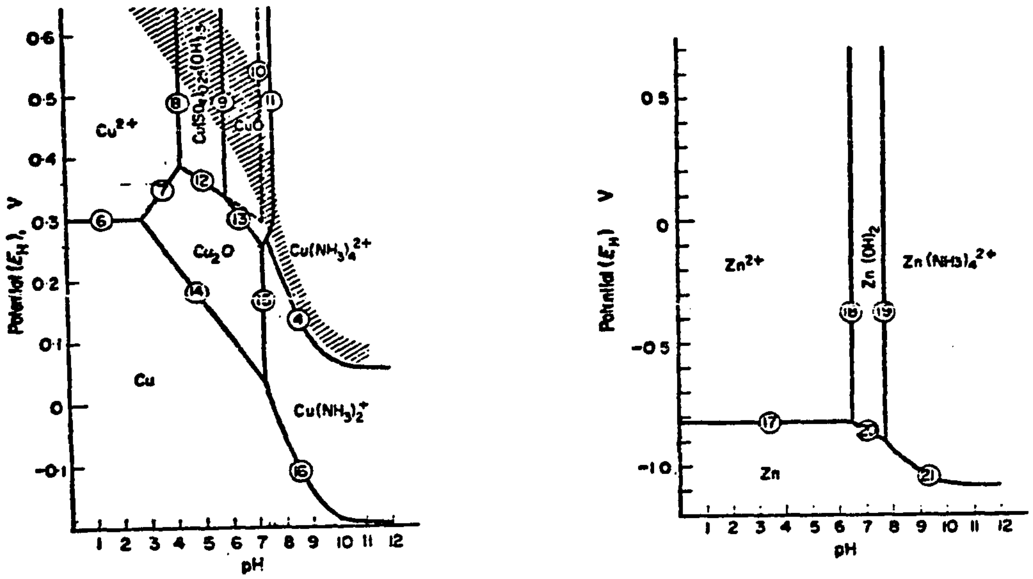

a b

a. $Cu-NH_3-H_2O$ system

b. $Zn-NH_3-H_2O$ system

Figure 2. Potential/pH diagram of ternary systems containing 1 g mole NH_3 and 0.05 M $CuSO_4$ at 25°C [6]

The brass (63 Cu-37 Zn) loops were immersed in solutions of different pH and observed visually for crack appearance. All the solutions had the same composition of 1 g-mole of NH_3 [added as NH_3 solution or $(NH_4)_2SO_4$, in proper ratio to adjust the required pH] + 0.05 g-atom/L of Cu, added as $CuSO_4 \cdot 5\ H_2O$. Mattsson identified two kinds of solutions, tarnishing and nontarnishing, according to the appearance of the sample after the test. In tarnishing solutions, $6.3 \leq pH \leq 7.3$, a black surface coating of Cu_2O was observed. Time-to-cracking, t_c, was found to decrease with increasing pH, passing through a minimum at pH=7.3; however, no cracking was identified at pH=2. The cracking mode was intergranular in tarnishing solutions, and transgranular in nontarnishing solutions [$3.9 \leq pH \leq 5.5$ and $7.7 \leq pH \leq 11.2$]. The anodic reaction was assumed to be zinc dissolution at all pH values, in addition to copper dissolution at $7.8 \leq pH \leq 11.2$. The cathodic reaction was supposed to be the reduction of Cu^{2+}-complexes at pH values where these complexes are stable, and the reduction of Cu^{2+}-ions elsewhere. Hoar and Scully [9] observed the importance of yielding of the metal (upon stress) for the appearance of a large increase in dissolution current, and postulated an electrochemical mechanism for the SCC propagation. Takano and Shimodaira [10] observed the SCC of α-brass (70/30) in Mattsson's solutions at pH=7.4, but not at pH=2.0 or 10.0. They suggested that the cracking observed by Mattsson at pH=10.0 was due to mechanical failure caused by the thinning of the sectional area of the specimen by severe corrosion. This is supported by the fact that the rate of potential drop of the redox potential at that pH was the highest value reported by Mattsson indicating the destruction of air-formed film and exposure of bare metal to more dissolution [11]. The general corrosion at high pH values was also confirmed by Hoar and Booker [12]. The authors also proposed that the tarnish film was the result of anodic dissolution of zinc from the heavily cold-worked surface, and the anodic conversion of the "activated" porous copper into Cu_2O. Polarization measurements showed that the tarnish film had a more inhibiting effect on corrosion, but a more favorable one on SCC. It was also found that stresses lower than the yield stress still caused cracking at longer times, which was disputed by Logan [13], who assumed that stresses should be higher than the yield stress for SCC to occur.

To account for crack initiation, the authors [12] suggested that very narrow zones of stressed "disarranged metal" dissolve anodically in preference to stressed "well-ordered" metal, to produce sub-microscopic fissures which act as local stress raisers. At $5 \leq pH \leq 7.4$, it is probable that the concomitant oxide film formation hinders such preferential dissolution from the body of the grain far more than at the grain boundaries, which thus become the major points of crack initiation, leading to intergranular cracking. Moreover, Zn emergence is very high in cold-worked metal, since Zn diffusion is easier than in annealed metal. Thus, any point on the surface, where micro-localized cold work has occurred, will (in early stages of corrosion) become poor in Zn and rich in disarranged Cu, whereby further mechanical deformation of weakened metal (under stress) occurs, and anodic oxidation of Cu into Cu_2O will be much stimulated. Finally, when local stresses at the bottom of the sub-microfissure increase, yielding at the advancing edge of the crack will occur, leading to:

a. Stimulation of anodic emergence of Zn

b. Mechanical fracture and anodic oxidation of the remaining Cu

c. Disruption in the Cu_2O film

d. Provision of a supply of easily anodically attacked material, from the freshly produced metal surface

Therefore, several factors will assist a metal atom at the advancing edge (and not at the crack side) to leave, therefore, propagation of the crack occurs. Although Hoar and Booker [12] used Mattsson's potential/pH diagrams after revising them; Johnson and Leja [14] relocated the stability regions of CuO, Cu_2O, and $Zn(OH)_2$ on the diagram, and Lahiri [15] suggested the presence of a second stability region for Cu_2O at higher pH.

Hoar et al. [16] confirmed the second stability region of Cu_2O at a higher pH value. They revised the potential/pH diagram for the second time, taking into consideration the oxidation of NH_3 to NO_2^- ion, and found that simultaneous production of solid Cu_2O and soluble $Cu(NH_3)_2^+$ was also allowed at pH=11.5, in addition to the previously known formation at $7.2 \leq pH \leq 7.4$

The authors concluded that the bright black film formed on brass (and not on pure Cu) in solutions containing Cu^{2+} ions (and not in absence of Cu^{2+} ions) and at the specific pH range, $6.4 \leq pH \leq 7.3$, was "nearly amorphous, nonstoichiometric cuprous oxide doped with Zn."

The use of potential/pH diagrams of pure metals to predict the behavior of alloys was not restricted to α-brass, but extended to other cases, e.g., copper-nickel alloys, where the superimposed potential/pH diagrams of both Cu and Ni were used to interpret the behavior of their alloys [17]. However, the superposition technique was disputed by some authors [18], on the basis that pure metals behave differently in the alloyed state.

Pugh and Westwood [19] prepared solutions of concentrated aqueous ammonia (~15 N) containing various concentrations of cupric complex ions to avoid the tendency of Mattsson's solutions to form precipitates (basic copper sulfate). Two compositions of Pugh solutions have been used:

1) Tarnishing solutions containing 8 g/L of Cu-powder in 15 N aqueous ammonia
2) Nontarnishing solutions containing 1 g/L of Cu-powder in 15 N aqueous ammonia

The authors assumed that in oxygenated ammoniacal solutions the dissolution of Cu takes place through the autocatalytic reaction:

$$\begin{tikzcd}
[Cu(NH_3)_5]^{2+} + Cu_{surface} \arrow[r] & 2[Cu(NH_3)_2]^{+} + NH_3 \arrow[d, "+ O_2 + NH_3"] \\
 & 2[Cu(NH_3)_4]^{2+}
\end{tikzcd}$$

The important role of Cu^{2+}-complexes in SCC process was discussed by several authors [20-22].

In his first review, Pugh [23] summarized the dissolution process and SCC mechanisms of α-brass in both tarnishing and nontarnishing aqueous ammoniacal solutions. Cracking in tarnishing solutions was supposed to occur discontinuously by the repeated formation and rupture of the tarnish film. In nontarnishing solutions the cracking mechanism was proposed to involve failure by a single-stage process involving preferential anodic dissolution at dislocations created by the applied stress.

The structure and mechanism of formation of the tarnish film was first studied by Forty and Humble [24], who stressed the important role of tarnish film, consisting mainly of Cu_2O, in the SCC process. McEvily and Bond [25] concluded that a localized cracking process would be avoided if the film formed is nonprotective so it would permit general corrosion to occur instead of a localized attack, or is strong enough to sustain the applied stress without rupturing. Although the kinetics and role of tarnish formation were further studied by many authors [26-36], Jenkins and Durham [37] were the first to identify a more protective thin film on α-brass, by electron diffraction, prior to the tarnish layer formation. Leidheiser and Kissinger [38] analyzed the liquid within the propagating crack, using the technique developed by Brown et al. [39], and observed a very high Zn content, indicating more Zn dissolution at the crack tip. They also observed that the internal surfaces of the crack were covered by a thin film, which decreased in thickness from the outer surface to the crack tip. The absence of a tarnish film at the crack tip conflicted with the idea that SCC is a consequence of the formation of a brittle oxide which repetitively cracks once it reaches appreciable thickness. This conflict was further stressed by other authors [40,41]. It may be useful at this point to differentiate between the "tarnish film" and the "thin film." The "tarnish film" is a film resulting in a visible discoloration of the metal surface, and therefore has a thickness of the order of (or greater than) the wavelength of light. The "thin film" is a film not resulting in visible discoloration, therefore, detectable by means other than visual observation, e.g., electrochemical means, Auger spectroscopy, ellipsometry, or electron diffraction. The tarnish film and the thin film may have the same composition, e.g., Cu_2O.

The formation of a thin film before the tarnish layer (Figure 3) was confirmed by Pinchback et al. [42], who used Auger electron spectroscopy (AES) to show that a thin oxidized layer penetrated to the leading edge (Figure 3) of the stress corrosion crack formed in α-brass (70/30) exposed to Pugh's tarnishing solution. The formation of a thicker tarnish film, depleted in Zn, trailed well behind the leading edge, thus, playing no apparent role in crack propagation. No bulk depletion of Zn was detected in the alloy at the stress corrosion crack leading edge, and no evidence was found for the discontinuous crack propagation observed before.

The formation of Cu_2O oxide film, depleted in Zn, on α-brass exposed to Pugh's tarnishing solution was also found by Gabel et al. [43], who proposed a dissolution-precipitation mechanism where both Cu and Zn dissolved at the metal-tarnish interface, then a part of Cu reprecipitated as Cu_2O, while the ions of Zn diffused through the porous film to the bulk solution. An outer layer of CuO was found in specimens exposed for long periods.

In Pugh's nontarnishing solution, Pinchback et al. [44] found that the fracture surfaces in α-brass (70/30) were brass colored, and the cleavage-like features extended to the site of crack initiation, thus, characterizing the entire SCC surface and challenging the dissolution model proposed before, for this case. Preferential zinc dissolution was observed on SCC surfaces; but no evidence was found for oxide formation.

At this point, it may be relevant to summarize the present understanding of SCC process according to Pugh's second review [45] and the latest publications.

In tarnishing solutions

Tarnish film formation The tarnish formation is not a single stage as thought before, but involves several steps:

1) The formation of a thin protective film of Cu_2O (~ 200 Å). The onset of tarnishing was indicated by active-passive transition in the anodic polarization curves.
2) local breakdown of the thin film leading to rapid anodic dissolution of the substrate and the precipitation of a thick porous layer of Cu_2O. The breakdown was indicated by the increasing currents at larger anodic potentials.
3) The formation of an outer layer of CuO (of thickness > 5 μm).

While the growth kinetics of the film were not strongly dependent on Zn content, the rate of film breakdown increased with increasing Zn content, as was indicated by higher currents at more anodic potentials. Recent observations [46-49] are in accordance with the above mechanism.

Mechanisms of cracking The intergranular mode of failure is common in all alloys in the annealed conditions, while transgranular failure is observed in the heavily worked Cu-30 Zn alloy.

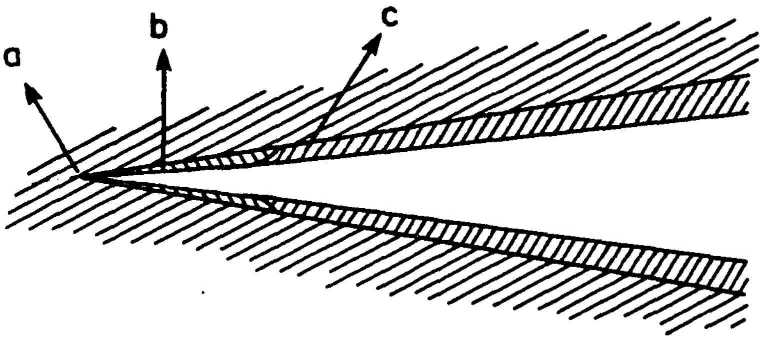

a. Crack tip
b. Thin film
c. Tarnish film

Figure 3. Simplified diagram of a stress corrosion crack and surface films formed in tarnishing solutions

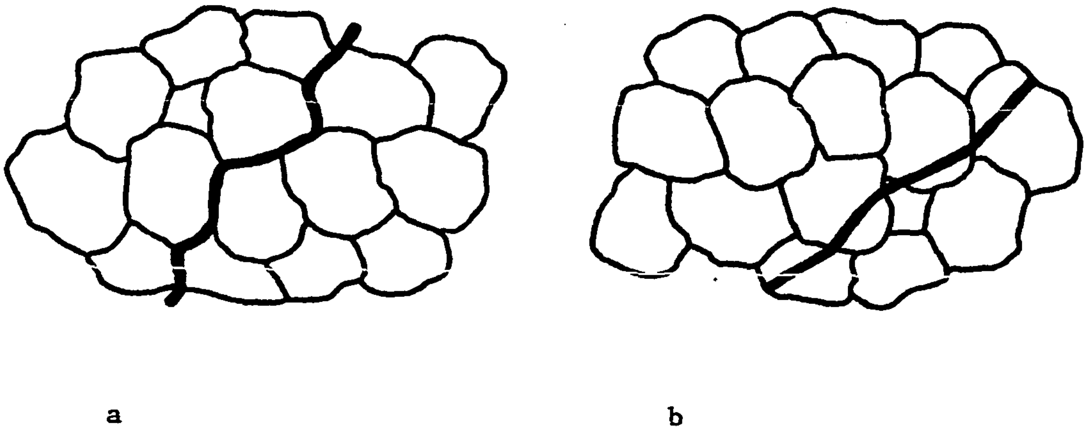

a. Intergranular
b. Transgranular

Figure 4. Different modes of stress corrosion cracking [11]

Mechanism of intergranular cracking The repeated tarnish formation-rupture mechanism is modified by replacing the thick film by the protective film, which is in fact present at the crack tip. A competition is envisioned between anodic dissolution and repassivation at the crack tip, and the potential should be high enough to allow rapid anodic dissolution at the crack tip, as well as the formation of a surface layer apart from the tip, but not so high that passivation of the crack tip occurs. This condition, fulfilled only by certain environments, accounts for the specific nature of solutions causing SCC. The dependence of SCC susceptibility on Zn content (time-to-fracture decreases with increasing Zn content) can be attributed to the zinc effect on the two processes of anodic dissolution and repassivation.

The structure and composition of grain boundaries might cause slower repassivation kinetics at the grain boundaries than at the grain surfaces (Figure 4a), leading to an intergranular cracking path. So, the slower repassivation kinetics is the main cause, and intergranular penetration is its secondary effect. However, intergranular penetration may play an important role in crack initiation.

Mechanism of transgranular cracking This is supposed to be the same as the transgranular cracking (Figure 4b) in nontarnishing solutions, which will be dealt with later.

In nontarnishing solutions

Dissolution process The system is under concentration polarization, where anodic dissolution rates of Cu and Zn are determined by the transport of the predominant cathodic species, ex. $[Cu(NH_3)_4]^{2+}$ to the surface. Brown, loosely-adherent, and nonprotective films are commonly observed; however, the origin of these films has not been established. Large rates of active anodic dissolution are possible, producing faceted surfaces. No preferential Zn dissolution was observed on a macroscopic scale, but the possibility of shallow dezincified layers exists. Pinchback et al. [44] provided evidence for dezincification at the transgranular stress corrosion fracture surfaces; however, no studies have been made on unstressed samples.

Mechanisms of cracking According to the dissolution model proposed before, cracking occurs when stressed samples undergo rapid anodic dissolution. While the cupric complex ions are necessary to provide a sufficiently rapid dissolution rate at open circuit potentials, the presence of these complex ions is not essential if anodic potentials are applied. Finally, the preferential dissolution at dislocations (cellular or planar) will lead to either intergranular or transgranular cracking. However, it is difficult to reconcile this dissolution model with the observation of cleavage-like features of the entire SCC surface reported [44,50-51]. If transgranular failures occur by brittle mechanical fracture, the cause of embrittlement can be attributed to one of the following models:

1) The adsorption model: in which species adsorb and interact with strained bonds at the crack tip, causing reduction in bond strength and permitting brittle fracture [52-56].

2) H_2-embrittlement model: as in other stress corrosion failures which exhibit cleavage-like fracture surfaces;

however, the hydrogen source is not evident in the case of α-brass. Although the anodic reaction:

$$Cu + 2NH_4^+ = [Cu(NH_3)_2]^+ + 2H^+ + e$$

was supposed [57]; no evidence of hydrogen evolution was found during dissolution or cracking. Bertocci [58] discussed the hydrogen embrittlement model recently, but without drawing any decisive conclusions.

3) Dezincification model: which might produce an embrittled zone at the crack tip, leading to a discontinuous brittle fracture. Dezincification was evident at transgranular stress corrosion fracture surfaces [44].

Cleava[illegible]ike fracture has been observed in heavily cold-worked Cu-30 Zn in tarnishing solutions, and the mechanism seems to be the same as before. However, the fracture surfaces in cold-worked specimens exhibit parallel markings, suggesting discontinuous cracking, which has not been reported in the nontarnishing case. Actually, if failure is due to cleavage, then discontinuous propagation should be expected, since cleavage cracks propagate at velocities of sound waves, whereas the overall rate of transgranular cracking is relatively small. A discontinuous model of cracking is consistent with H_2-embrittlement and dezincification, but not with adsorption, where continuous cracking at a rate controlled by critical species transport to the crack tip, is predicted.

In the case of intergranular cracking in nontarnishing solutions, the actual mechanism is not known. If it is assumed to be the same as in transgranular cracking, then the change in the crack path can be related to the dislocation behavior. The occurrence of intergranular SCC of unalloyed copper in nontarnishing solutions rules out the dezincification model for that case at least. Moreover, if a discontinuous fracture surface can be detected, the only possible mechanism will be the hydrogen embrittlement one. It is interesting to note that the cleavage-like features, which led to the rejection of the dissolution model, have as yet received little attention.

Stress Corrosion Cracking of Brass in Nonammoniacal Solutions

Although SCC of α-brass has been investigated mainly in Mattsson's and Pugh's ammoniacal solutions, failure in nonammoniacal solutions has also been reported. During his investigation of SCC of α-brass in ammoniacal $CuSO_4$ solutions, Mattsson [6] observed that ammonia was not included in the cracking mechanism in the pH range 3.9-4.7, where no cupric ammine complex was stable, and cathodic reaction appeared to be the reduction of Cu^{2+} ions. To confirm this, Mattsson investigated the behavior of α-brass in the same pH range of a solution in which NH_4^+ was replaced by Na^+ ion. He observed transgranular microcracks after 160 hours, compared to visual transgranular cracks after 60-100 hours in ammoniacal solution, and concluded that, in ammoniacal solutions, ammonia had a stimulating effect.

Green and Pugh [59] investigated the SCC of α-brass, using ellipsometric techniques, in citrate and tartrate solutions at pH 10.3 and 13.5, respectively. Intergranular cracking, formation of Cu^{2+}

complex ions, and formation of tarnish films indicated the similarity to SCC in tarnishing ammoniacal $CuSO_4$ solutions. Ellipsometric techniques, which measure the average rate of tarnish growth on the grain surface, could not provide a direct indication of the SCC behavior, since SCC susceptibility is related to the degree of intergranular penetration by the tarnish film.

Pickering and Byrne [60] reported the SCC of Cu-30 Zn in acid sulfate solution (1 N $Na_2SO_4 + 0.01$ N H_2SO_4) at pH=2.0 during elongation. The fracture path was mainly along grain boundaries, with some secondary cracking through the grains. They concluded that ammonium and Cu^{2+} complex ions were not necessary for SCC of brass. However, the test was conducted on Cu-30 Zn specimens anodically polarized at 0.24 V (SHE) and not at open circuit potential. In the presence of anodic dissolution, Cu^{2+} complex ions are not essential, since their role at open circuit potential is to provide an efficient cathodic reaction, hence, promoting a rapid anodic dissolution. Moreover, the authors admit that the occurrence of SCC in these experiments most likely stems from the application of dynamic, rather than static loading. A partial check of this was done by straining a specimen to a fixed deformation, then exposing it to the test solution, with all other conditions fixed. In this case, no cracking was observed. Generally, the dynamic loading is a more severe test for SCC than the static one.

The susceptibility of admiralty brass (71 Cu-28 Zn-1 Sn) to SCC in 1 N Na_2SO_4 solution was tested over a pH range of $1.3 \rightarrow 12.7$ by

Kawashima et al. [61] at open circuit potential and anodic polarization conditions, but using the dynamic technique of slow-strain rate at 1.5 x 10^{-5} sec^{-1}. They showed that admiralty brass was less susceptible to SCC than Cu-30 Zn, since no SCC of admiralty brass was observed under the same conditions (pH=2 and 240 mV_H) for which Cu-30 Zn cracked [60]. Moreover, SCC was not observed in any of the specimens tested at open circuit potential. The authors assumed that the crack velocity at open circuit potential might be so small that no detectable penetration occurred in the time of the experiment. A slower strain rate might have allowed more time for crack penetration. This assumption supports the idea of using a constant load technique (static technique) in SCC studies. On the other hand, SCC occurred at anodic potentials, where the overpotential value varied with the pH, and minimum overpotential was required in the range $4 \leq pH \leq 10$. The cracking mode was always transgranular with considerable branching, especially at high anodic potentials. Cracking severity decreased with a decrease in sulfate ion concentration, and no cracking occurred at a concentration of 10^{-4} N. The conclusion was that SCC of admiralty brass occurred in nonammoniacal solutions over a wide range of pH depending on the oxidizing conditions produced by anodic polarization. The increase in severity with increasing potential favors anodic dissolution, rather than H_2-embrittlement, as the cause of cracking. Since the sample was annealed and zinc content was higher than 18%, and observed cracking was transgranular, then the solution should be nontarnishing.

However, the authors did not refer to the presence of the brown, nonprotective film usually formed in these cases.

Admiralty brass was again tested for SCC in aq. $CuSO_4$ solution by Pinchback et al. [62]. Admiralty tube specimens were totally immersed in different concentrations (0.05 → 0.5 M) of aq. $CuSO_4$ solution at room temperature with no external stress for 500 hours. All specimens developed transgranular cracks during the test period. The SCC fracture surfaces showed cleavage-like features, as observed before for α-brass in nontarnishing ammoniacal solutions, in conflict with the dissolution mechanism. Auger electron spectroscopy (AES) revealed a higher concentration of Sn (~5 times higher) at the leading edge of the SCC than on either the mechanical fracture or the brown filmed area. Inert gas ion sputtering near the crack leading edge showed the Sn rich layer to be about 100 atomic layers thick. Since Sn is known to be an effective catalyst poison for H_2-recombination reaction, and the SCC surface showed cleavage-like features, the authors proposed that a H_2-embrittlement mechanism was operating. However, no explanation was given for the origin of high Sn concentration at the crack leading edge. Possible reasons mentioned were the segregation of Sn, or the redeposition of dissolved Sn near the crack leading edge. Sn was found to form a SnO_2 layer in admiralty brass immersed in oxygenated acidic NaCl solution, in addition to a solid solution of Cu and Sn (Stannate, or $CuSnO_3$) [63]. While selective dissolution of the electronegative components of the alloy (Zn and Sn) takes place in the initial stage, the uniform dissolution of the alloy sets in afterwards [64].

Syrett and Parkins [65] studied the effect of different concentrations of Sn or As on the SCC behavior of α-brass (80/20) in Mattsson solutions. It was found that the addition of Sn or As increased the resistance of α-brass to SCC, and the mode of cracking changed gradually from intergranular to transgranular with increasing percentage of Sn or As. At pH=7.3, an adherent black Cu_2O coating was formed in most cases, while at pH=11.3 every specimen had two surface films, one completely covering the other. The outer coating, white or light grey, was only weakly adherent and could be rubbed off the underlying, dark-colored coat with ease. The outer film is suggested to consist largely of ZnO or $Zn(OH)_2$, possibly with oxides of Sn or As. The potential-time curves showed a smooth rise in potential in the first 20 minutes of immersion for 80/20, 1% Sn, and 0.7% As alloys, but the higher Sn and As brasses showed an arrest or fall in potential during the same period, indicating more resistance to SCC. The authors suggested that Sn or As affected the film formation or character to such an extent that sites within the grains became as susceptible as the grain boundaries, so the cracking mode changed from an intergranular to transgranular one. No data were available for the concentration changes of Cu, Zn and Sn along the crack path, and accurate compositions of formed coatings were not given.

Kawashima et al. [66] investigated the SCC of admiralty brass (71 Cu-28 Zn-1 Sn-0.06 As) in several nonammoniacal solutions at pH = 8. The SCC susceptibility was found to decrease in the order

$NO_2^- > NO_3^- > ClO_3^- > SO_4^{--} > MoO_4^{--} > Cl^- > WO_4^{--}$, with no actual cracking in HCO_3^-, $B_4O_7^{--}$, CrO_4^{--}, and HPO_4^{--} solutions. All the tests were conducted at a controlled anodic potential of 300 mV_H and the authors used the dynamic test (slow strain rate technique). The potential of 300 mV_H was chosen due to its proximity to the Cu_2O/CuO equilibria in neutral solutions ($6<pH<8$) on the Pourbaix diagram. The cracking was always transgranular with considerable branching in SO_4^{--}, NO_3^-, and NO_2^- solutions. Anodic polarization curves suggested an active dissolution of the metal in aggressive solutions, while early passivation of the metal took place in other solutions where no SCC was observed.

Gouda et al. [67] reported intergranular SCC of α-brass (72/78) in 1 M, 0.1 M $NaClO_3$ solution at open circuit potential, and transgranular SCC at anodic potentials, using constant strain rate technique. In a less concentrated solution (0.01 M), anodic polarization was required and the cracking mode was transgranular. A discontinuous dezincified layer was formed in stressed specimens in relatively concentrated solutions, especially under anodic polarization. The authors suggested a mechanism of conjoint processes based on dissolution and/or embrittlement models. Similar SCC results were also reported by Maria and Scully [68]. Burstein and Newman [69] reported the susceptibility of α-brass to SCC in 1 M nitrite solution due to the reduction of NO_2^- to NH_4^+ which accumulates within the cracks. Later, Newman and Sieradzki [70] used the acoustic emission technique to confirm the discontinuous nature of the TGSCC of brass in 1 M $NaNO_2$ solution. The transgranular mode of cracking was also reported by Alvarez et al. [71].

Electrochemical polarization technique was used, in few instances, as a tool to predict SCC in different solutions. Since the reaction rate at the crack tip is considerably faster than those at all other exposed surfaces, then the activity of the crack tip and sides can be reflected in differences in currents obtained in fast (~ 1 V/min) and slow (~ 10 mV/min) sweep rate potentiokinetic polarization measurements. SCC is predicted to occur in the potential range where the current values differ by ~1 mA/cm^2 in the two sweeps. Although accurate predictions of the potential range in which SCC occurred was better achieved with rapid straining electrode tests than with potentiokinetic measurements, the latter were useful in giving the first indication of crack susceptibility. Parkins and Holroyd (72), using this technique, showed that α-brass (70/30) was susceptible to cracking in solutions of sodium acetate, formate, tartrate and hydroxide, in certain ranges of potential and pH. Intergranular cracking was observed when the potential and pH employed fell within the stability domain of Cu_2O. At higher potentials, transgranular cracking was observed.

Stress Corrosion Cracking of Pure Copper

Pugh et al. [73] were the first to report the SCC of pure Cu in nontarnishing ammoniacal solutions containing large concentration of Cu-complexes (15 N oxygenated aqueous ammonia + 2.5 g/L Cu-powder) using the constant load technique. No tarnishing of the sample was observed, and the failure was partially intergranular and partially transgranular (ductile). However, pure copper didn't undergo SCC under constant load in tarnishing solutions [5,74]. The report of SCC of pure Cu in nontarnishing solutions [73] was later disputed by Uhlig and Duqette [75], who observed intergranular corrosion with an average penetration equal in depth on the specimen surface away from, as well as at the region of maximum strain, and also equal in depth on the compression side. They concluded that the failure reported by Pugh et al. was the result of intergranular corrosion in which the grain boundaries were deeply etched on both sides of the foil used. Later, Escalante and Kruger [76] reported the intergranular SCC of pure Cu at constant load, in Cu-acetate, but not in Cu-sulfate solution. The solution was found to be tarnishing, and the brittle film rupture mechanism was assumed. Pednekar et al. [77] reported the failure of commercially pure Cu in naturally aerated 1 M $NaNO_2$ solution, using the slow strain rate technique. The solution should be tarnishing since Cu_2O film was detected on the crack sides; however, the cracking mode was transgranular. The authors proposed film rupture and anodic dissolution at the slip steps as the cracking mechanism. Similar results were reported by Suzuki and Hisamatsu [78], who observed the transgranular SCC of pure Cu under constant load stress in dilute ammoniacal solutions. A thick tarnish film of Cu_2O was formed, and the brittle tarnish rupture mechanism was assumed. It is apparent that the literature dealing with SCC of pure copper is characterized by many conflicting experimental results and correspondingly conflicting interpretations.

Summary of Stress Corrosion Cracking Studies: The Unsolved Problems

During the early studies of SCC of brasses in ammoniacal solutions, the constant load technique and open circuit potential state were the most favored experimental conditions. The SCC of brass has been well-observed in Mattsson's and Pugh's solutions, where the anions are sulfate or hydroxide; however, there was no systematic study on the effect of different anions of ammonium salts on the SCC susceptibility. The formation of ammonium hydroxide has been blamed for the SCC of brasses in humid atmospheres; however, other ammonium salts, such as chloride and nitrate, are also being formed in the present urban atmospheres, where industrial alloys are extensively used. Thus, a systematic study of the effect of these ammonium salts on SCC is necessary to understand SCC in these solutions. Brown [79] reported that SCC occurs in ammoniacal solutions and all other species which can react with copper to produce the cupric-ammonium complexes or structurally similar complexes. However, cracking has been observed in Mattsson's solution at pH values where such complexes are not stable [6]. If complexing effect is necessary for SCC of brass, then no SCC should occur in noncomplexing solutions. On the other hand, if complexing effect is a sufficient condition for SCC, then SCC should occur in any complexing solution, unless there are certain requirements to be met. A detailed study of SCC of brass in complexing and noncomplexing solutions should reveal the role of complexing effect in SCC process.

Later on, the SCC studies were extended to nonammoniacal solutions, but most of the investigations were conducted using dynamic load techniques with different strain rates and potentiostatic anodic potentials to enhance the SCC process. The effect of the strain rate on the dissolution process was reported by many authors [80-85]. According to Parkins [86], the dissolution at the crack tip depends not only upon the electrochemical conditions but also upon the rate at which bare metal is created at the crack tip by plastic strain. Maximum cracking can be expected at an intermediate rate in slow strain rate tests. In constant load tests, the crack propagation will continue only when the strain rate at the crack tip exceeds the minimum rate required. On the other hand, the potentiostatic anodic polarization will increase the anodic dissolution of the sample under investigation. In general, the conditions of constant load and open circuit potential (used earlier) are more relevant to service conditions. Therefore, these conditions should be used during the SCC investigation to eliminate any probability of enhanced dissolution or failure due to strain.

Electrochemical polarization curves and Tafel plot technique have been used extensively to clarify the corrosion mechanisms and calculate the corrosion parameters [87-95]. Several computer programs were developed to replace the analytical methods and facilitate the lengthy calculations [96-103]. However, the application of electrochemical polarization techniques in SCC studies has been mostly qualitative with little effort to relate the calculated corrosion parameters to the reactions taking place on the electrode surface. Moreover, very few studies have attempted to develop suitable methods for SCC prediction. There is no doubt that electrochemistry plays an important role in SCC process, since a stressed sample would not fail or crack in dry atmospheres. A careful combination of results obtained by different electrochemical techniques should reveal the type and extent of chemical reactions taking place during SCC process, and lead to better understanding of the SCC mechanisms. It is also expected that the SCC susceptibility in each solution will be related to the electrochemical behavior of the alloy under investigation. Thus, there may be a simple and effective electrochemical test which can be used to predict SCC in different solutions.

Finally, the controversy over the SCC of pure copper in different aqueous solutions needs to be resolved; the first step should be repetition of previously reported studies but under common experimental conditions. This should be followed by the investigation of SCC behavior of pure copper in other solutions under these same conditions and generalization of the results.

The present work was conducted under constant load and open circuit potential conditions to study the following.

1. The effect of different anions of ammonium salts on the SCC of brass. Mattsson's nontarnishing solution was also investigated for the sake of comparison.

2. The SCC behavior of brass in different (complexing and noncomplexing) nonammoniacal solutions.

3. The application of electrochemical methods to predict, study, and identify (with the help of surface analysis techniques) the SCC mechanism(s).

4. The SCC behavior of pure copper in different aqueous solutions.

EXPERIMENTAL

Material

Stress corrosion cracking samples

Tensile stress specimen Samples of total length of 10 cm and 0.5 cm in diameter were machined using α-brass rods of composition 80% Cu - 20% Zn (atomic weight %). The samples were annealed at 400°C for 1 hr in argon atmosphere. Each sample was electropolished, in an electrolyte bath [60 ml methanol + 30 ml nitric acid (70%)] at 0°C and controlled potential of 30 volts, for one minute. The sample was then washed in ultrasonic methanol bath and dried in warm air.

Loop specimens Loops were prepared from brass rods 0.15 cm in diameter, 60 cm in length, and composition of 59.54 Cu-38.57 Zn-0.32 Fe-0.82 Sn (weight %). The brass rods were bent around a 3/8-inch diameter mandrel to produce the loops. The loops were chemically polished in an acid mixture [40 ml glacial acetic + 25 ml phosphoric (70%) + 10 ml HNO_3 (60%)] then washed in an ultrasonic water bath and dried in nitrogen atmosphere. Each rod produced up to eight loops.

Electrochemical tests samples

α-brass (80/20) samples Cylindrical samples of 0.70 cm diameter and 0.4 cm in thickness were machined and used as the working electrode in rotating disc electrode.

Cylindrical samples of 0.95 cm diameter and 0.2 cm in thickness were used as the disc electrode in rotating ring disc electrode (RRDE) with platinum ring.

The discs were polished manually using silicon carbide paper (600 type) then three grades of alumina (1 μ, 0.3 μ, then 0.05 μ) on polishing cloth. The samples were then washed in an ultrasonic water bath and dried in a nitrogen atmosphere.

αβ'-brass (60/39) samples Rods of brass (60/39) 24 cm long and 0.15 cm diameter were fixed in glass tubes (17 cm long and 0.5 cm diameter) using silicone rubber. The upper end of the wire (~ 5 cm) was cleaned, abraded, and used for electrical connection. The lower end (~ 2 cm) was all covered, except a total area of 0.5 cm^2, with silicone rubber. The produced electrode was chemically cleaned in the acid mixture mentioned above. Pure copper and zinc electrodes were prepared in the same way.

Solutions

Three sets of solutions were studied. The first set includes solutions reported before to cause stress corrosion cracking of brasses [6,62,66,67], e.g., ammoniacal copper sulfate, nitrate, nitrite, and chlorate solutions. The second set includes solutions not necessarily reported to cause SCC of brasses but with anions known to form complexes with Cu^{2+} and Zn^{2+} ions, e.g., pyrophosphate solution (stability constants are shown in Appendix C). The third set includes ammonium salt solutions with different anions, namely, ammonium (nitrate, sulfate, carbonate, and chloride) solutions with and without 0.05 M Cu^{2+} ions.

All solutions were prepared from reagent grade chemicals and quadruply distilled water.

Measurement Techniques

Stress corrosion cracking tests

Tensile stress test   This test was conducted using an Instron tensile stress machine and the tensile stress specimens of α-brass (80/20). The machine was equipped with a Wheatstone bridge driven by D.C. power supply and connected to a time recorder to determine the time-to-failure in each solution. The tensile specimens were prestressed in air to a fixed point beyond the ultimate tensile stress value by applying a constant crosshead speed of 0.05 inch/hr, and a full load of 2400 lb. The carriage was then stopped and the specimen kept under constant load while completely immersed in the solution under test. The samples were removed from the solution after failure or after seven days, which was first.

Loop specimen tests   The two ends of each loop were connected by an insulated copper wire, and the loops were suspended in 100-ml beakers containing 50 ml of each solution under test and isolated from the atmosphere. The loops were observed periodically for any cracks. Two loops were used in each solution and the average time-to-cracking was calculated.

Electrochemical tests

The following tests were conducted using the computerized corrosion system Model 332 (Figure 5) (EG&G Princeton Applied Research).

Corrosion potential, E_{cor}, measurements   The corrosion potential of brass samples in each solution was measured every minute for a

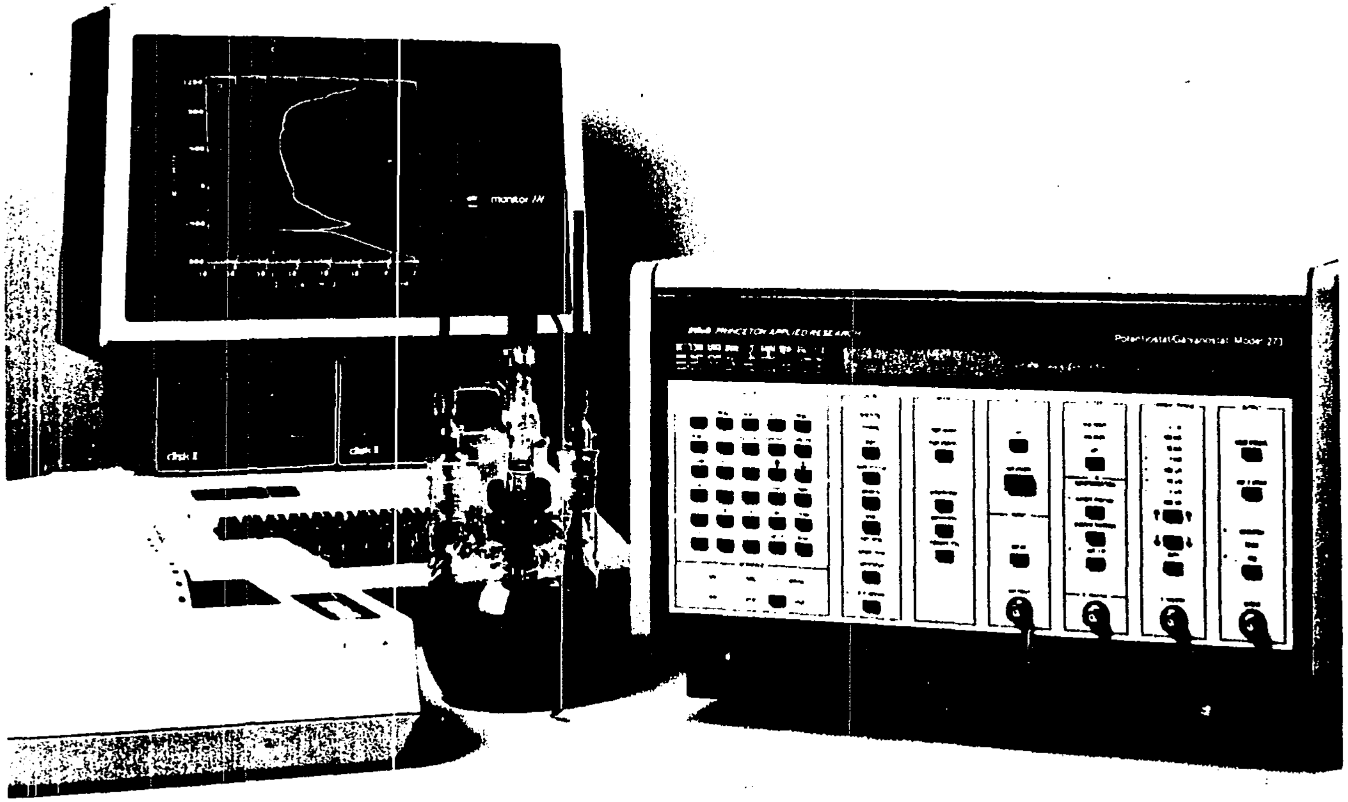

Fig. 5. The corrosion measurements system Model 332, containing Potentiostat/Galvanostat Model 273, and an Apple IIe Computer

total of 180 minutes. In most cases, the corrosion potential was almost constant within this period.

Tafel plot measurements The cathodic then anodic polarization of the sample were conducted in the potential range of ±250 mV w.r.t. the corrosion potential at a scan rate of 0.05 mV/s. The slopes of both cathodic and anodic Tafel lines were calculated from the straight portions of the cathodic and anodic branches. The point of intersection of both lines determines the corrosion potential and corrosion current, i_{cor}. The calculations were mostly done by the computer program, Parcalc, which is based on the Stern and Geary model of polarized electrodes [104].

Cyclic polarization measurements The sample potential was scanned at 1 mV/s from cathodic to anodic potentials, then back to the cathodic region. The potential range used was ±250 mV w.r.t. the corrosion potential.

All the electrochemical tests mentioned above were conducted under identical conditions of stirring to minimize the mass transfer effects [105].

Rotating ring disc measurements These tests were conducted to detect intermediate Cu^+-complexes produced during the corrosion process at the brass disc in ammoniacal complexing solutions. The potential of the disc electrode was scanned in the anodic region w.r.t. the corrosion potential, while the platinum ring potential was fixed at +0.5 V_{SHE}.

All electrochemical measurements were conducted using a saturated

Calomel electrode as the reference and a graphite electrode as the counter electrode.

Surface analysis tests

Energy-dispersive x-ray analysis (EDAX)

This technique was used to identify the composition of the crack and mechanically-fractured surfaces. Facilities for performing it are included in the Scanning Auger Multiprobe, PHI 600, and were used for this purpose.

Scanning electron microscope (SEM)

A Cambridge S-200 scanning electron microscope was used to determine the surface characteristics of produced SCC surfaces.

Optical microscopy technique

A Zeiss Axiomat Metallograph was used to determine the mode of stress corrosion cracking in different solutions, e.g., intergranular or transgranular.

RESULTS AND DISCUSSION

Brass in Ammoniacal and Ammonium Salts
Aqueous Solutions

Stress corrosion cracking tests

The loop samples of $\alpha\beta'$-brass (60/39) were found to crack in hydroxide and nitrate solutions with and without Cu^{2+}-ions, but not in carbonate or chloride solutions with and without Cu^{2+}-ions. The results are summarized in Table 1. On the other hand, the tesntile stress specimens of α-brass (80/20) failed in hydroxide solution, but not in nitrate or sulfate solutions. The results of α-brass are summarized in Table 2.

The results show that α-brass (80/20) is less susceptible to SCC than $\alpha\beta'$-brass (60/39) at open circuit potential under static load. Both brasses are susceptible to SCC in Mattsson's solution (1 M $NH_4OH + 0.05$ M $CuSO_4$). However, while t_c of $\alpha\beta$-brass in ammonium-copper nitrate solution is half that in Mattsson's solution, α-brass did not fail in ammonium-copper nitrate solution within a period five times that needed to fail in Mattsson's solution. This supports earlier findings [59] that the susceptibility of brass to SCC increases with increasing zinc content.

The loop test proved to be a simple and efficient test for the simultaneous study of brass cracking in several solutions. The good agreement, between the two samples used in each solution, proves a satisfactory reproducibility, similar to that reported before [6,8]. It is also worthy to notice that the ratio of times-to-crack, in hydroxide and sulfate solutions with Cu^{2+} ions, is $31.5/5.25 = 6$, com-

Table 1. Time-to-crack of $\alpha\beta'$-brass (60/39) loop specimens in various aqueous solutions at 25°C

Solution	pH	$\bar{t}_c$ [a] (hrs)	E_{cor} [b] (mV_{SHE})
1 M NH_4OH + 0.05 M $CuSO_4$ [c]	10.90	5.25	-129
1 M NH_4OH [c]	11.40	48	-233
1 M NH_4NO_3 + 0.05 M $Cu(NO_3)_2$	3.60	2.75	292
1 M NH_4NO_3	5.80	48	48
1 M $(NH_4)_2SO_4$ + 0.05 M $CuSO_4$	3.90	31.50	257
1 M $(NH_4)_2SO_4$	5.90	NC [d]	123
1 M $(NH_4)_2CO_3$ + 0.05 M $CuSO_4$ [c]	8.50	NC	- 38
1 M $(NH_4)_2CO_3$ [c]	8.60	NC	-190
1 M NH_4Cl + 0.05 M $CuCl_2$	3.50	NC	105
1 M NH_4Cl	5.65	NC	- 96

[a] Average time-to-crack.

[b] Corrosion potential (relative to standard hydrogen electrode).

[c] Solutions forming Cu^{2+}-complexes.

[d] No cracking in 7 days.

pared to 90/15.56 = 5.78 in Mattsson's work [6].

The progression of time-to-crack, t_c, shows that the presence of Cu^{2+} ions increases the SCC susceptibility. Many authors [12,15,19, 23,106] have claimed that. In the present study, brass cracked in hydroxide solutions, where Cu^{2+}-complexes are stable, and also in nitrate

Table 2. Time-to-failure of α-brass (80/20) tensile stress specimens in various aqueous solutions at 25°C

Solution	pH	t_f [a]	E_{cor} [b] (mV_{SHE})
1 M NH_4OH + 0.05 M $CuSO_4$ [c]	10.9	30	-102.6
1 M NH_4NO_3 + 0.05 M $Cu(NO_3)_2$	3.60	NF[d]	-
1 M $(NH_4)_2SO_4$ + 0.05 M $CuSO_4$	3.90	NF	-

[a] Time-to-failure.

[b] Corrosion potential (relative to standard hydrogen electrode).

[c] Solutions forming Cu^{2+}-complexes.

[d] No failure in 7 days.

solutions, where Cu^{2+}-complexes are not stable in the portions of potential/pH diagram studied. On the other hand, brass didn't crack in solutions containing (carbonate solutions) and free of (sulfate solution) Cu^{2+}-complexes. This observation suggests that while the presence of Cu^{2+} ions is necessary but not sufficient for SCC to occur, the complexing effect is neither necessary nor sufficient for SCC. Bertocci et al. [51] observed recently the SCC of α-brass (70/30) in the presence of Cu^{+}-complexes only and concluded that Cu^{2+}-complexes are not necessary for SCC. It should be noticed that these results were obtained using the slow-strain rate technique. Using the constant load technique, the present work shows that neither Cu^{2+}-complexes nor Cu^{+}-complexes are necessary for SCC as long as Cu^{2+} ions can furnish the required cathodic species.

The immunity to SCC of brasses in sulfate solution can be attributed to the formation of a Cu_2O film, which prevents more dissolution, in addition to the inhibiting effect of sulfate ion previously reported [107].

The immunity in carbonate solution containing Cu^{2+} ions may be due to the high general and uniform corrosion which occurs in presence of these ions, instead of the pit formation required to initiate SCC process. The large increase in corrosion rate, when sulfate was replaced by carbonate anion in cupric ammoniacal solutions, was observed before by Sedzimir and Bujanska [108]. On the other hand, the immunity in Cu^{2+}-free carbonate solution may be the result of insufficient corrosion rate in this solution. Lees and Hoar [109] reported that, in Mattsson's solution at pH=8.9, no SCC occurred due to uniform dissolution of the sample surface. Similarly, in chloride solutions, the brass immunity to SCC can be attributed to the high general and uniform corrosion in the presence of Cu^{2+} ions and to insufficient corrosion rate in their absence. Moreover, the inhibiting effect of Cl^- ion on SCC of brass in Mattsson's solution has been reported by many authors [8,67, 107,110].

Electrochemical tests

Corrosion potential, E_{cor}, measurements   Corrosion potential vs. time curves, for $\alpha\beta'$-brass (60/39) in different ammonium salt solutions, are shown in Figures 6-9. Among the solutions containing Cu^{2+} ions,

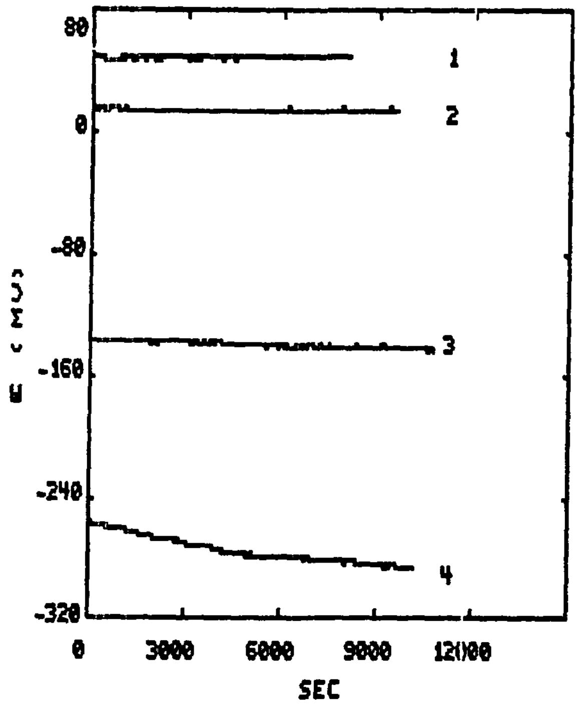

1. 1 M NH_4NO_3 + 0.05 M $Cu(NO_3)_2$
2. 1 M $(NH_4)_2SO_4$ + 0.05 M $CuSO_4$
3. 1 M NH_4Cl + 0.05 M $CuCl_2$
4. 1 M $(NH_4)_2CO_3$ + 0.05 M $CuSO_4$

Figure 6. Corrosion potential vs. time for αβ'-brass (60/39) electrode in various ammonium salts solutions, containing Cu^{2+} ions, at 25°C

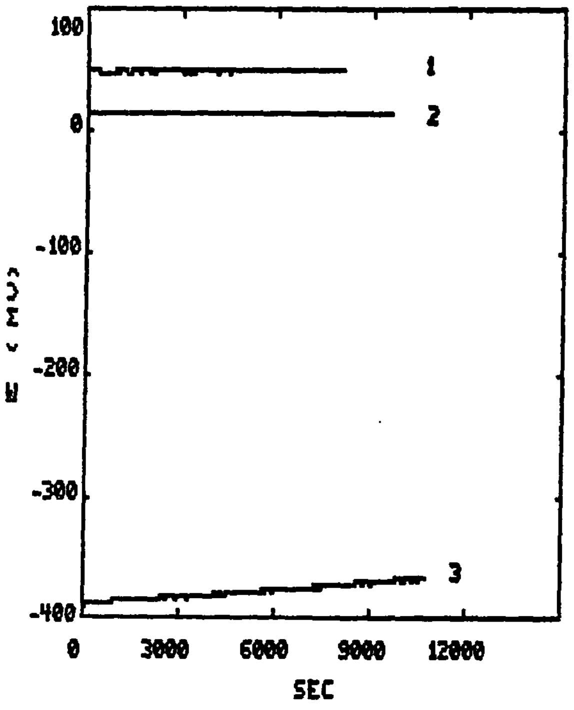

1. 1 M NH_4NO_3 + 0.05 M $Cu(NO_3)_2$
2. 1 M $(NH_4)_2SO_4$ + 0.05 M $CuSO_4$
3. 1 M NH_4OH + 0.05 M $CuSO_4$

Figure 7. Corrosion potential vs. time for αβ'-brass (60/39) electrode in ammoniacal and ammonium salts solutions (where SCC was observed) at 25°C

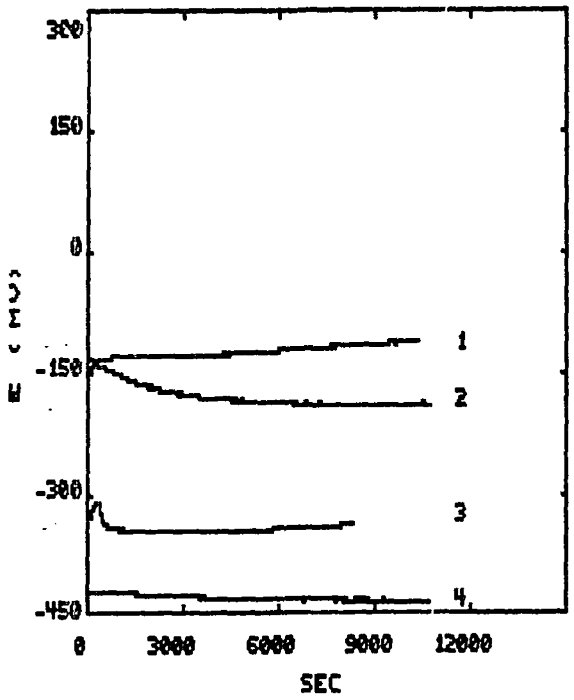

1. 1 M $(NH_4)_2SO_4$
2. 1 M NH_4NO_3
3. 1 M NH_4Cl
4. 1 M $(NH_4)_2CO_3$

Figure 8. Corrosion potential vs. time for αβ'-brass (60/39) electrode in various ammonium salts solutions at 25°C

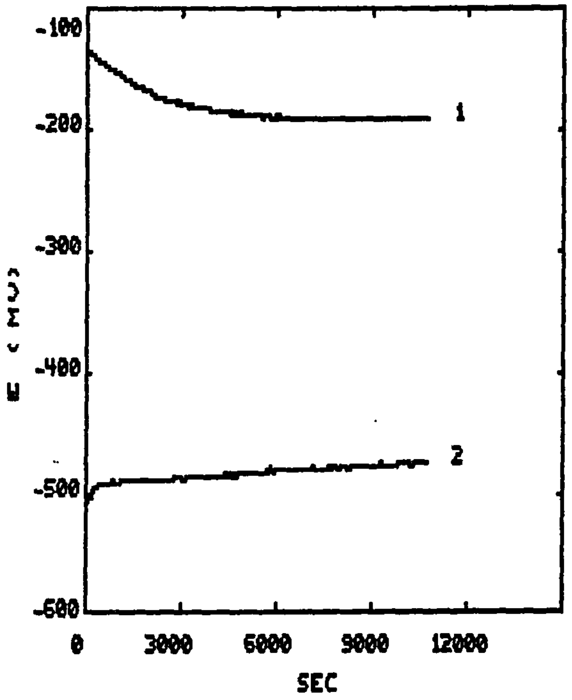

1. 1 M NH_4NO_3
2. 1 M NH_4OH

Figure 9. Corrosion potential vs. time for αβ'-brass (60/39) electrode in ammoniacal and ammonium salt solutions (where SCC was observed) at 25°C

the least noble potentials are observed in carbonate and hydroxide solutions, where Cu^{2+} ions are complexed. In solutions which are originally Cu^{2+}-ions-free, the least noble potentials are observed in carbonate, hydroxide and chloride solutions, where dissolved copper is complexed in the first two and negligible in the third solution. In other solutions, the potential is very close to that for a standard Cu/Cu^{2+} electrode potential, indicating either the pretest introduction of Cu^{2+} ions or appreciable copper dissolution. The numerical values of corrosion potentials after three hours are shown in Tables 1 and 2. The change of corrosion potential with time can be used in some cases to confirm electrochemical reactions taking place at the electrode surface. For example, considering the Cu^{2+} ions-containing solutions, the shift of E_{cor} into the noble direction in hydroxide solution indicates the increase of metallic ion concentration in the solution, while the almost constant E_{cor} value in nitrate and sulfate solutions indicates a balanced dissolution and deposition of metallic ions (Figure 6). However, no direct relation between the corrosion potential and the SCC susceptibility could be drawn, which means that corrosion potential alone cannot be used to identify, predict, or monitor SCC. It was concluded elsewhere [111], that measurements of E_{cor} vs. time alone are not reliable indicators of relative corrosion rate when oxygen reduction is the cathodic process.

Tafel plots results The experimental Tafel plots were used to calculate the Tafel line slopes and corrosion parameters by means of the Parcalc program which is based on the Stern and Geary equation

[104]:

$$i_{app} = i_{cor} \{\exp(\frac{nB_aF}{RT})^{\eta} - \exp(\frac{-nB_cF}{RT})^{\eta}\} \qquad (1)$$

where:

i_{app} = the external current density, $\mu A/cm^2$
i_{cor} = corrosion current density, $\mu A/cm^2$
n = # electrons involved in the reaction
B_a, B_c = anodic and cathodic symmetry coefficients
F = Faraday's constant, 96500 coulomb/equiv.
η = overvoltage potential, in volts
R = universal gas constant, 8.3 goule/mole °K
T = temperature, °K

The Parcalc program final results are:

E(I=0): corrosion potential in mV_{SCE}
Cathodic Tafel (slope) in mV
Anodic Tafel (slope) in mV
I_{corr}: corrosion current in $\mu A/cm^2$
Corrosion rate (MPY): millinch per year
CHI^2: a numerical measure for the fitting of the experimental data to the theoretical model

In some cases, where more than one Tafel line appears in the same region, the calculated Tafel line slope has no relation to any of the reactions taking place, a case reported before by Stern [112]. In these cases, where the value of CHI^2 is also high, manual measurements of Tafel slopes are used.

Tafel slopes and corrosion parameters are used to predict all the possible cathodic and anodic reactions. The prediction is based on:

1. The corrosion potential, E_{cor}, should always lie between the cathodic and anodic reaction potentials.

2. The cathodic and anodic reaction potentials are obtained from the corresponding potential/pH diagrams. As an approximation, the diagrams of $Cu-H_2O-NH_3$ and $Zn-H_2O-NH_3$ constructed by Mattsson [6] are used.

3. Transfer coefficients, α_{aa} and α_{cc}, are calculated from Tafel line slope according to:

$$\alpha = \frac{2.3\ RT}{F\ (\text{slope})} \qquad (2)$$

   The values of α_{aa} are reported as 1/2 for elementary one-electron reactions and 3/2 for several divalent metals [113].

4. The exchange current for each reaction is calculated according to the formula [113].

$$i_{cor} = i_{oa}\ \exp\left(\frac{\alpha_{aa}F}{RT}\right)(\phi^*-\phi^\circ_a) = i_{oc}\ \exp\left(\frac{-\alpha_{cc}F}{RT}\right)(\phi^*-\phi^\circ_c) \qquad (3)$$

   where:

   i_{oa}, i_{oc} = anodic and cathodic exchange current density, A/cm^2

   α_{aa}, α_{cc} = transfer coefficients

   ϕ^* = corrosion potential, E_{cor}

   $\phi^\circ_a, \phi^\circ_c$ = standard reduction potentials for anodic and cathodic reactions

5. Coupling several simultaneous cathodic reactions with the anodic reaction produces a corrosion rate controlled by the cathodic reaction with the largest rate. The corrosion potential would lie nearer to the potential of the reaction (anodic or cathodic) with the faster rate (higher exchange current, or lower polarizability) [113,114].

The calculation results in each solution are discussed in the following. Table 3 summarizes the results obtained for all the solutions under test.

Table 3. Electrochemical reactions of $\alpha\beta'$-brass (60/39) in ammoniacal and ammonium salts solutions at 25°C (see Table 1 for pH and E_{corr} values)

Solution	i_{cor} ($\mu A/cm^2$)	Anodic reaction (species to be oxidized)	α_{aa}	Cathodic reaction (species to be reduced)	α_{cc}
1 M NH_4OH + 0.05 M $CuSO_4$	2307	Cu Zn	0.16	$[Cu(NH_3)_4]^{2+}$	0.17
1M NH_4OH	115	Cu Zn	0.30	O_2	0.30
1 M NH_4NO_3 + 0.05 M $Cu(NO_3)_2$	6947	Zn	0.44	NO_3^- Cu^{2+}	0.24
1 M NH_4NO_3	37	Zn	0.48	NO_3^-	0.20
1 M $(NH_4)_2SO_4$ + 0.05 M $CuSO_4$	1637	Zn	-	O_2 Cu^{2+}	-
1 M $(NH_4)_2SO_4$	33	Zn	0.58	O_2	0.40
1 M $(NH_4)_2CO_3$ + 0.05 M $CuSO_4$	11973	Cu Zn	0.26	$[Cu(NH_3)_4]^{2+}$	0.24
1 M $(NH_4)_2CO_3$	89	Zn	0.99	O_2	0.20
1 M NH_4Cl + 0.05 M $CuCl_2$	8999	Cu Zn	0.55	Cu^{2+}	0.20
1 M NH_4Cl	21	Zn	0.98	O_2	0.32

$1\ M\ NH_4OH + 0.05\ M\ CuSO_4$ The Tafel plot and Parcalc results are shown in Figure 10. The most probable reactions, along with kinetic parameters, are:

Reactions	Potential (V_H)	i_o A/cm^2	α
Cathodic:			
$O_2 + 2H_2O + 4e \rightleftarrows 4OH^-$	0.584	2.2×10^{-5}	0.17
$O_2 + H_2O + 2e \rightleftarrows HO_2^- + OH^-$	0.015	0.85×10^{-3}	"
$[Cu(NH_3)_4]^{2+} + 2H^+ + e \rightleftarrows [Cu(NH_3)_2]^+ + 2NH_4^+$	0.060	0.64×10^{-3}	"
Anodic:			
$[Cu(NH_3)_2]^+ + 2H^+ + e \rightleftarrows Cu + 2NH_4^+$	-0.19	1.7×10^{-3}	0.16
$[Zn(NH_3)_4]^{2+} + 4H^+ + 2e \rightleftarrows Zn + 4NH_4^+$	-1.05	0.89×10^{-5}	"

Among the possible cathodic reactions, the reduction of Cu^{2+}-complexes is more favorable due to higher concentration and exchange current. On the other hand, the Cu dissolution is more favored as the anodic reaction due to:

1. higher exchange current
2. more appropriate value of transfer coefficient, α_{aa}, to Cu (normal value 0.5) than to Zn (normal value 1.5)
3. closer anodic reaction potential to the corrosion potential. This means that the anodic reaction should be of higher exchange current than the cathodic one. This is true only for Cu-dissolution.

The higher dissolution rate of Cu is further supported by the Tafel results for pure Cu and pure Zn in the same solution (Figures 11,12).

```
======================================
           PARCALC TAFEL MENU
======================================
EXP. NAME:TAF MATSTIR 1        DATA:195
TECHNIQUE:TAFEL                [E VS I]
--------------------------------------

                RESULTS

E(I=0) (MV)                 -382.83

CATHODIC TAFEL (MV)         359.17

ANODIC TAFEL (MV)           376.08

I-CORR (UA/CM^2)            2307.35849

CORR RATE (MPY)             1128.24

CHI ^2                      60.03
```

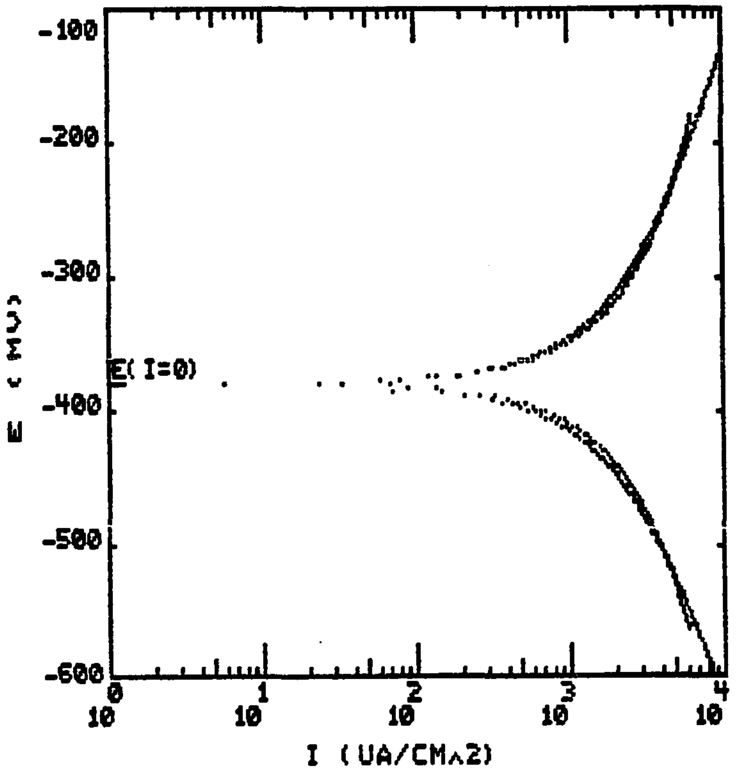

Figure 10. Tafel plot and Parcalc results for αβ'-brass (60/39) electrode in 1 M NH_4OH + 0.05 M $CuSO_4$ solution at 25°C

```
=====================================
         PARCALC TAFEL MENU
=====================================
EXP. NAME:TAFCU MATSTIR1*     DATA:171
TECHNIQUE:TAFEL               [E VS I]
-------------------------------------

              RESULTS

E(I=O) (MV)              -214.31

CATHODIC TAFEL (MV)       251.91

ANODIC TAFEL (MV)         284.66

I-CORR (UA/CM^2)         1489.42

CORR RATE (MPY)          1373.31

CHI ^2                     39.81
```

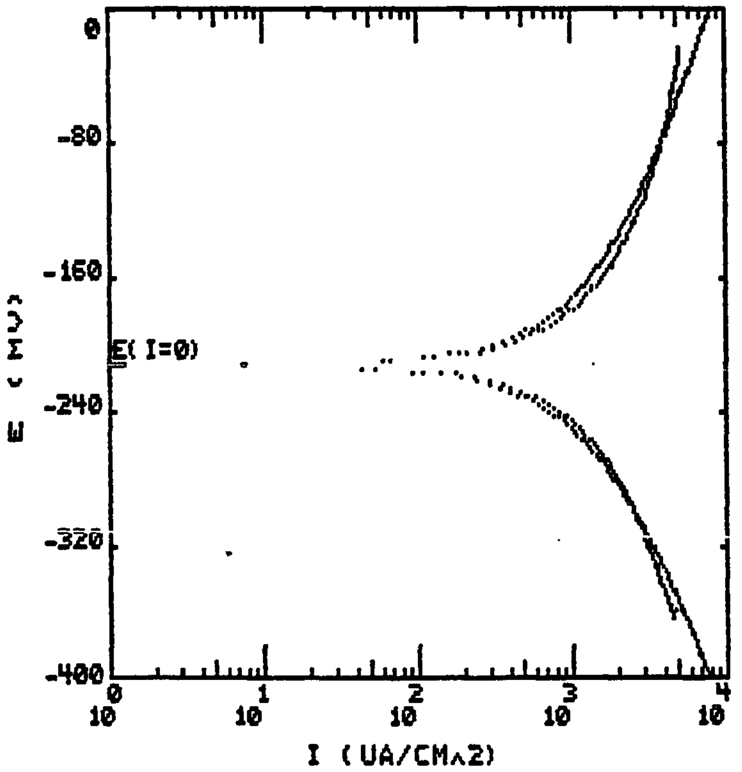

Figure 11. Tafel plot and Parcalc results for pure copper electrode in 1 M NH_4OH + 0.05 M $CuSO_4$ solution at 25°C and scan rate of 0.5 mV/s

```
=====================================
           PARCALC TAFEL MENU
=====================================
EXP. NAME:TAFZN MATSTIR2*      DATA:40
TECHNIQUE:TAFEL                [E VS I]
-------------------------------------

                RESULTS

E(I=0) (MV)                -298.35

CATHODIC TAFEL (MV)        218.98

ANODIC TAFEL (MV)          220.57

I-CORR (UA/CM^2)           1049.04

CORR RATE (MPY)            624.39

CHI ^2                     537.76
```

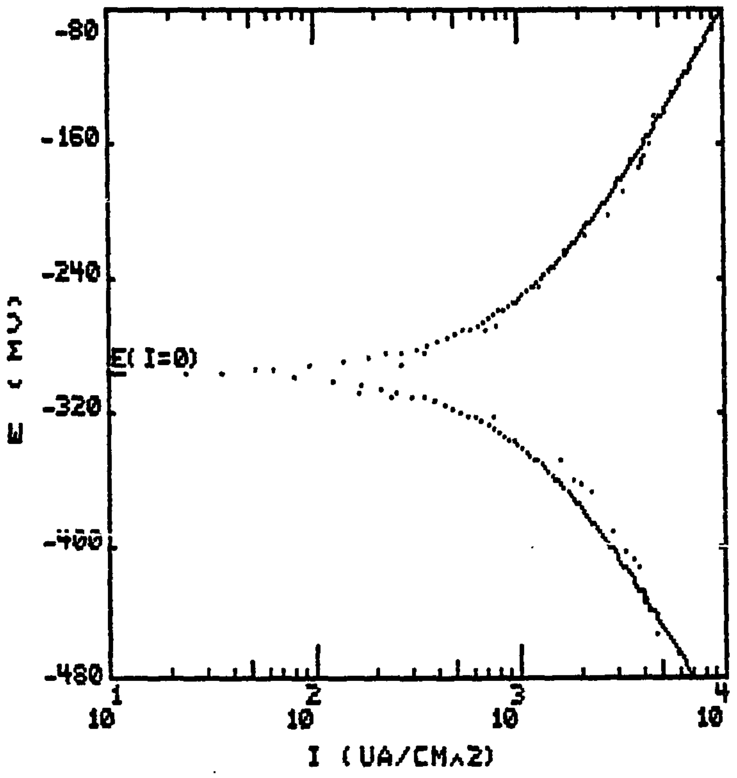

Figure 12. Tafel plot and Parcalc results for pure zinc electrode in 1 M NH_4OH + 0.05 M $CuSO_4$ solution at 25°C and scan rate of 0.5 mV/s

The results show a higher corrosion current in the case of Cu.

1 M NH_4OH The Tafel plot and Parcalc results are shown in Figure 13. The most probable reactions and their kinetic parameters are:

Reaction	Potential V_H	i_o A/cm^2	α
Cathodic:			
$O_2 + 2H_2O + 4e \rightleftarrows 4OH^-$	0.554	1.1×10^{-8}	0.30
$O_2 + H_2O + 2e \rightleftarrows HO_2^- + OH^-$	0.0007	0.63×10^{-5}	"
$O_2 + 2H_2O + 2e \rightleftarrows H_2O_2 + 2OH^-$	0.007	0.59×10^{-5}	"
Anodic:			
$[Cu(NH_3)_2]^+ + 2H^+ + e \rightleftarrows Cu + 2NH_4^+$	-0.400	0.21×10^{-4}	0.30
$[Zn(NH_3)_4]^{2+} + 4H^+ + 2e \rightleftarrows Zn + 4NH_4^+$	-1.050	1.1×10^{-8}	"

Again, Cu-dissolution is more favored than Zn-dissolution for the same reasons mentioned before. This is also supported by the observation of solution coloration shortly after the sample immersion. The low corrosion current can be explained using the potential/pH diagram for Cu-H_2O-NH_3 constructed by Johnson and Leja [14], where Cu_2O is stable at the present solution pH. At higher anodic potentials, Cu_2O is oxidized to CuO.

1 M NH_4NO_3 + 0.05 M $Cu(NO_3)_2$ Three successive Tafel plots (Figure 14) show clearly the presence of two Tafel lines in the cathodic region. The Parcalc results (Figure 15) show, as should be expected,

```
=======================================
          PARCALC TAFEL MENU
=======================================
EXP. NAME:TAFSTIR AM*          DATA:223
TECHNIQUE:TAFEL                [E VS I]
---------------------------------------

               RESULTS

E(I=O) (MV)               -495

CATHODIC TAFEL (MV)       201.09

ANODIC TAFEL (MV)         197.36

I-CORR (UA/CM^2)          115.12963

CORR RATE (MPY)           57.18

CHI ^2                    38.84
```

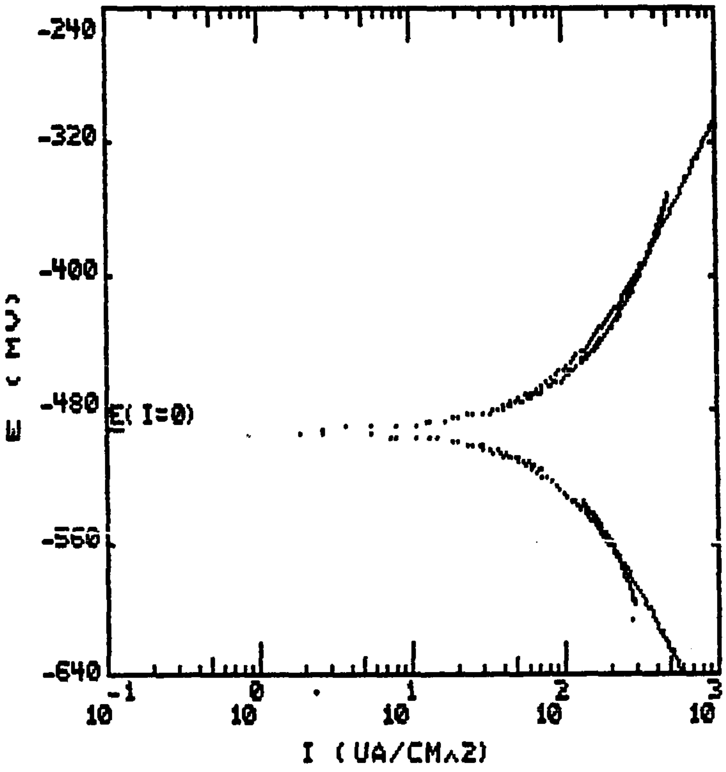

Figure 13. Tafel plot and Parcalc results for αβ'-brass (60/39) electrode in 1 M NH_4OH solution at 25°C

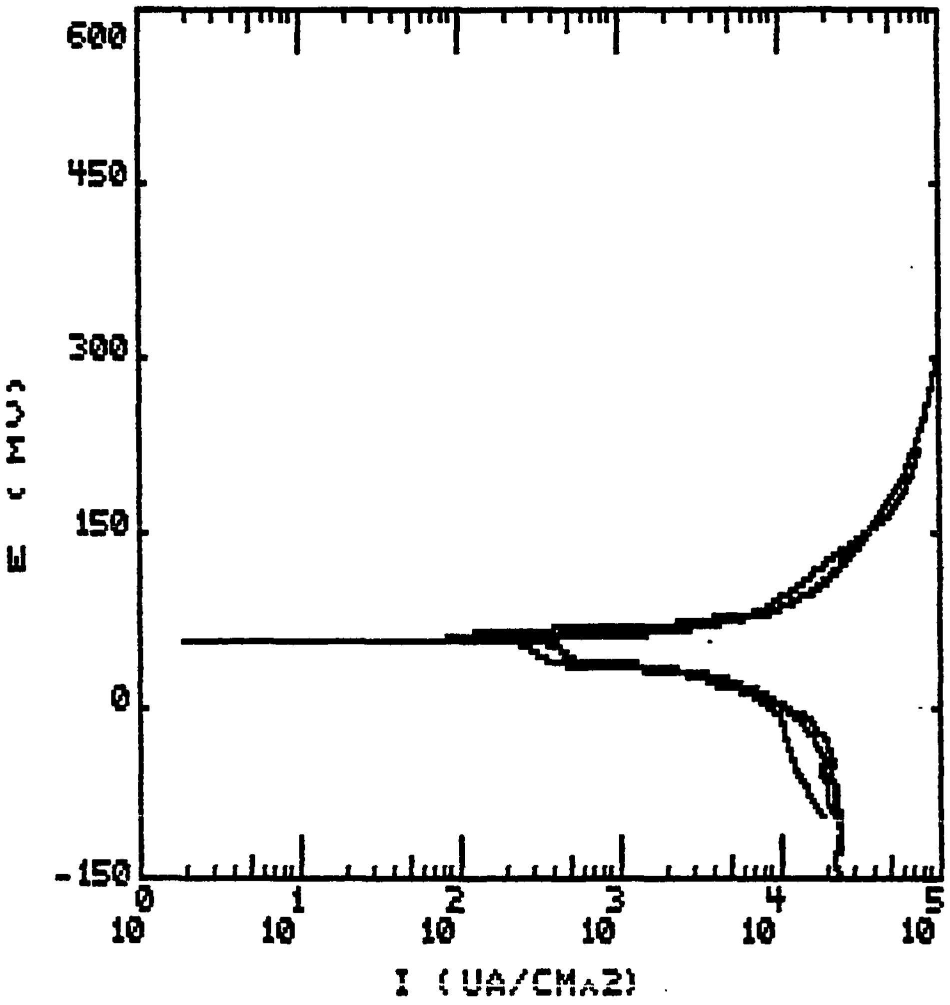

Figure 14. Tafel plots for αβ'-brass (60/39) electrode in 1 M NH_4NO_3 + 0.05 M $Cu(NO_3)_2$ solution, reproduced at the same experimental conditions at 25°C

```
======================================
          PARCALC TAFEL MENU
======================================
EXP. NAME:TAF AMNITSTIR1*      DATA:182
TECHNIQUE:TAFEL                [E VS I]
--------------------------------------

               RESULTS

E(I=0) (MV)               51.6

CATHODIC TAFEL (MV)       530.01

ANODIC TAFEL (MV)         165.58

I-CORR (UA/CM^2)          6947.07548

CORR RATE (MPY)           3396.93

CHI ^2                    720.85
```

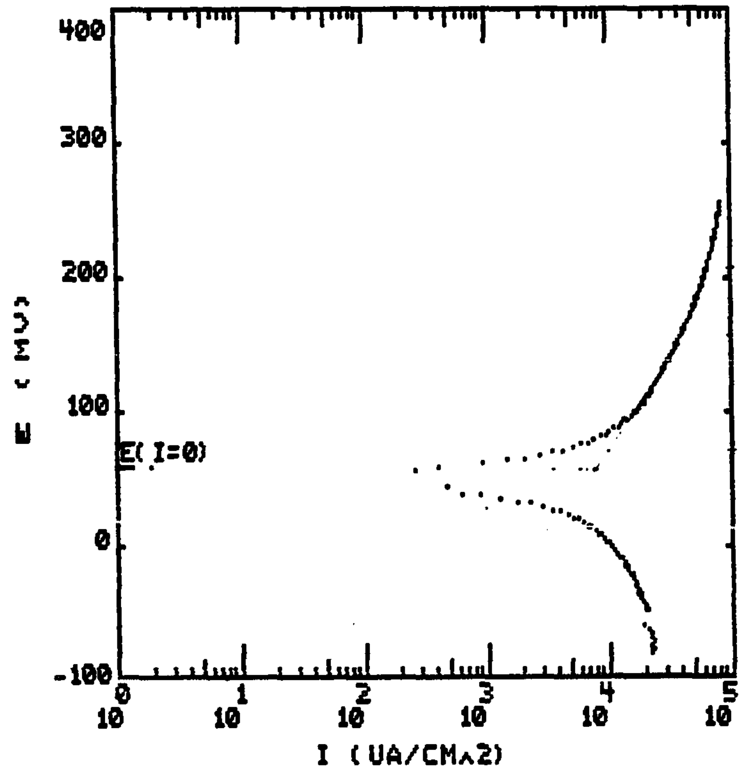

Figure 15. Tafel plot and Parcalc results for αβ'-brass (60/39) electrode in 1 M NH_4NO_3 + 0.05 M $Cu(NO_3)_2$ solution at 25°C

a large difference between the experimental data and the theoretical model (based on one reaction in each region). The results obtained by manual measurements are shown below along with those obtained by Parcalc:

	E_{cor} mV_H	i_{cor} $\mu A/cm^2$	Anodic Tafel mV	Cathodic Tafel I mV	Cathodic Tafel II mV
Manual	293.6	8000	137.5	254.17	123.13
Parcalc	293.6	6947	165.58	530.01	-

The most probable cathodic reactions are:

Reaction	Potential (V_H)	i_o (A/cm^2)	α
$O_2 + 4H^+ + 4e \rightleftharpoons 2H_2O$	1.018	0.12×10^{-4}	0.24
$O_2 + 2H_2O + 4e \rightleftharpoons 4OH^-$	1.016	0.12×10^{-4}	"
$NO_3^- + 4H^+ + 3e \rightleftharpoons NO + H_2O$	0.674	0.27×10^{-3}	"
$NO_3^- + 3H^+ + 2e \rightleftharpoons HNO_2 + H_2O$	0.618	0.45×10^{-3}	"
$2NO_3^- + 4H^+ + 2e \rightleftharpoons N_2O_4 + 2H_2O$	0.380	0.39×10^{-2}	"

The reduction of Cu^{2+} to Cu, which occurs at 300 mV_H, seems to take place at potentials very close to E_{cor}, leading to the second cathodic Tafel line.

On the other hand, the most probable anodic reaction is:

Reaction	Potential (V_H)	i_o A/cm^2	α
$Zn^{2+} + 2e \rightleftharpoons Zn$	-0.820	0.58×10^{-10}	0.44

The oxidation of Cu to Cu_2O (proposed by Mattsson's diagram) is not consistent with the high corrosion current observed. The dissolution of Cu to Cu^{2+} (assumed by Johnson and Lega) will actually be at equilibrium since it has almost the same potential ($\sim 0.30\ V_H$) as the corrosion potential.

The final reactions will be the dissolution of Zn and the reduction of Cu^{2+} ions. This is supported by the observed gradual disappearance of solution color after the sample immersion. The Zn-dissolution is also supported by the Tafel experiments for pure Cu and pure Zn in the same solution (Figures 16,17), which show a Zn corrosion current vastly greater than that of Cu.

<u>1 M NH_4NO_3</u> The Tafel plot and Parcalc results are shown in Figure 18. The most probable reactions, with their kinetic parameters, are:

Reaction	Potential (V_H)	i_o (A/cm^2)	α
Cathodic:			
$O_2 + 4H^+ + 4e \rightleftharpoons 2H_2O$	0.887	0.68×10^{-7}	0.20
$O_2 + 2H_2O + 4e \rightleftharpoons 4OH^-$	0.885	0.69×10^{-7}	"
$NO_3^- + 4H^+ + 3e \rightleftharpoons NO + H_2O$	0.508	1.4×10^{-6}	"
$2NO_3^- + 4H^+ + 2e \rightleftharpoons N_2O_4 + 2H_2O$	0.430	0.27×10^{-5}	"
Anodic:			
$Zn^{2+} + 2e \rightleftharpoons Zn$	-0.82	0.17×10^{-11}	0.48

```
========================================
          PARCALC TAFEL MENU
========================================
EXP. NAME:TAFCU AMNITST3*     'DATA:152
TECHNIQUE:TAFEL                [E VS I]
----------------------------------------

                RESULTS

E(I=O) (MV)                 100.4

CATHODIC TAFEL (MV)         114.6

ANODIC TAFEL (MV)           102.8

I-CORR (UA/CM^2)            2029.56

CORR RATE (MPY)             1871.34

CHI ^2                      522.67
```

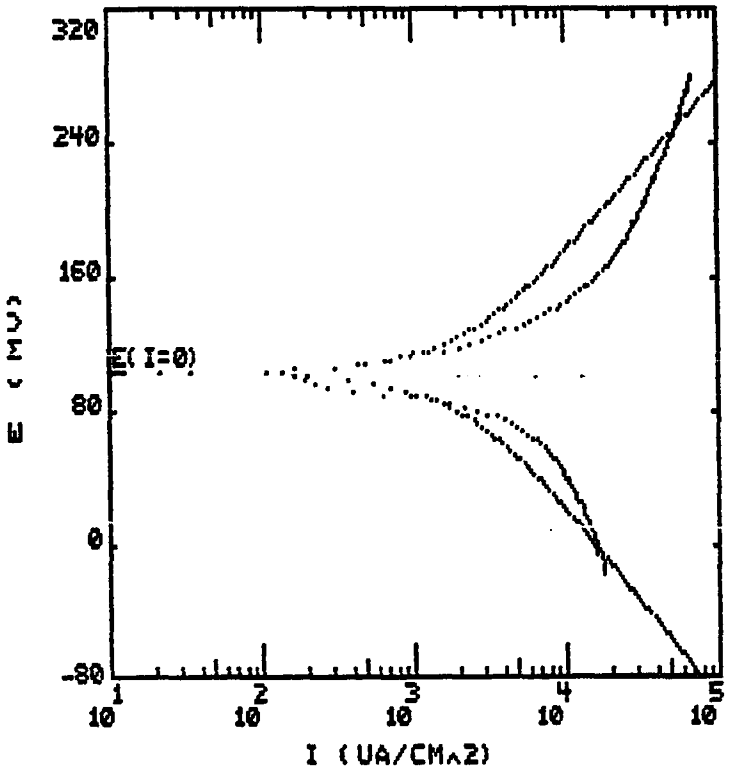

Figure 16. Tafel plot and Parcalc results for pure copper electrode in 1 M NH_4NO_3 + 0.05 M $Cu(NO_3)_2$ solution at 25°C and scan rate of 0.5 mV/s

```
========================================
          PARCALC TAFEL MENU
========================================
EXP. NAME:TAFZN AMNITST2*      DATA:56
TECHNIQUE:TAFEL                [E VS I]
----------------------------------------

               RESULTS

E(I=0) (MV)               -462.99

CATHODIC TAFEL (MV)       245.08

ANODIC TAFEL (MV)         196.37

I-CORR (UA/CM^2)          15874.902

CORR RATE (MPY)           9448.69

CHI ^2                    592.25
```

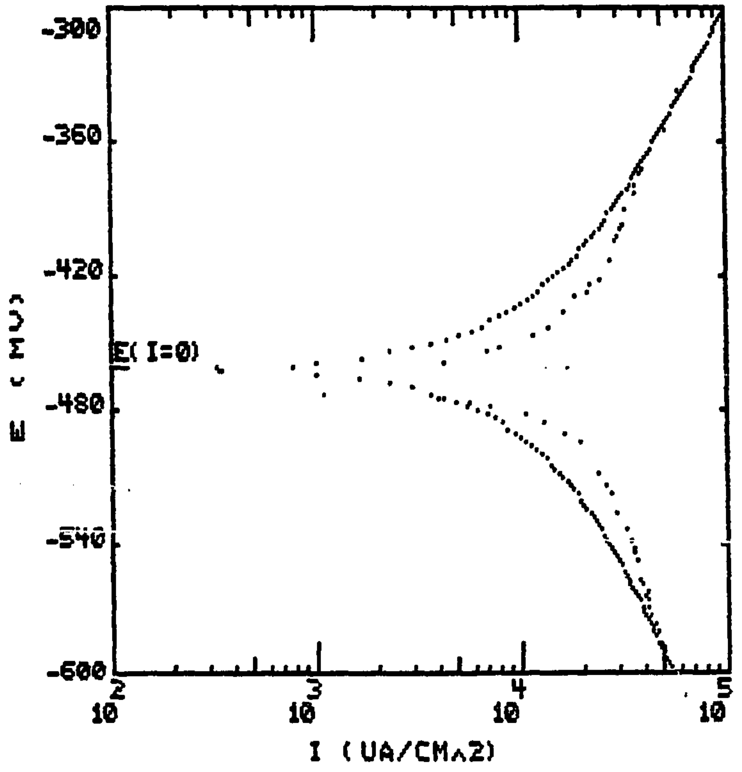

Figure 17. Tafel plot and Parcalc results for pure zinc electrode in 1 M NH_4NO_3 + 0.05 M $Cu(NO_3)_2$ solution at 25°C and scan rate of 0.5 mV/s

```
======================================---
           PARCALC TAFEL MENU
========================================
EXP. NAME:TAFST AMNITO*          DATA:199
TECHNIQUE:TAFEL                  [E VS I]
----------------------------------------

                RESULTS

E(I=O)  (MV)               -142.19

CATHODIC TAFEL  (MV)       286.92

ANODIC TAFEL  (MV)         125.17

I-CORR  (UA/CM^2)          37.3888889

CORR RATE  (MPY)           18.57

CHI  ^2                    57.75
```

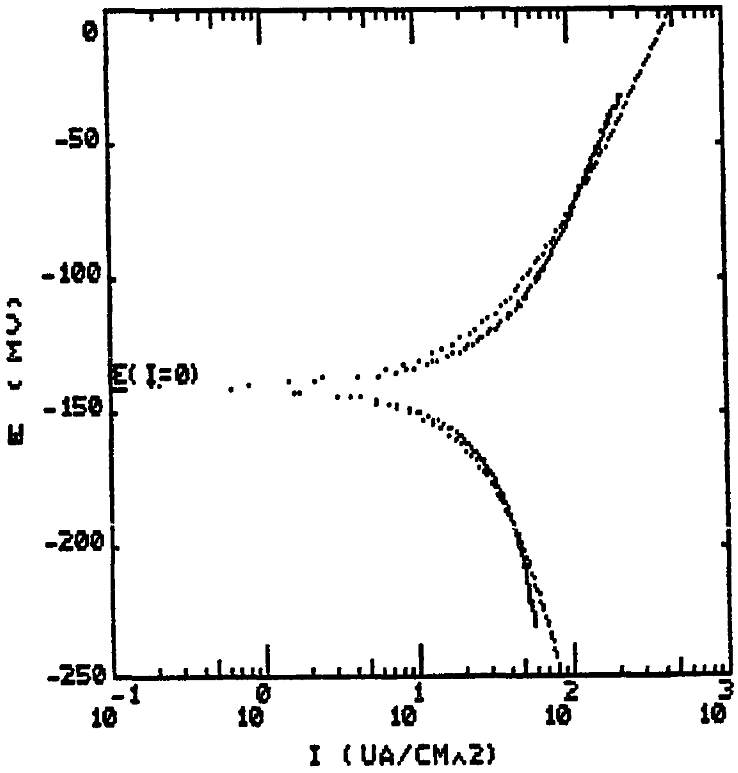

Figure 18. Tafel plot and Parcalc results for αβ'-brass (60/39) electrode in 1 M NH_4NO_3 solution at 25°C

So, the dissolution of Zn (and not of copper due to potential consideration), and the reduction of nitrate ion (due to higher exchange current) are initially favored as the anodic and cathodic reactions. Due to consumption of H^+ ions (in cathodic reaction) the pH increases and Cu-dissolution reaction potential takes values less noble than the corrosion potential. This is supported by the observation that the solution pH shifted from 5.68 (at the experiment beginning) to 6.68 three days later, and that the colorless solution became deep blue (indication of Cu^{2+}-complex formation) after four days.

$\underline{1\ M\ (NH_4)_2SO_4 + 0.05\ M\ CuSO_4}$ Two successive Tafel plots (Figure 19) show the presence of two Tafel lines in the cathodic region, similar to those in the solution of 1 M NH_4NO_3 + 0.05 M $Cu(NO_3)_2$. Moreover, the anodic curve shows the presence of two anodic Tafel lines. The large deviation, between the experimental data and the theoretical model, shown by CHI^2 value (Figure 20) is not surprising. The only reliable parameter is the corrosion potential value, which is also consistent with the corrosion potential experiment result. According to the corrosion potential value, the most probable reactions are:

	Potential (V_H)
Cathodic:	
$O_2 + 4H^+ + 4e \rightleftarrows 2H_2O$	0.995
$O_2 + 2H_2O + 4e \rightleftarrows 4OH^-$	1.007
$Cu^{2+} + 2e \rightleftarrows Cu$	0.300
Anodic:	
$Zn^{2+} + 2e \rightleftarrows Zn$	-0.820

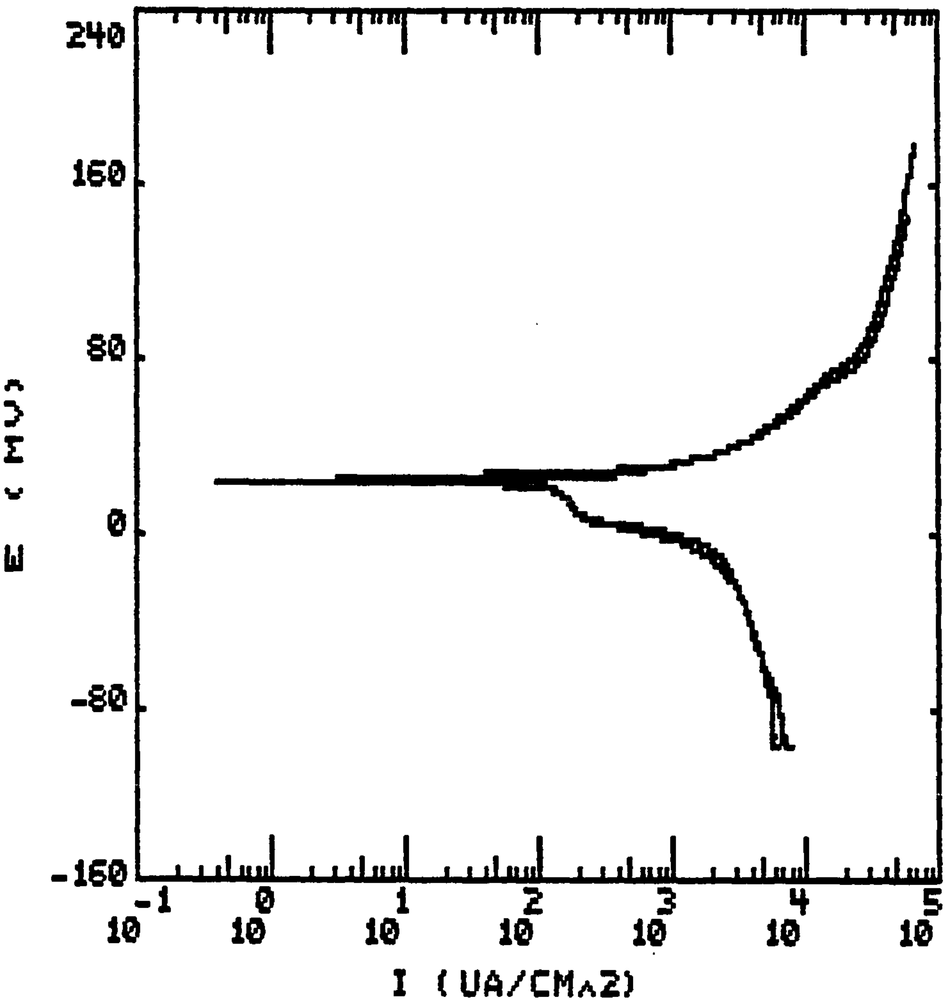

Figure 19. Tafel plots for αβ'-brass (60/39) electrode in 1 M $(NH_4)_2SO_4$ + 0.05 M $CuSO_4$ solution, reproduced at the same experimental conditions at 25°C

```
=======================================
          PARCALC TAFEL MENU
=======================================
EXP. NAME:TAFSTIR AMSU1*       DATA:151
TECHNIQUE:TAFEL                [E VS I]
---------------------------------------

               RESULTS

E(I=O) (MV)               14.88

CATHODIC TAFEL (MV)       843.3

ANODIC TAFEL (MV)         51.39

I-CORR (UA/CM^2)          1637.16667

CORR RATE (MPY)           813.06

CHI ^2                    831.65
```

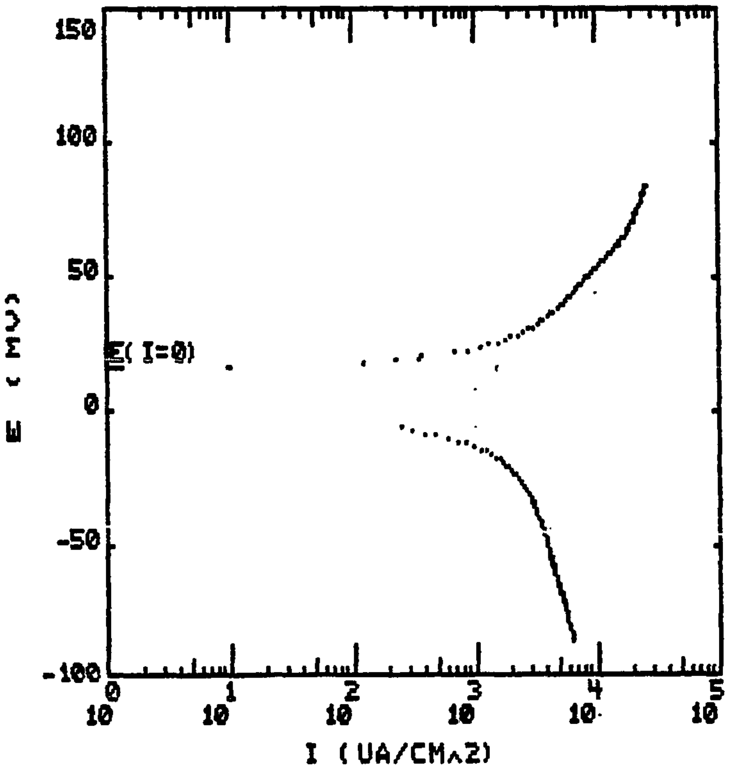

Figure 20. Tafel plot and Parcalc results for $\alpha\beta'$-brass (60/39) electrode in 1 M $(NH_4)_2SO_4$ + 0.05 M $CuSO_4$ solution at 25°C

The Zn dissolution and Cu^{2+}-reduction are supported by the observed solution color disappearance.

$\underline{1\ M\ (NH_4)_2SO_4}$ The Tafel plot and calculations are shown in Figure 21. The most probable reactions and their kinetic parameters are:

Reaction	Potential (V_H)	i_o (A/cm^2)	α
Cathodic:			
$O_2 + 4H^+ + 4e \rightleftharpoons 2H_2O$	0.879	$0.2x10^{-9}$	0.40
$O_2 + 2H_2O + 4e \rightleftharpoons 4OH^-$	0.877	$0.2x10^{-9}$	"
Anodic:			
$Zn^{2+} + 2e \rightleftharpoons Zn$	-0.820	$0.61x10^{-13}$	0.58

According to both Mattsson, and Johnson and Leja, Cu does not take part in any reaction. This is supported by the observation that no solution coloration occurred. The low value of Zn-dissolution exchange current is consistent with the small corrosion current observed.

$\underline{1\ M\ (NH_4)_2CO_3 + 0.05\ M\ CuSO_4}$ The Tafel plot and Parcalc results are shown in Figure 22. The probable reactions are:

Reaction	Potential (V_H)	i_o (A/cm^2)	α
Cathodic:			
$O_2 + 4H^+ + 4e \rightleftharpoons 2H_2O$	0.728	$0.76x10^{-5}$	0.24
$O_2 + 2H_2O + 4e \rightleftharpoons 4OH^-$	0.726	$0.78x10^{-5}$	"

```
=========================================
           PARCALC TAFEL MENU
=========================================
EXP. NAME:TAFST AMSUO*          DATA:130
TECHNIQUE:TAFEL                 [E VS I]
-----------------------------------------

                RESULTS

E(I=0) (MV)               -150.8

CATHODIC TAFEL (MV)       150.42

ANODIC TAFEL (MV)         104.11

I-CORR (UA/CM^2)          33.4901961

CORR RATE (MPY)           16.63

CHI ^2                    27.03
```

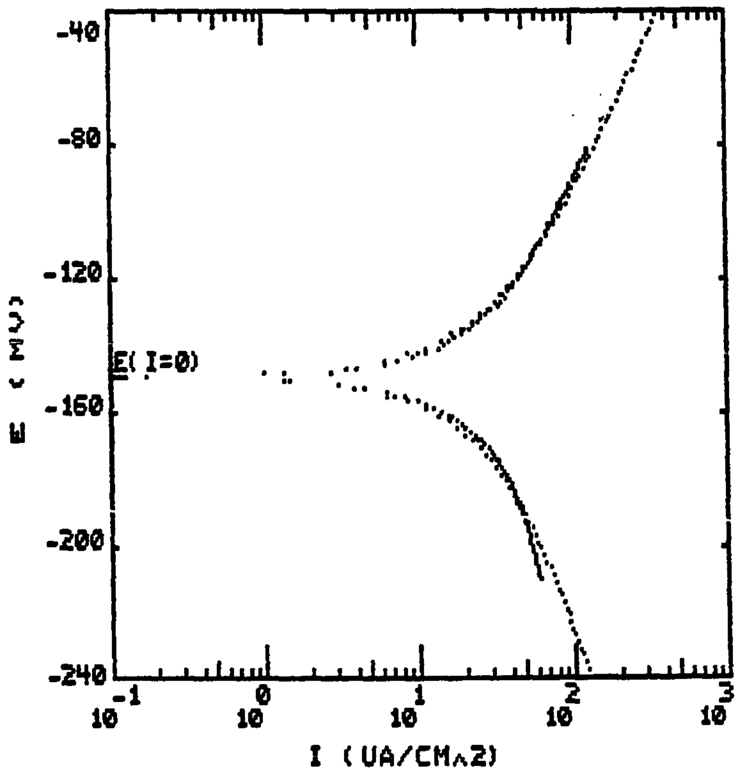

Figure 21. Tafel plot and Parcalc results for αβ'-brass (60/39) electrode in 1 M $(NH_4)_2SO_4$ solution at 25°C

```
=======================================
          PARCALC TAFEL MENU
=======================================
EXP. NAME:TAFST AMCAR*          DATA:150
TECHNIQUE:TAFEL                 [E VS I]
---------------------------------------

                RESULTS

E(I=O) (MV)                -291.97

CATHODIC TAFEL (MV)        243.22

ANODIC TAFEL (MV)          227.51

I-CORR (UA/CM^2)           11973.5926

CORR RATE (MPY)            5946.46

CHI ^2                     26.93
```

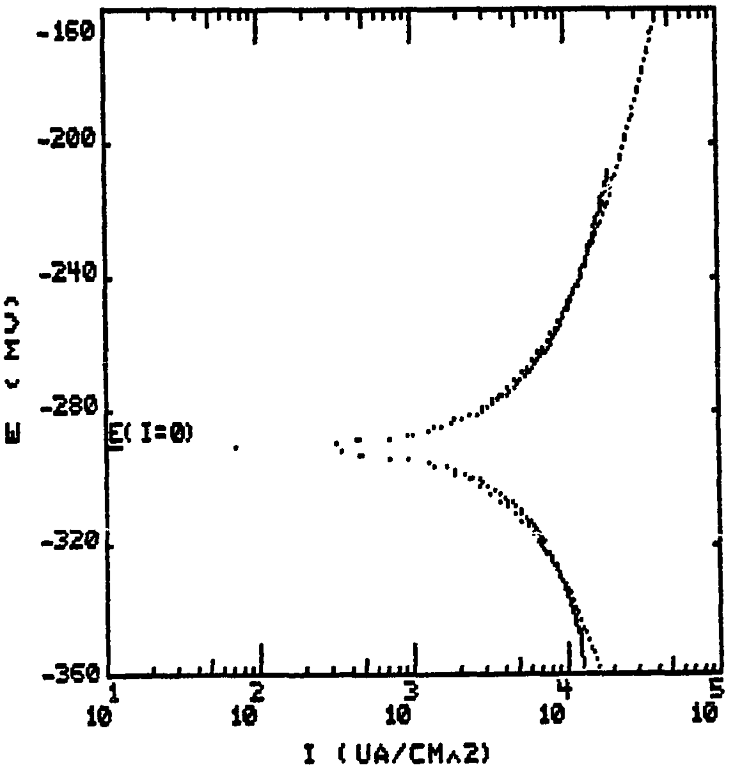

Figure 22. Tafel plot and Parcalc results for αβ'-brass (60/39) electrode in 1 M $(NH_4)_2CO_3$ + 0.05 M $CuSO_4$ solution at 25°C

	Potential (V_H)	i_o (A/cm^2)	α
Cathodic:			
$O_2 + H_2O + 2e \rightleftharpoons HO_2^- + OH^-$	0.087	0.33×10^{-2}	"
$[Cu(NH_3)_4]^{2+} + 2H^+ + e \rightleftharpoons [Cu(NH_3)_2]^+ + 2NH_4^+$	0.150	0.18×10^{-2}	"
Anodic:			
$[Zn(NH_3)_4]^{2+} + 4H^+ + 2e \rightleftharpoons Zn + 4NH_4^+$	-0.97	0.11×10^{-5}	0.26
$[Cu(NH_3)_2]^+ + 2H^+ + e \rightleftharpoons Cu + 2NH_4^+$	-0.11	0.65×10^{-2}	"

Again Cu^{2+}-complex reduction is favored due to higher concentration and exchange current. On the other hand, Cu-dissolution is favored over Zn dissolution for the same reasons discussed before in the case of 1 M NH_4OH + 0.05 M $CuSO_4$ solution.

<u>1 M $(NH_4)_2CO_3$</u> Tafel plot and Parcalc results are shown in Figure 23. The most probable reactions and their kinetic parameters are:

Reaction	Potential (V_H)	i_o (A/cm^2)	α
Cathodic:			
$O_2 + 4H^+ + 4e \rightleftharpoons 2H_2O$	0.721	0.94×10^{-7}	0.20
$O_2 + 2H_2O + 4e \rightleftharpoons 4OH^-$	0.719	0.95×10^{-7}	"
$O_2 + H_2O + 2e \rightleftharpoons HO_2^- + OH^-$	0.083	0.12×10^{-4}	"
Anodic:			
$[Zn(NH_3)_4]^{2+} + 4H^+ + 2e \rightleftharpoons Zn + 4NH_4^+$	-1.05	0.61×10^{-18}	0.99

```
=====================================
          PARCALC TAFEL MENU
=====================================
EXP. NAME:TAFST AMCARO*        DATA:200
TECHNIQUE:TAFEL                [E VS I]
-------------------------------------

               RESULTS

E(I=0) (MV)               -431.72

CATHODIC TAFEL (MV)       305.06

ANODIC TAFEL (MV)         60.64

I-CORR (UA/CM^2)          89.6862745

CORR RATE (MPY)           44.54

CHI ^2                    2.87
```

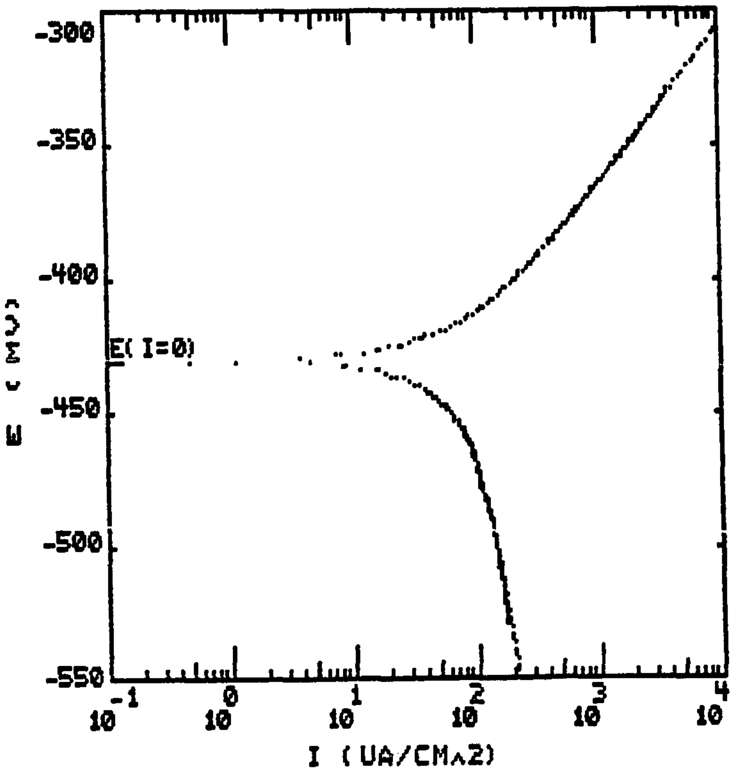

Figure 23. Tafel plot and Parcalc results for αβ'-brass (60/39) electrode in 1 M $(NH_4)_2CO_3$ solution at 25°C

The low exchange current for Zn-dissolution is consistent with low corrosion current observed. At increased value of solution pH, due to cathodic reaction, the Cu-dissolution potential shifts to less noble values than the corrosion potential. This is supported by the observation of solution coloration shortly after the sample immersion.

1 M NH_4Cl + 0.05 M $CuCl_2$ Tafel plot and Parcalc results are shown in Figure 24. The probable reactions are:

Reaction	Potential (V_H)	i_o (A/cm^2)	α
Cathodic:			
$O_2 + 4H^+ + 4e \rightleftharpoons 2H_2O$	1.024	0.50×10^{-5}	0.20
$CuCl_2 + e \rightleftharpoons CuCl_2^-$	0.300	0.19×10^{-2}	"
Anodic:			
$Zn^{2+} + 2e \rightleftharpoons Zn$	-0.933	0.21×10^{-11}	0.55
$CuCl_2^- + e \rightleftharpoons Cu + 2\ Cl^-$	-0.026	0.5×10^{-3}	"

All the potential values are obtained from potential/pH diagrams of Zn-H_2O and Cu-H_2O-Cl^- in reference [115].

The reduction of Cu^{2+} to $CuCl_2^-$ is favored as the cathodic reaction due to higher concentration and exchange current. On the other hand, the Cu dissolution is favored over Zn-dissolution for the same reasons mentioned before in the case of 1 M NH_4OH + 0.05 M $CuSO_4$ solution. At higher anodic potential, $CuCl_2^-$ is further oxidized to $CuCl_2$ according to:

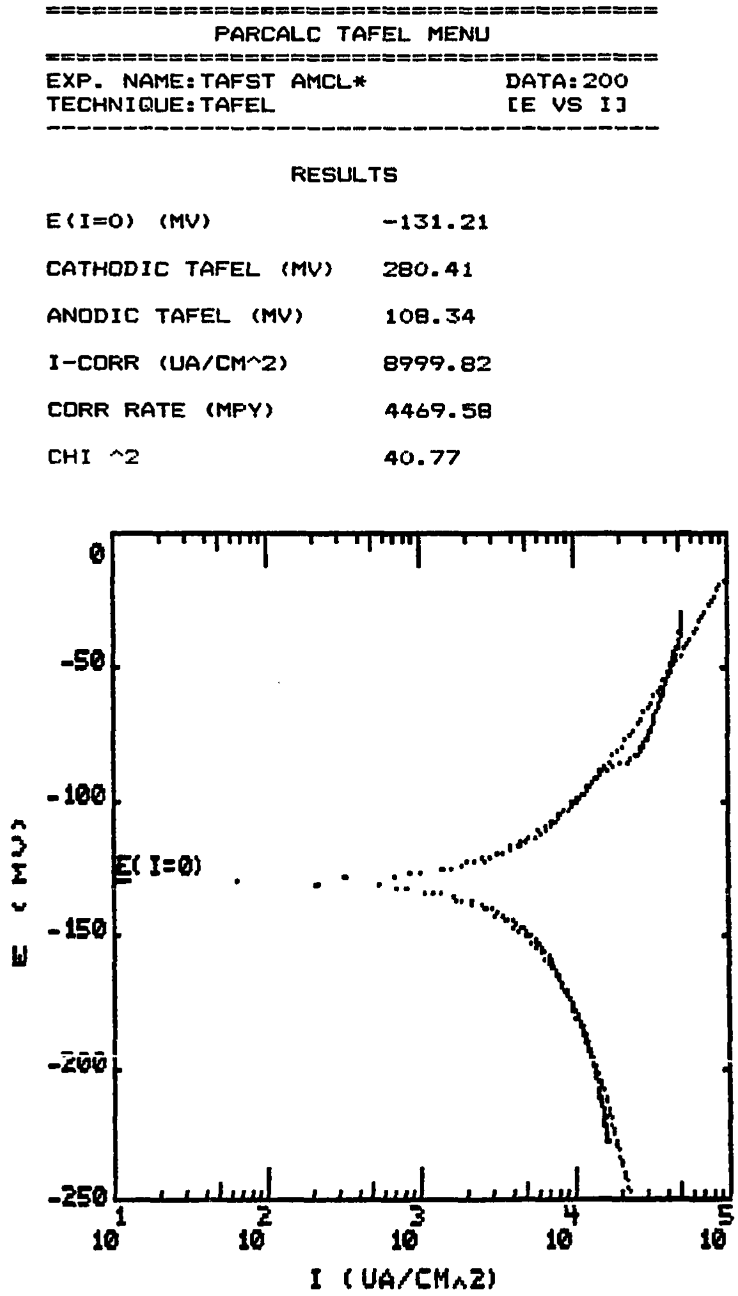

```
=====================================
           PARCALC TAFEL MENU
=====================================
EXP. NAME:TAFST AMCL*        DATA:200
TECHNIQUE:TAFEL              [E VS I]
-------------------------------------

                RESULTS

E(I=O)  (MV)              -131.21

CATHODIC TAFEL (MV)       280.41

ANODIC TAFEL (MV)         108.34

I-CORR (UA/CM^2)          8999.82

CORR RATE (MPY)           4469.58

CHI ^2                    40.77
```

Figure 24. Tafel plot and Parcalc results for αβ'-brass (60/39) electrode in 1 M NH_4Cl + 0.05 M $CuCl_2$ solution at 25°C

$CuCl_2 + e \rightleftharpoons [CuCl_2]^-$ ... 0.300 V_H.

This reaction leads to another anodic Tafel line as observed in Figure 24 at a potential $\geq$ 160 mV_H.

<u>1 M NH_4Cl</u> Tafel plot and Parcalc results are shown in Figure 25. The most probable reactions are:

Reaction	Potential (V_H)	i_o (A/cm^2)	α
Cathodic:			
$O_2 + 2H_2O + 4e \rightleftharpoons 4OH^-$	0.902	0.96×10^{-10}	0.32
$O_2 + 4H^+ + 4e \rightleftharpoons 2H_2O$	0.896	0.1×10^{-9}	"
$O_2 + H_2O + 2e \rightleftharpoons HO_2^- + OH^-$	0.175	0.73×10^{-6}	"
Anodic:			
$Zn^{2+} + 2e \rightleftharpoons Zn$	-0.933	0.76×10^{-18}	0.98

The low corrosion current observed is consistent with the low exchange current for the Zn dissolution reaction.

The Tafel plots were always used for qualitative evaluation of corrosion rates. In the present work, the quantitative results of the Tafel plot measurements imply the electrochemical reactions taking place at the electrode surface related to SCC. The results show the presence of three regions of corrosion current, i_{cor}, values.

First region: $i_{cor}<0.1$ mA/cm^2. Corrosion current is sufficiently low that SCC is not observed in the 7-day observation period.

Second region: $0.1\leq i_{cor}\leq 5$ mA/cm^2. SCC generally observed whenever the dissolution mechanism operates.

```
=========================================
            PARCALC TAFEL MENU
=========================================
EXP. NAME:TAFST AMCLO 2*        DATA:210
TECHNIQUE:TAFEL                 [E VS I]
-----------------------------------------

                 RESULTS

E(I=0) (MV)                 -344.88

CATHODIC TAFEL (MV)         187.33

ANODIC TAFEL (MV)           61.59

I-CORR (UA/CM^2)            21.66

CORR RATE (MPY)             10.76

CHI ^2                      6.4
```

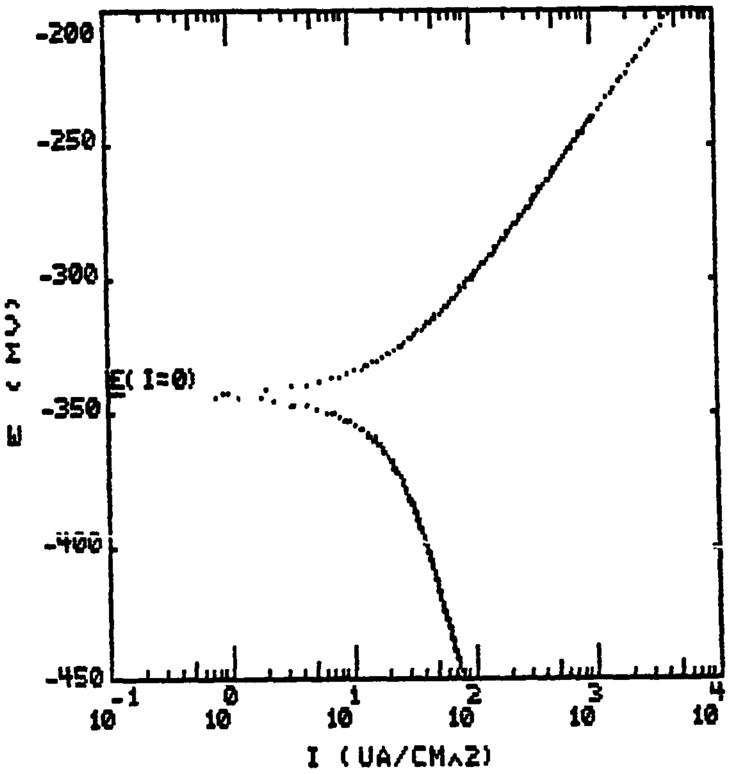

Figure 25. Tafel plot and Parcalc results for $\alpha\beta'$-brass (60/39) electrode in 1 M NH_4Cl solution at 25°C

Third region: $i_{cor}>5$ mA/cm^2. SCC is rarely observed, because the associated polarization usually results in general and uniform corrosion.

While SCC was not observed in the first and third regions (except cases where the dissolution mechanism is not believed to operate), SCC was always observed in the second region. This observation supports the assumption that the dissolution mechanism is in effect in case of nontarnishing solutions and that only moderate corrosion rate can cause SCC in this case.

One of the interesting findings in the present work is the preferential dissolution of copper in complexing solutions. This was first predicted from electrochemical measurements on brass, where the predicted anodic reactions from Tafel plots show the preferential copper dissolution in complexing solutions. The same result was then confirmed by Tafel plot measurements on pure copper and pure zinc in complexing and noncomplexing solutions under the same conditions. Table 4 shows the ratios of corrosion currents of pure Cu and pure zinc in two different solutions (complexing and noncomplexing), at two different scan rates.

Table 4. Corrosion current ratios of pure copper and pure zinc

	i_{Cu}/i_{Zn}	
Solution	Scan rate 0.05 mV/s	Scan rate 0.5 mV/s
1 M NH_4OH + 0.05 M $CuSO_4$ [a]	1.20	1.40
1 M NH_4NO_3 + 0.05 M $Cu(NO_3)_2$	0.30	0.36

[a] Complexing solution.

Similar results were obtained in Cu^{2+}-containing carbonate solution. The results were further confirmed by surface analysis results as will be discussed later.

Corapcioglu [116] reported that the affinity of Cu^{2+} ions to surface adsorption is higher than that of Zn^{2+} ions in noncomplexing solutions where copper dissolves by two one-electron transfer reactions mechanism [113,117]:

$$Cu(s) \xrightarrow{\text{fast}} Cu^{+}_{surf} + e \ldots. \quad (4a)$$

$$Cu^{+}_{surf} \xrightarrow{\text{slow}} Cu^{2+}_{soln} + e \ldots. \quad (4b)$$

Under concentration polarization conditions, the higher adsorption of Cu^{2+} ions on the surface will lead to lower copper dissolution (in noncomplexing solutions containing Cu^{2+} ions) and selective dissolution of zinc. On the other hand, in complexing solutions, where Cu^{+}-complexes are stabilized, reaction (4b) may not be important. Subsequent formation of Cu^{2+}-complexes can be accomplished by homogeneous reaction with an oxidant (e.g., oxygen) in the solution. Moreover, Cu^{2+} ion adsorption decreases with increasing of total complexation of ions [116]. Since the stability constant, of Cu^{2+}-complexes, is $\sim 10^5$ times that of Cu^{+}-complex [118], then adsorption of Cu^{2+} ions will decrease due to fast total complexation, leading to higher dissolution of copper. On the other hand, Johnson and Leja [52] reported the following free energies for the reactions:

$$\begin{array}{lr} & \Delta G^\circ \\ & \text{(Kcal)} \\ Cu + [Cu(NH_3)_4]^{2+} \longrightarrow 2[Cu(NH_3)_2]^{+} \ldots & -3.72 \quad \ldots \quad (5) \end{array}$$

$$\begin{array}{ll} & \Delta G^\circ \\ & \text{(Kcal)} \\ Zn + [Cu(NH_3)_4]^{2+} \longrightarrow Zn^{2+} + 2[Cu(NH_3)_2]^{+} \;\ldots & -50.84 \;\ldots\; (6) \end{array}$$

Although reaction (6) has a more negative free energy value, it appears to be much slower which indicates either that the activity of zinc in the brass surface is much smaller than expected, or the activation energy for reaction (6) is much higher than for reaction (5). The second assumption is supported by the electrochemical results in the present work, which show higher corrosion rate of pure copper than that of pure zinc in complexing solutions.

The important role of Cu^+-complexes in copper dissolution has been discussed by Hansen [119]. A model for the catalytic oxidation of Cu^+-complexes can be developed in dilute solutions, assuming constant activities of H_2O, NH_3 and O_2. It should be noted that for fast reactions the oxygen may be depleted and reactions may become oxygen transport limited. The catalytic oxidation is assumed to occur according to the following mechanism where Cu^+ and Cu^{++} mean the corresponding ammonia complexes:

$$\text{(I)} \quad 4Cu + O_2 + 2H_2O \xrightarrow{R_1} 4Cu^+ + 4OH^-, \qquad (7)$$

$$\left(\frac{d[Cu]^+}{dt}\right)_I = 4R_1 = \text{constant}$$

$$\text{(II)} \quad 4Cu^+ + O_2 + 2H_2O \xrightarrow{R_2} 4Cu^{++} + 4OH^- \qquad (8)$$

which proceeds by the following steps

$$Cu^+ + O_2 \longrightarrow CuO_2^+ \,, \tag{8a}$$

$$\left(\frac{d[CuO_2^+]}{dt}\right)_a = k_a' \, P_{O_2} [Cu^+] = k_a [Cu^+]$$

$$CuO_2^+ + Cu^+ + 2H_2O \longrightarrow 2Cu^{++} + 2OH^- + H_2O_2 \,, \tag{8b}$$

$$\left(\frac{d[H_2O_2]}{dt}\right)_b = k_b [Cu^+][CuO_2^+]$$

$$Cu^+ + H_2O_2 \longrightarrow CuOH^+ + HO\cdot \,, \tag{8c}$$

$$\left(\frac{d[HO\cdot]}{dt}\right)_c = k_c [Cu^+][H_2O_2]$$

$$Cu^+ + HO\cdot \longrightarrow CuOH^+ \,, \tag{8d}$$

$$\left(\frac{[CuOH^+]}{dt}\right)_d = k_d [Cu^+][HO\cdot]$$

$$CuOH^+ \longrightarrow Cu^{++} + OH^- \,, \tag{8e}$$

$$\left(\frac{d[CuOH^+]}{dt}\right)_e = -k_e [CuOH^+]$$

$$\text{(III)} \quad Cu^{++} + Cu \longrightarrow 2Cu^+ \,, \tag{9}$$

$$\left(\frac{d[Cu^+]}{dt}\right)_{III} = 2k_3 [Cu^{++}]$$

If initial concentrations, at t=0, are zero for $[Cu^+]$, $[Cu^{++}]$, $[H_2O_2]$, $[CuO_2^+]$, $[CuOH^+]$ and $[HO\cdot]$, then amounts of the various species initially will be proportional to t, t^2, t^4, and t^6 for $[Cu^+]$, $[CuO_2^+]$, $[Cu^{++}]$ and H_2O_2, and $[CuOH^+]$ and $[HO\cdot]$, respectively. It should be noted that if the reactions (8a-8e) are fast, then these proportions will not last very long. The steady state conditions can be assumed for CuO_2^+, H_2O_2, $HO\cdot$ and $CuOH^+$ since their concentrations are small due to high reactivity. The steady state assumption may be risky in case of H_2O_2; however, it is necessary to avoid nonlinear differential equations, which can be solved only by numerical methods. According to steady state approximation, the following equations are obtained:

$$\frac{d[CuO_2^+]}{dt} = 0 = k_a[Cu^+] - k_b[CuO_2^+][Cu^+]$$

$$\text{i.e., } [CuO_2^+] = \frac{k_a}{k_b}$$

$$\frac{d[H_2O_2]}{dt} = 0 = k_b[CuO_2^+][Cu^+] - k_c[Cu^+][H_2O_2]$$

$$= k_a[Cu^+] - k_c[Cu^+][H_2O_2]$$

$$\text{i.e., } [H_2O_2] = \frac{k_a}{k_c}$$

$$\frac{d[HO\cdot]}{dt} = 0 = k_c[Cu^+][H_2O_2] - k_d[Cu^+][HO\cdot]$$

$$= k_a[Cu^+] - k_d[Cu^+][HO\cdot]$$

$$\text{i.e., } [HO\cdot] = \frac{k_a}{k_d}$$

$$\frac{d[CuOH^+]}{dt} = k_c[Cu^+][H_2O_2] + k_d[Cu^+][HO\cdot] - k_c[CuOH^+]$$

$$= 2k_a[Cu^+] - k_e[CuOH^+]$$

$$\text{i.e., } [CuOH^+] = \frac{2k_a[Cu^+]}{k_e}$$

Then, for Cu^+-complex growth rate:

$$\frac{d[Cu^+]}{dt} = 4R_1 - [Cu^+]\,\{k_a + k_b[CuO_2^+]$$

$$+ k_c[H_2O_2] + k_d[OH\cdot]\} + 2k_3[Cu^{++}]$$

$$= 4R_1 - 4k_a[Cu^+] + 2k_3[Cu^{++}].$$

and for Cu^{++}-complex growth rate:

$$\frac{d[Cu^{++}]}{dt} = 2k_b[Cu^+][CuO_2^+] + k_e[CuOH^+] - k_3[Cu^{++}]$$

$$= 2k_a[Cu^+] + 2k_a[Cu^+] - k_3[Cu^{++}]$$

$$= 4k_a[Cu^+] - k_3[Cu^{++}]$$

The complete solution of the two differential equations, using Laplace transformations, is shown in Appendix D. The final results show that $[Cu^+]$ initially increases in proportion to t (expected from the initial set of equations) whereas $[Cu^{++}]$ increases in proportion to t^2 (rather than t^4) because the steady state assumption for CuO_2^+ has "masked" that part of the transient behavior.

It is concluded that copper dissolution is favored mostly in complexing ammoniacal and ammonium salts solutions, while zinc dissolution is favored in noncomplexing ammonium salts solutions, and that preferential dissolution is required for SCC to occur in nontarnishing ammoniacal and ammonium salts solutions. On the other hand, protective film formation, general or low corrosion, and presence of inhibiting anions are among the factors decreasing the SCC susceptibility.

Rotating ring disc electrode, RRDE, results The RRDE results on an α-brass (80/20) disc in 1 M NH_4Cl + 0.05 M $CuCl_2$ solution are shown in Figure 26. The ring current increases gradually with increasing disc current, indicating the formation of Cu^+-complexes during the brass disc reaction. The ring residual current is obtained under the same conditions but in 1 M $NaNO_3$ + 0.05 M $Cu(NO_3)_2$ solution of the same pH. No change in ring current is observed in spite of the increasing

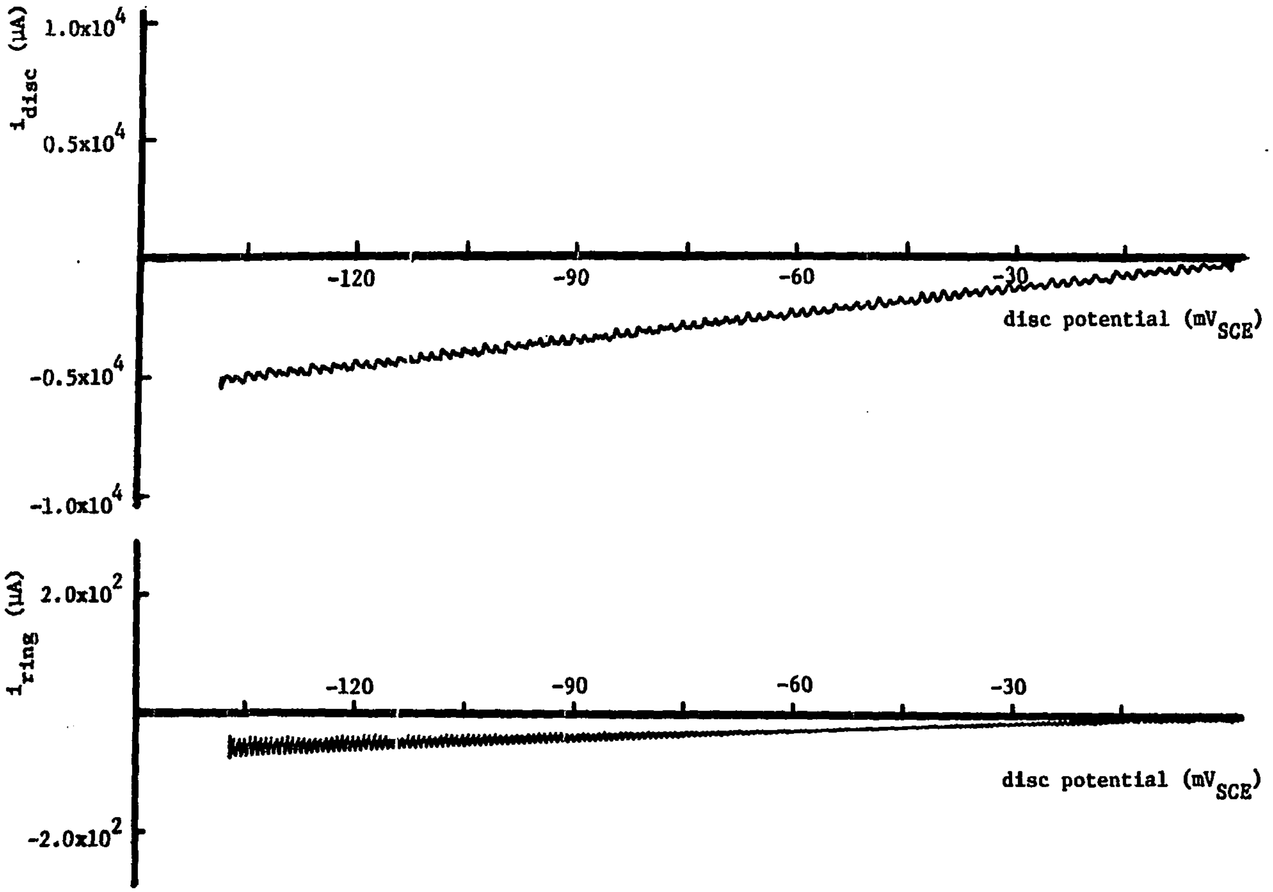

rotation velocity = 500 rpm
scan rate = 500 mV/min
disc potential = -150 → 0.00 mV$_{SCE}$
ring potential = +260 mV$_{SCE}$

Figure 26. I_d-E_d and I_r-E_d for Cu^{++} in 1 M NH_4Cl + 0.05 M $CuCl_2$ solution, pH=3.5, using an α-brass (80/20) disc and a platinum ring

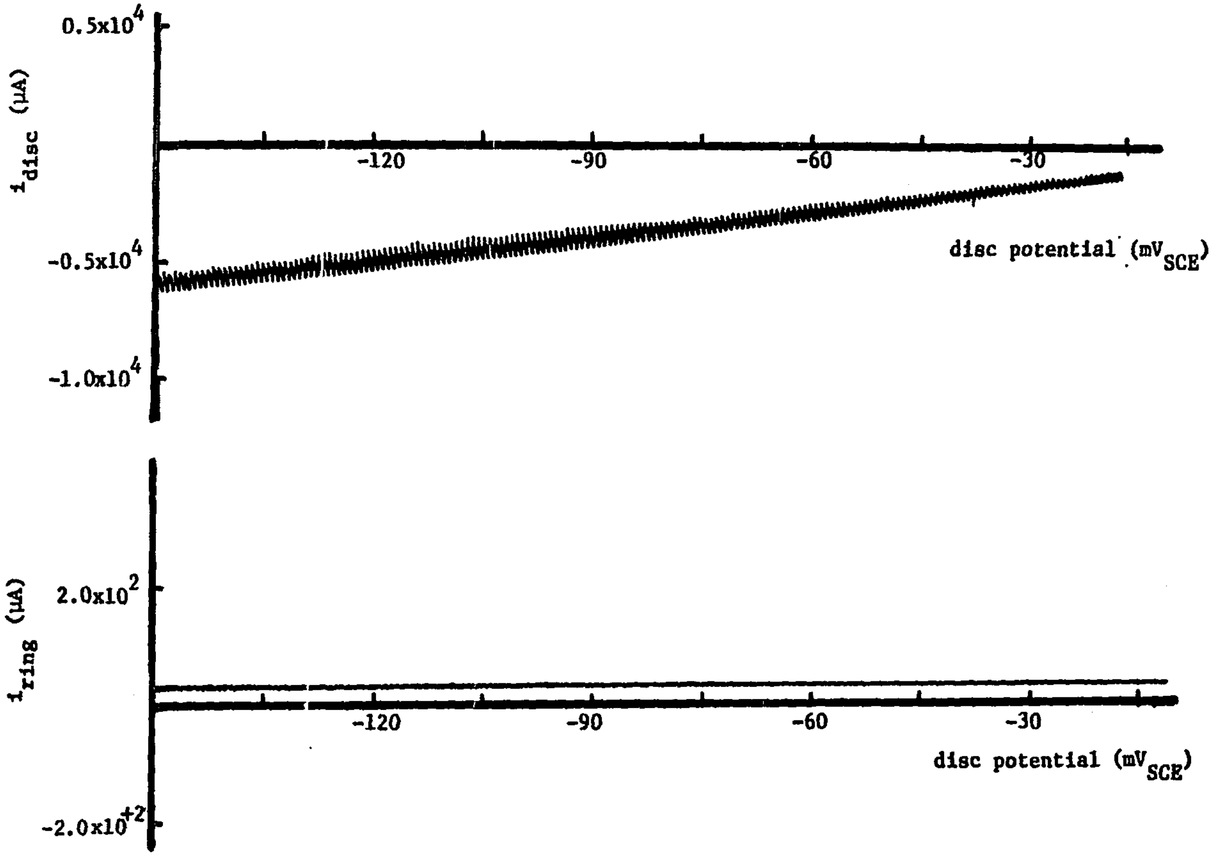

rotation velocity = 500 rpm
scan rate = 500 mV/min
disc potential = -150 → 0.0 mV_{SCE}
ring potential = +260 mV_{SCE}

Figure 27. I_d-E_d and I_r-E_d for Cu^{++} in 1 M $NaNO_3$ + 0.05 M $Cu(NO_3)_2$ solution, pH=3.5, using an α-brass (80/20) disc and a platinum ring

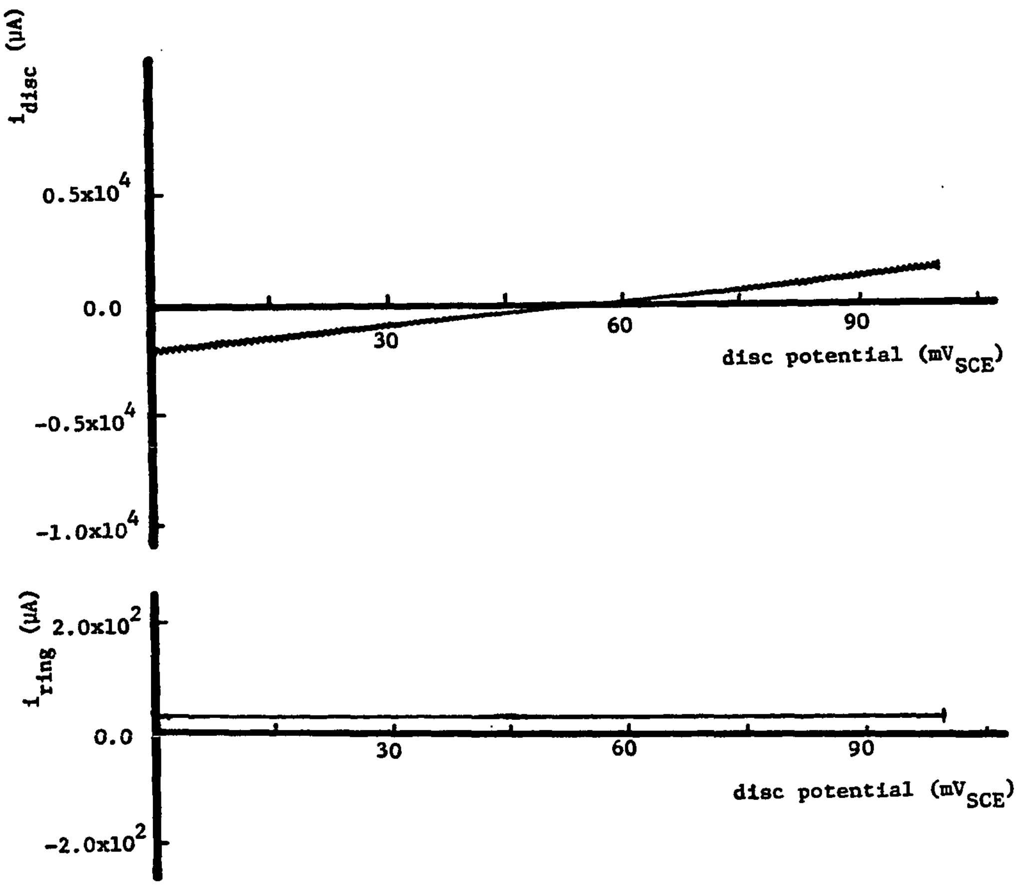

rotation velocity = 500 rpm
scan rate = 500 mV/min
disc potential = 0.0 → 100 mV_{SCE}
ring potential = +260 mV_{SCE}

Figure 28. I_d-E_d and I_r-E_d for Cu^{++} in 1 M $NaNO_3$ + 0.05 M $Cu(NO_3)_2$ solution, pH=4.1, using an α-brass (80/20) disc and a platinum ring

brass disc current (Figure 27), which indicates the absence of any Cu^+-ion formation. Figure 28 shows the disc and ring currents in the latter solution at cathodic and anodic potentials w.r.t. the brass corrosion potential in this solution. While the brass disc current changes from cathodic to anodic region at almost the brass corrosion potential value, no change in ring current is observed. The results present a strong support for the presence of Cu^+-complexes in the $NH_4Cl + CuCl_2$ solution, predicted from Tafel plot measurements. However, no ring current could be observed in Mattsson's solution, which may be attributed to the very fast oxidation of Cu^+-complexes into the much more stable Cu^{2+}-complexes.

<u>Cyclic polarization measurement results</u> The cyclic polarization curves of $\alpha\beta'$-brass (60/39) (Figures 29-38) were obtained by scanning the potential of the brass sample from cathodic potentials (about -250 mV w.r.t. E_{cor}) to anodic potentials (about +250 mV w.r.t. E_{cor}), then back to the initial cathodic potential. It is interesting to note the following features of cyclic polarization curves in solutions where sample cracking occurred, i.e., Figures 29-33:

a. The reverse anodic branch has always higher current values than (and appreciably removed from) the original anodic branch.

b. The potential at which the reverse scan current changes sign (from anodic to cathodic current, i.e., zero-current potential) is less noble than the original value of E(I=0) or E_{cor}.

c. At E_{cor}, the value of the current on the reverse anodic branch is ≥ 10 mA/cm^2.

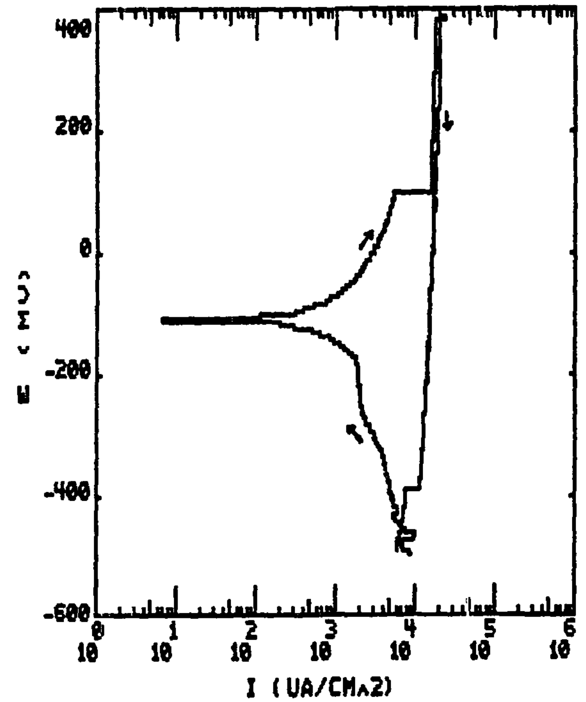

Figure 29. Cyclic polarization curve for αβ'-brass (60/39) electrode in 1 M NH_4OH + 0.05 M $CuSO_4$ solution at 25°C

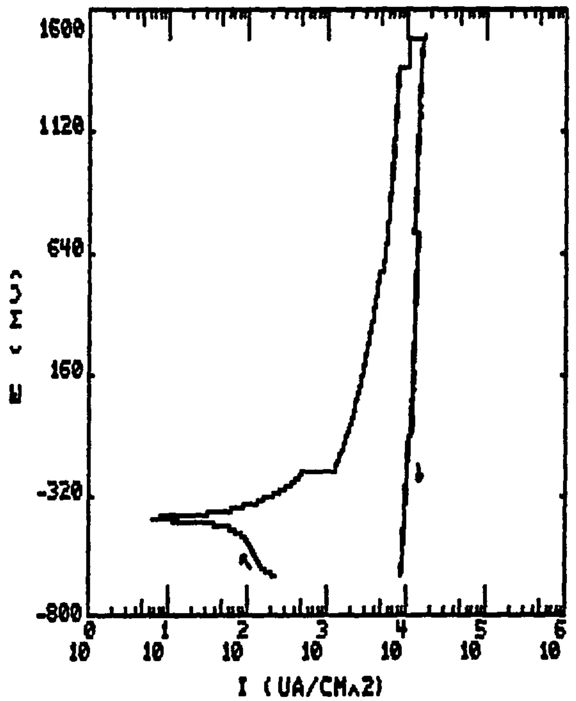

Figure 30. Cyclic polarization curve for αβ'-brass (60/39) electrode in 1 M NH_4OH solution at 25°C

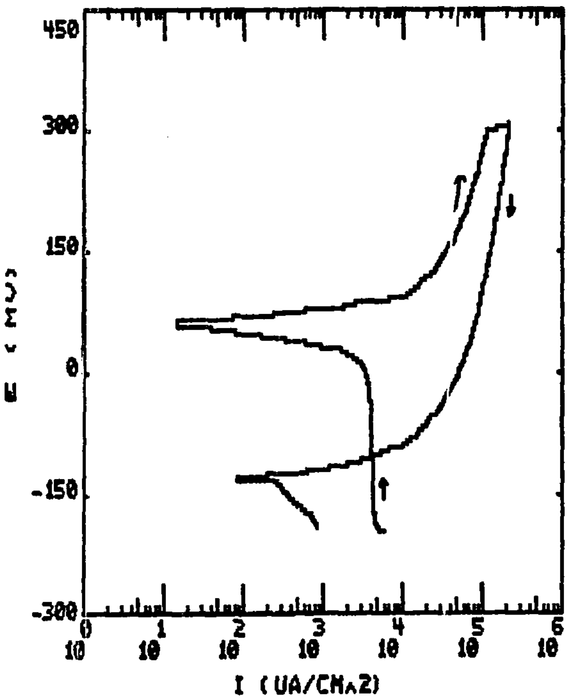

Figure 31. Cyclic polarization curve for $\alpha\beta'$-brass (60/39) electrode in 1 M NH_4NO_3 + 0.05 M $Cu(NO_3)_2$ solution at 25°C

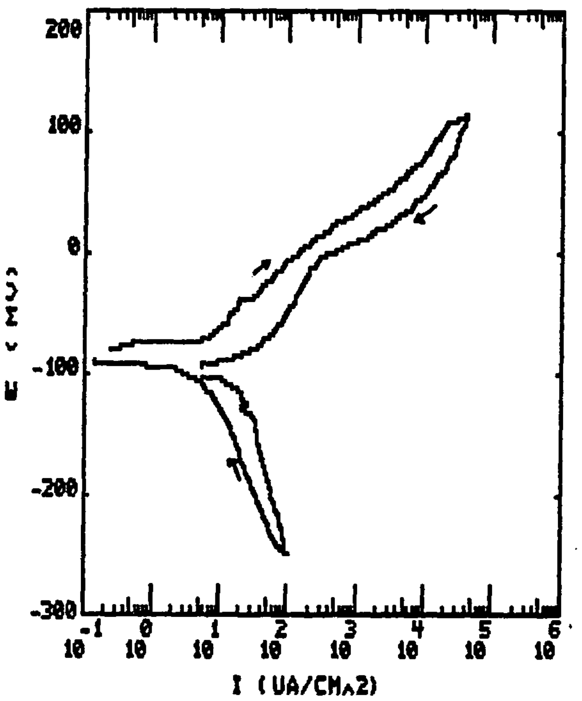

Figure 32. Cyclic polarization curve for $\alpha\beta'$-brass (60/39) electrode in 1 M NH_4NO_3 solution at 25°C

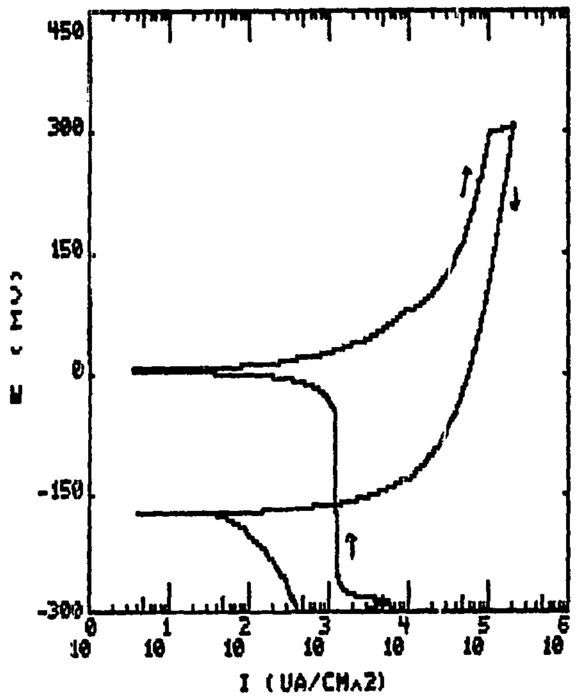

Figure 33. Cyclic polarization curve for αβ'-brass (60/39) electrode in 1 M $(NH_4)_2SO_4$ + 0.05 M $CuSO_4$ solution at 25°C

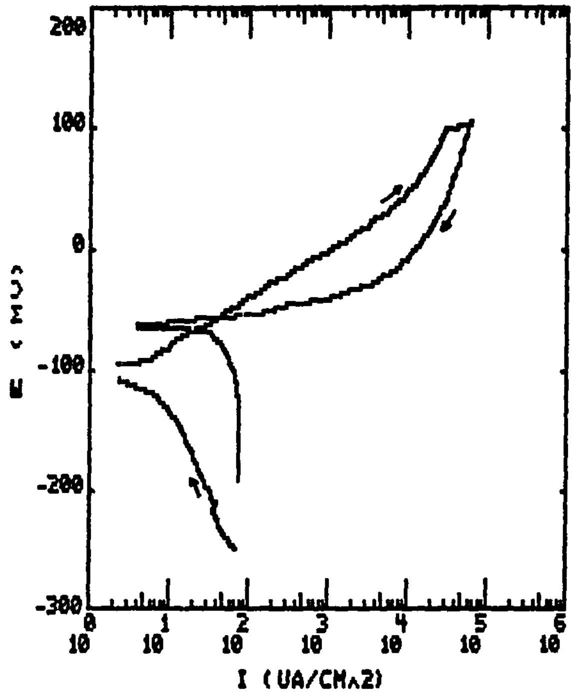

Figure 34. Cyclic polarization curve for αβ'-brass (60/39) electrode in 1 M $(NH_4)_2SO_4$ solution at 25°C

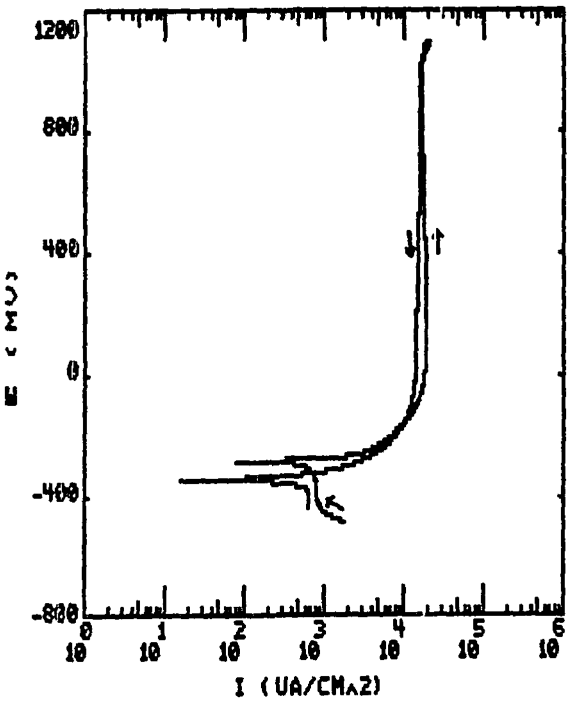

Figure 35. Cyclic polarization curve for αβ'-brass (60/39) electrode in 1 M $(NH_4)_2CO_3$ + 0.05 M $CuSO_4$ solution at 25°C

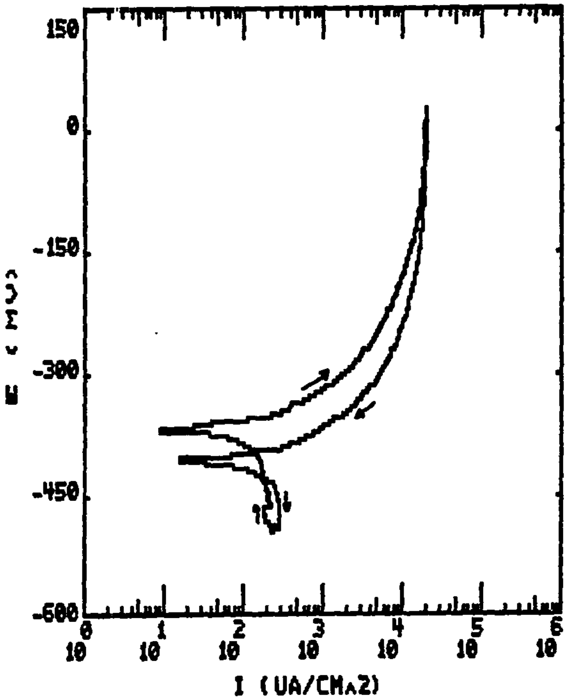

Figure 36. Cyclic polarization curve for αβ'-brass (60/39) electrode in 1 M $(NH_4)_2CO_3$ solution at 25°C

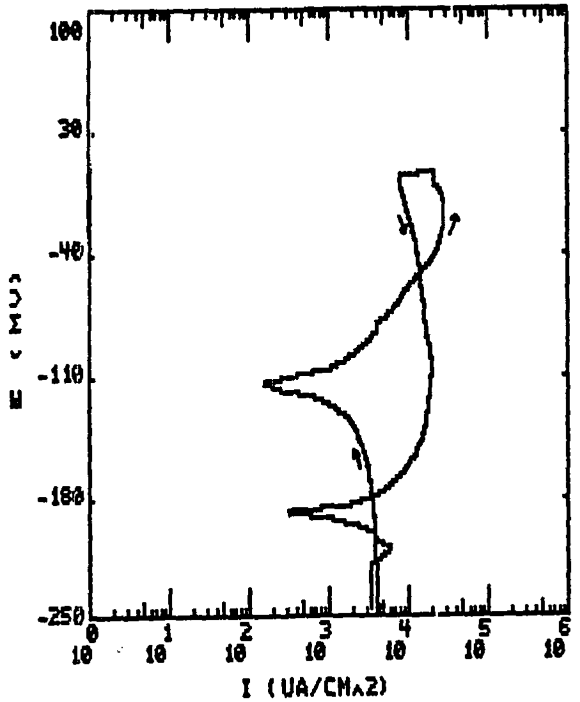

Figure 37. Cyclic polarization curve for αβ'-brass (60/39) electrode in 1 M NH_4Cl + 0.05 M $CuCl_2$ solution at 25°C

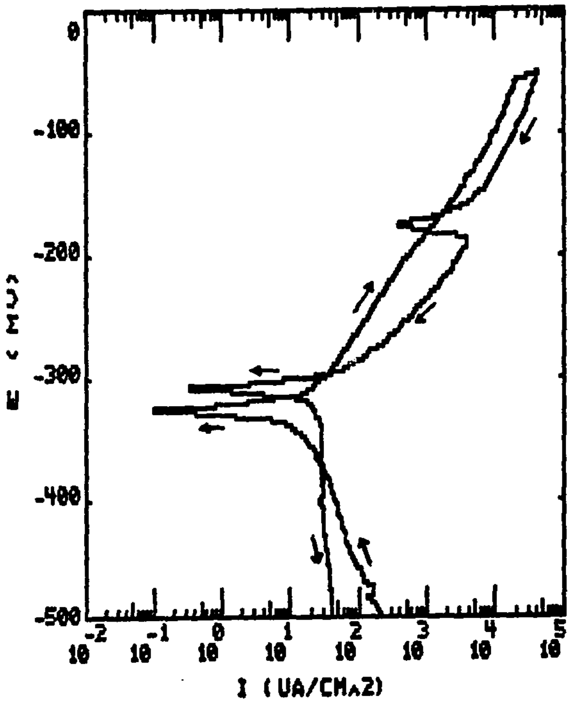

Figure 38. Cyclic polarization curve for αβ'-brass (60/39) electrode in 1 M NH_4Cl solution at 25°C

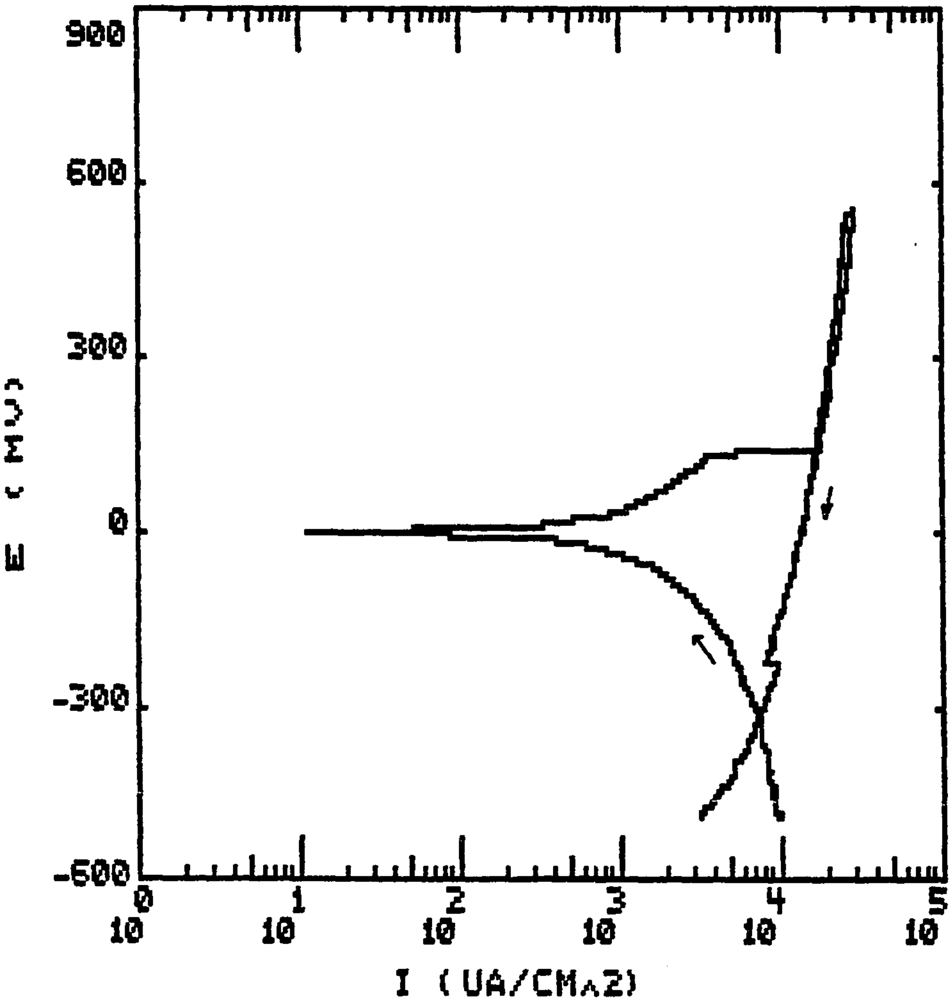

Figure 39. Cyclic polarization curve for α-brass (80/20) electrode in 1 M NH_4OH + 0.05 M $CuSO_4$ solution at 25°C

The same features are noticed for α-brass (80/20) in Mattsson's solution (Figure 39). On the other hand, in Figures 34-38, it is clear that not all of these features are present in the case of solutions where no cracking occurred.

Cyclic polarization curves at constant scan rate were used to predict pit formation [120-121], while SCC prediction was obtained from cyclic polarization curves at two different scans, mainly fast forward and slow reverse sweeps [122-123]. Parkins and Holroyd [72] suggested that SCC can be predicted to occur in the potential range where a fast (~1 V/min) and a slow (~10 mV/min) sweep rate potentiokinetic curves show appreciable current density displacement (~1 mA/cm^2). They suggested that the fast and slow sweep rates reflect the activities of crack tip and sides, respectively. The present results show that SCC may be predicted to occur in a solution (at open circuit potential and constant load) if the corresponding cyclic polarization curve, at constant scan rate, satisfies the following features:

1. The reverse anodic branch has always higher current values than the forward branch, and attains a value $\geq$ 10 mA/cm^2 at the original corrosion potential.
2. The zero-current potential, attained by the reverse branch, is always less noble than the original corrosion potential.

These features may indicate the possible formation of pits, which are formed during the initiation stage of the SCC mechanism. The formation of pits will increase the anodic corroding area, hence, the anodic current values on the reverse branch will be higher than those on the original one. Moreover, the decrease in anodic polarization due to pit formation will result in less noble corrosion potential [11].

Surface analysis tests

All surface analysis tests were done on $\alpha\beta'$-brass (60/39) loop samples.

Energy dispersive x-ray analysis (EDAX) results The analysis fundamentals are discussed in Appendix E. The EDAX analysis of the original untreated sample is shown in Figure 40. The brass consists mainly of Cu and Zn, in the ratio of $\frac{62\cdot62}{33\cdot66} = 1.86$. Impurities of Fe and Sn were also detected. The analysis of samples failed in different solutions is discussed below.

1 M NH_4OH + 0.05 M $CuSO_4$ Three different samples of different immersion times were analyzed:

1. Immersion time of 4.5 hours: The analysis of the crack surface showed that Zn-enrichment or Cu-depletion is a feature of the whole cracking surface. The ratio of Cu/Zn decreases from 1.86 in the mechanically fractured region to ~1.3 on the crack surface (Figure 41). The same result was found also for the sample surface analysis.

2. Immersion time of 32 hours: The analysis showed that near the crack tip, the Zn enrichment or the Cu-depletion is even more pronounced. Cu/Zn ratio is 0.25 (Figure 42). However, approaching the crack initiation area, the region is Cu-rich.

3. Immersion time of 4 days: The analysis of the crack surface behind the crack tip showed the presence of a Zn-rich region. The presence of a big ZnO particle behind the crack tip is revealed in Figure 43. The structure was confirmed by EDAX analysis shown in Figure 44. However, moving away from the crack tip, in the direction of the crack intiation region, the analysis showed a Cu-rich region (Figure 45). Moreover, the sample surface was found to be Cu-rich.

```
No. of Iterations  0
----      K        [Z]      [A]      [F]     [ZAF]   ATOM.%   WT.%
CU-K   0.631    1.006    1.000    1.000    1.007    62.62    63.39
ZN-K   0.349    0.995    0.999    1.000    0.995    33.66    34.61
SN-L   0.002    1.261    1.035    0.993    1.297     0.14     0.26
FE-K   0.011    0.957    1.007    0.844    0.814     1.05     0.93
SI-K   0.002    0.776    2.007    0.999    1.558     0.85     0.37  *
O -K   0.003    0.705    1.983    0.999    1.399     1.68     0.42  *
 * - High Absorbance
```

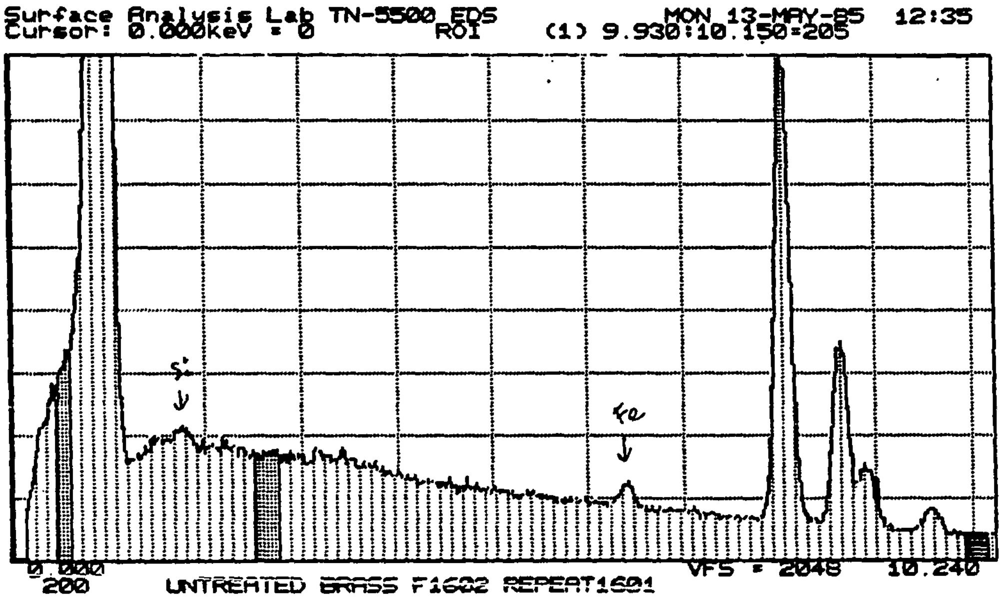

Figure 40. Energy dispersive x-ray (EDAX) analysis of untreated sample of αβ'-brass. Cu/Zn = 1.86

```
No. of Iterations  0
----      K      [Z]     [A]     [F]    [ZAF]  ATOM.%  WT.%
CU-K  0.552  1.001   1.000   1.000   1.002   56.13   55.39
ZN-K  0.436  0.991   0.999   1.000   0.991   43.09   43.18
SN-L  0.011  1.255   1.036   0.994   1.293    0.78    1.43
 * - High Absorbance
```

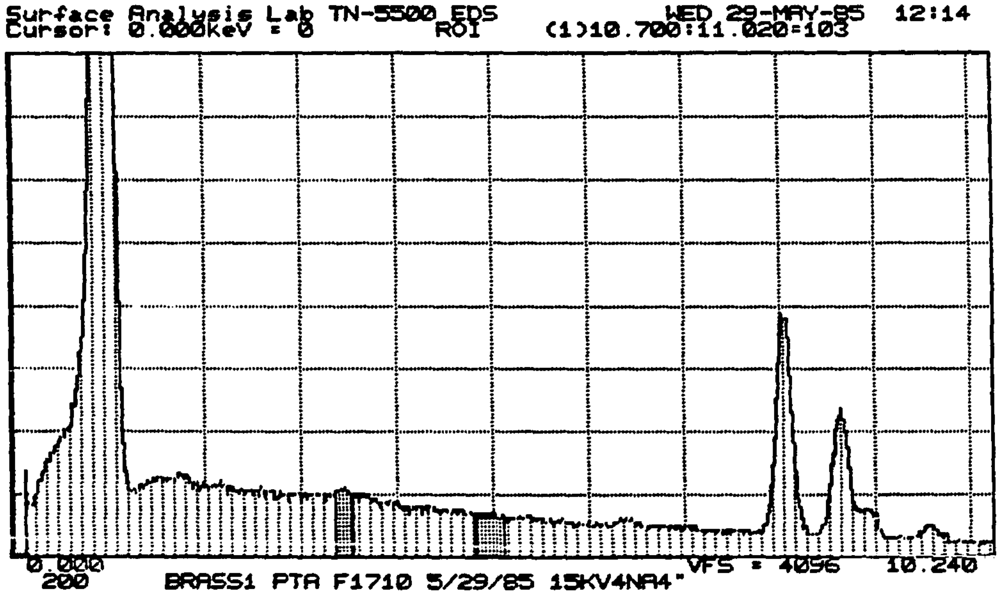

Figure 41. Energy dispersive x-ray (EDAX) analysis of crack surface in αβ'-brass loop specimen cracked in 1 M NH_4OH + 0.05 M $CuSO_4$. Immersion time 4.5 hr, Cu/Zn = 1.30

```
No. of Iterations  1
----      K       [Z]     [A]     [F]    [ZAF]   ATOM.%  WT.%
CU-K  0.180   1.022   1.001   1.000   1.024   15.59   17.78
ZN-K  0.742   1.012   1.000   1.000   1.012   62.36   72.23
SN-L  0.028   1.281   1.035   0.995   1.320    1.71    3.62
FE-K  0.007   0.972   1.010   0.885   0.870    0.67    0.66
SI-K  0.001   0.788   2.015   0.999   1.589    0.42    0.21  *
O -K  0.039   0.717   2.038   0.999   1.463   19.26    5.49  *
 * - High Absorbance
```

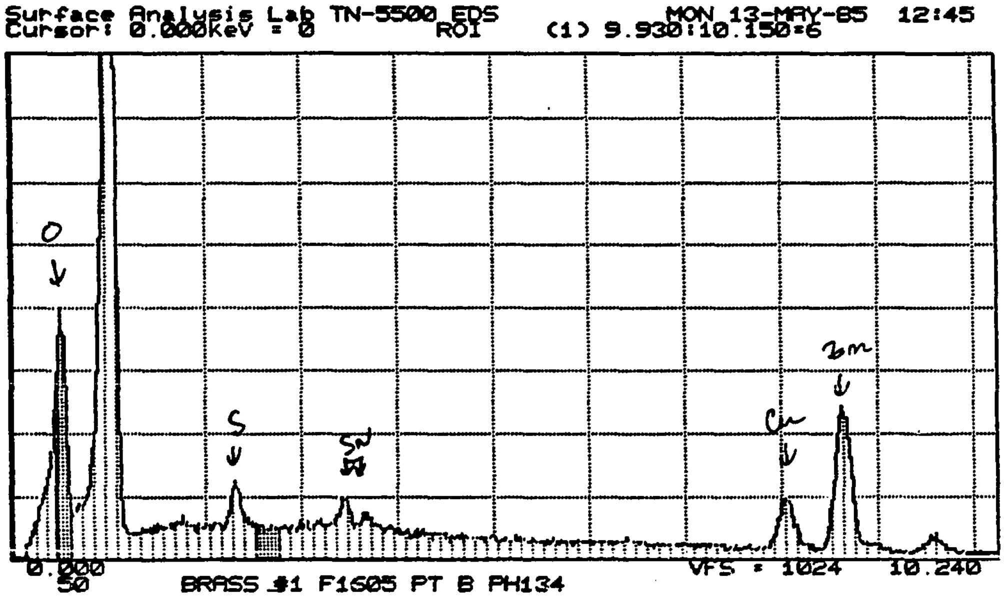

Figure 42. Energy dispersive x-ray (EDAX) analysis of crack surface in αβ'-brass loop specimen cracked in 1 M NH_4OH + 0.05 M $CuSO_4$. Immersion time 32 hr, Cu/Zn = 0.25

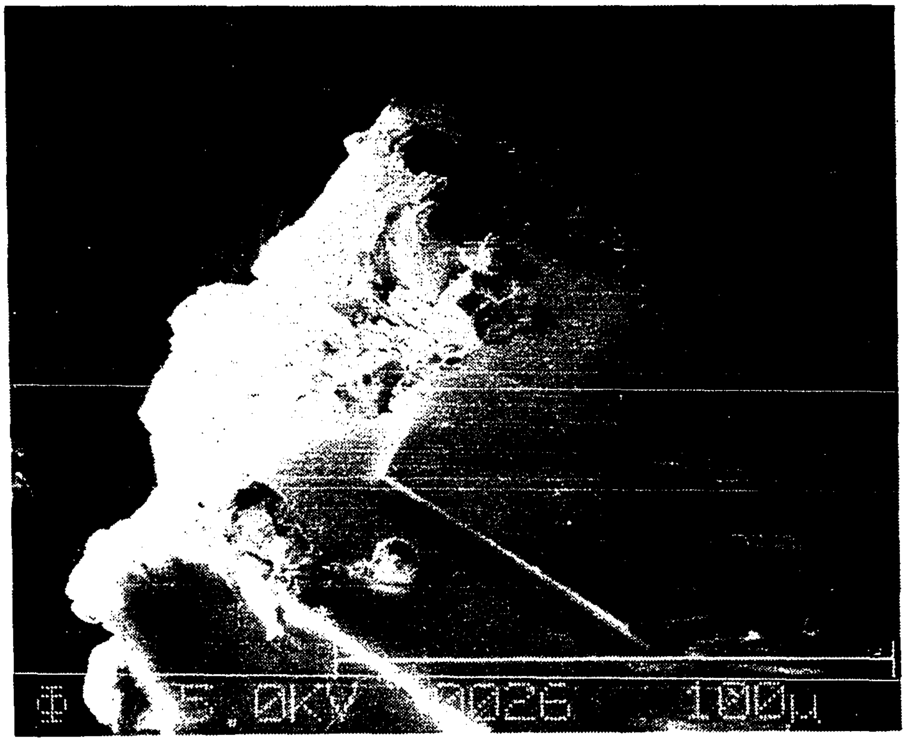

Fig. 43. Scanning electron micrograph of ZnO crystal detected on the crack surface on αβ'-brass (60/39) loop sample in 1 M NH_4OH + 0.05 M $CuSO_4$ solution. The immersion time is 4 days

```
No. of Iterations  3
----     K       [Z]     [A]      [F]    [ZAF]   ATOM.%  WT.%
CU-K  0.027   1.085   0.999   1.000   1.085    1.67    2.63
ZN-K  0.811   1.073   0.999   1.000   1.072   47.80   76.76
O -K  0.151   0.766   1.918   0.999   1.470   49.55   19.59  *
FE-K  0.006   1.033   1.005   0.883   0.918    0.37    0.52
SN-L  0.000   1.364   1.025   0.995   1.393    0.04    0.11
S -K  0.000   0.864   1.394   0.999   1.204    0.00    0.00 G
SI-K  0.002   0.841   1.950   0.999   1.641    0.56    0.39  *
 * - High Absorbance
```

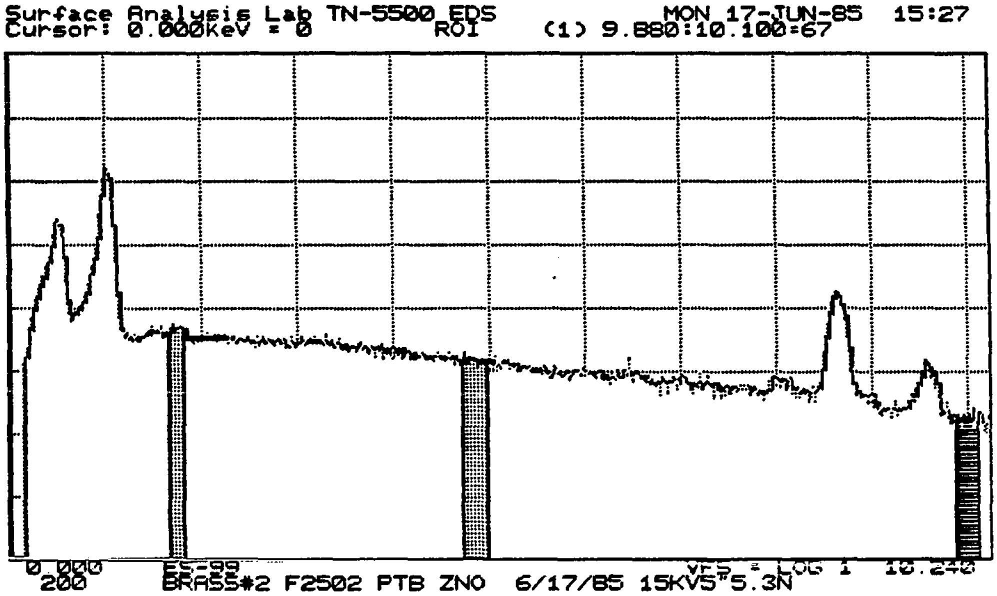

Figure 44. Energy dispersive x-ray (EDAX) analysis of ZnO crystal shown in Figure 43

```
No. of Iterations  2
----      K       [Z]     [A]     [F]     [ZAF]   ATOM.%  WT.%
CU-K  0.807  1.009  1.000  1.000  1.010  76.26  80.71
ZN-K  0.155  0.998  0.999  1.000  0.998  14.28  15.35
O -K  0.014  0.708  1.941  0.999  1.375   7.58   2.00   *
FE-K  0.019  0.960  1.006  0.837  0.809   1.70   1.57
SN-L  0.002  1.265  1.030  0.993  1.295   0.19   0.37
S -K  0.000  0.800  1.409  0.999  1.127   0.00   0.00 G *
SI-K  0.000  0.779  1.977  0.999  1.540   0.00   0.00 G *
 * - High Absorbance
```

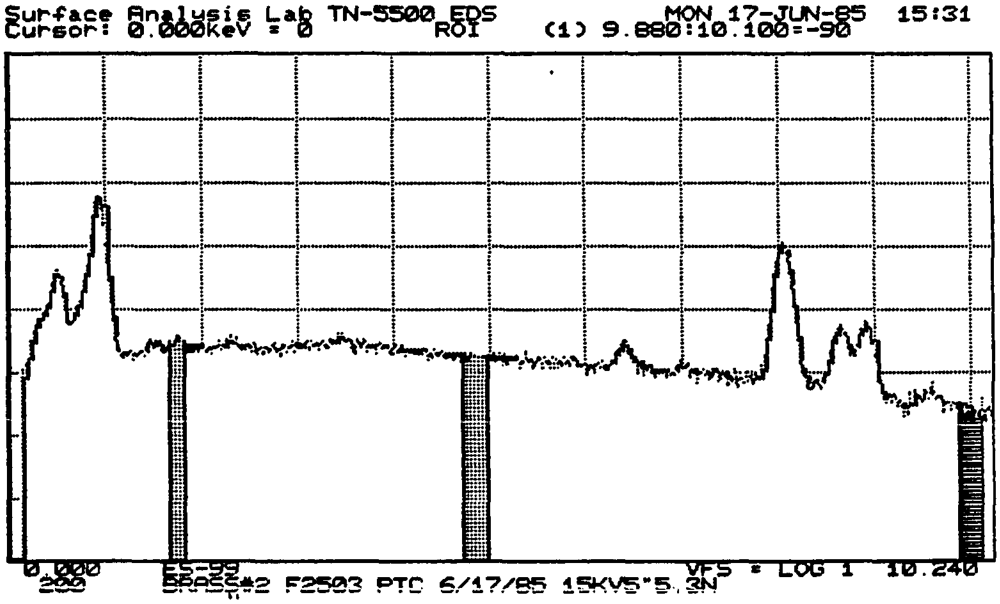

Figure 45. Energy dispersive x-ray (EDAX) analysis of crack surface (near initiation region) in αβ'-brass loop specimen cracked in 1 M NH_4OH + 0.05 M $CuSO_4$ solution. Immersion time 4 days, Cu/Zn = 5.34

<u>1 M NH_4OH</u> Results were similar to those obtained in the last solution. The analysis of a sample removed from the solution just after visible crack propagation revealed that near the crack tip the surface is Zn-rich (Figure 46). However, it is Cu-rich near the initiation point (Figure 47), and even more Cu-rich on the sample surface. ZnO particles were also detected near the crack tip in a sample picked out later from the solution. In the same sample, the Cu-enrichment away from the crack tip was more pronounced.

<u>1 M NH_4NO_3 + 0.05 M $Cu(NO_3)_2$</u> The cracking in this solution propagated from the outer surface (where stresses are tensile) to the inner surface (where stresses are compressive) in an oblique line (Figure 48). The EDAX analysis shows more Zn-depletion near the crack tip (Figure 49), than in the initiation region (Figure 50).

<u>1 M NH_4NO_3</u> The analysis of a sample removed from the solution shortly after crack propagation showed that the whole cracking surface was slightly Cu-depleted (Figure 51). The sample surface showed the same slight Cu-depletion.

<u>1 M $(NH_4)_2SO_4$ + 0.05 M $CuSO_4$</u> The EDAX analysis shows that the cracking surface is Cu-rich (Figure 52), and Cu increases toward the crack initiation region. Moreover, the outer surface away from the crack was found to be more Cu-rich than the outer surface around the crack, which was also Cu-rich. The outer surface away from the crack seems to act as a cathode (where copper deposits), hence, becomes more rich in copper.

```
No. of Iterations  1
----      K      [Z]     [A]     [F]    [ZAF]   ATOM.%  WT.%
CU-K  0.604  1.005  1.000  1.000  1.006  59.77  60.57
ZN-K  0.377  0.995  0.999  1.000  0.995  36.32  37.38
O -K  0.005  0.705  1.986  0.999  1.400   2.77   0.70  *
FE-K  0.008  0.956  1.007  0.847  0.816   0.80   0.71
SN-L  0.004  1.260  1.035  0.994  1.296   0.34   0.64
S -K  0.000  0.797  1.424  0.999  1.134   0.00   0.00 G *
SI-K  0.000  0.775  2.011  0.999  1.560   0.00   0.00 G *
 * - High Absorbance
```

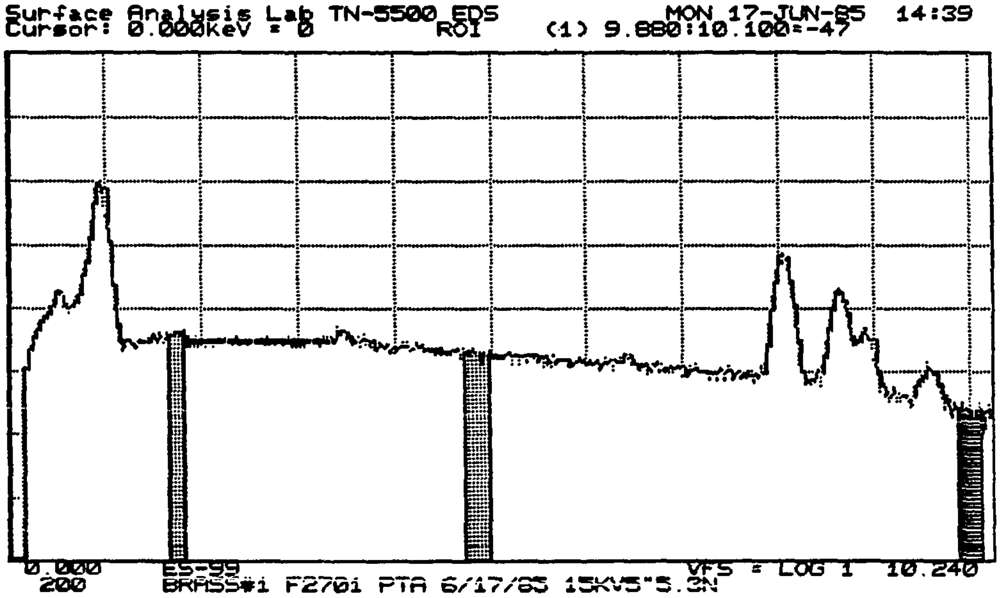

Figure 46. Energy dispersive x-ray (EDAX) analysis of crack surface in αβ'-brass loop specimen cracked in 1 M NH_4OH solution. Cu/Zn = 1.65

```
No. of Iterations  1
----       K       [Z]      [A]      [F]     [ZAF]   ATOM.%   WT.%
CU-K   0.640   1.006   1.000   1.000   1.007   62.42   64.04
ZN-K   0.336   0.996   0.999   1.000   0.996   31.94   33.29
O -K   0.007   0.706   1.981   0.999   1.398    4.14    1.06  *
FE-K   0.008   0.957   1.007   0.845   0.816    0.73    0.66
SN-L   0.006   1.261   1.034   0.993   1.297    0.42    0.80
S -K   0.000   0.797   1.422   0.999   1.133    0.00    0.00 G *
SI-K   0.000   0.776   2.006   0.999   1.556    0.34    0.15  *
 * - High Absorbance
```

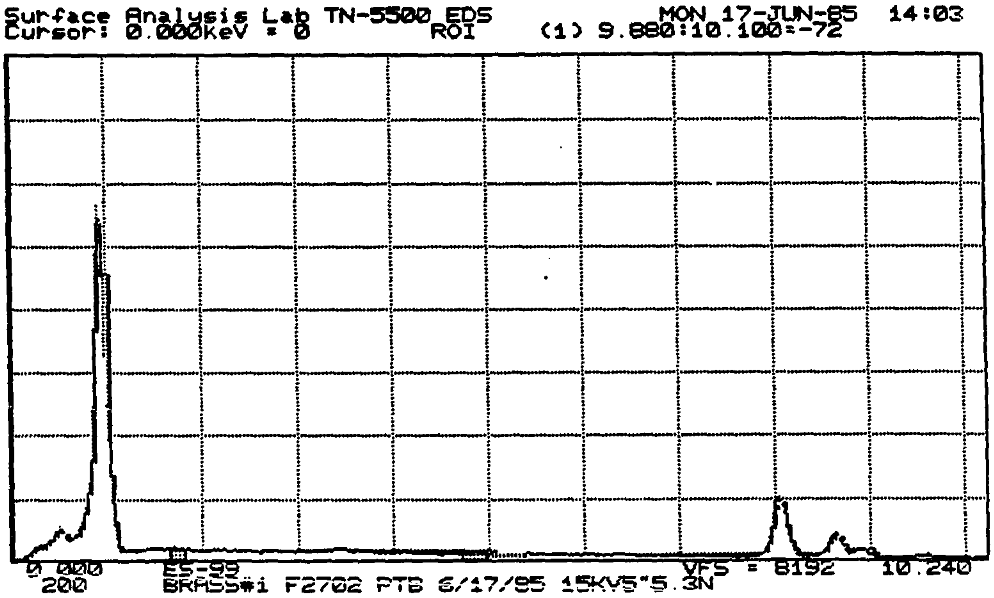

Figure 47. Energy dispersive x-ray (EDAX) analysis of crack surface (near initiation region) in αβ'-brass loop specimen cracked in 1 M NH_4OH solution. Cu/Zn = 1.95

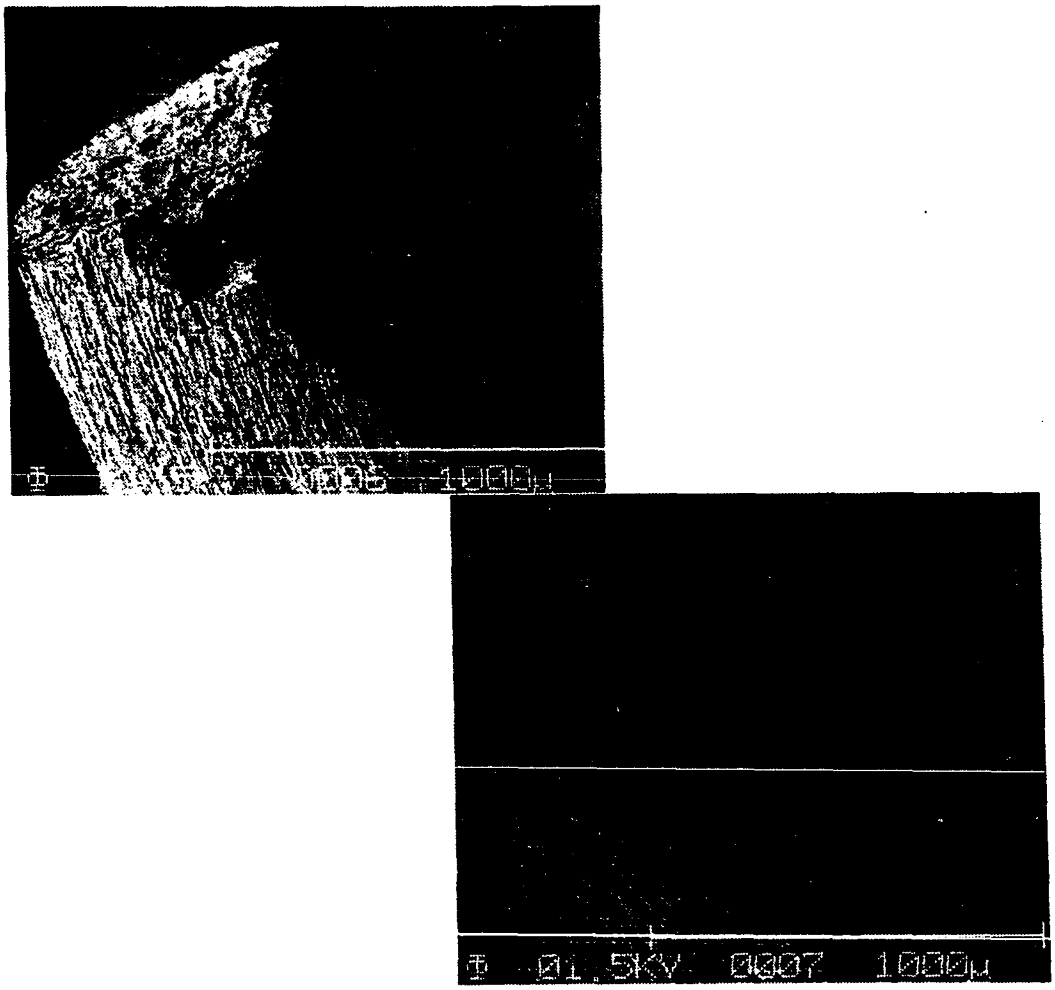

Fig. 48. Scanning electron micrograph of SCC crack on αβ'-brass (60/39) loop sample in 1 M NH_4NO_3 + 0.05 M $Cu(NO_3)_2$ solution at 25° C, illustrating the propagation of the crack from the outer to the inner surface

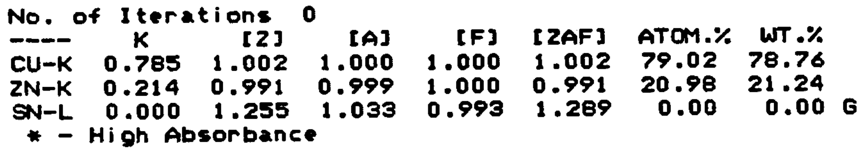

```
No. of Iterations  0
----      K        [Z]      [A]      [F]     [ZAF]   ATOM.%   WT.%
CU-K   0.785    1.002    1.000    1.000    1.002    79.02   78.76
ZN-K   0.214    0.991    0.999    1.000    0.991    20.98   21.24
SN-L   0.000    1.255    1.033    0.993    1.289     0.00    0.00 G
 * - High Absorbance
```

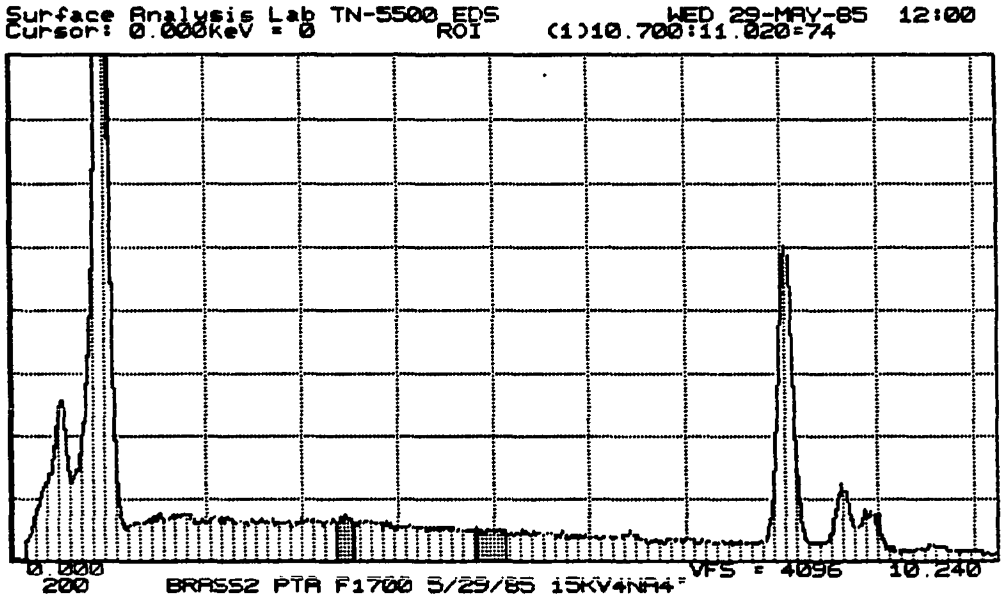

Figure 49. Energy dispersive x-ray (EDAX) analysis of crack surface in αβ'-brass loop specimen cracked in 1 M NH_4NO_3 + 0.05 M $Cu(NO_3)_2$ solution. Cu/Zn = 3.77

```
No. of Iterations  2
----      K      [Z]     [A]     [F]    [ZAF]   ATOM.%  WT.%
CU-K   0.689  1.010  1.000  1.000  1.011   64.29  68.57
ZN-K   0.282  0.997  0.999  1.000  0.997   25.57  27.70
SN-L   0.009  1.266  1.032  0.993  1.299    0.59   1.18
O -K   0.018  0.708  1.968  0.999  1.395    9.54   2.55  *
 * - High Absorbance
```

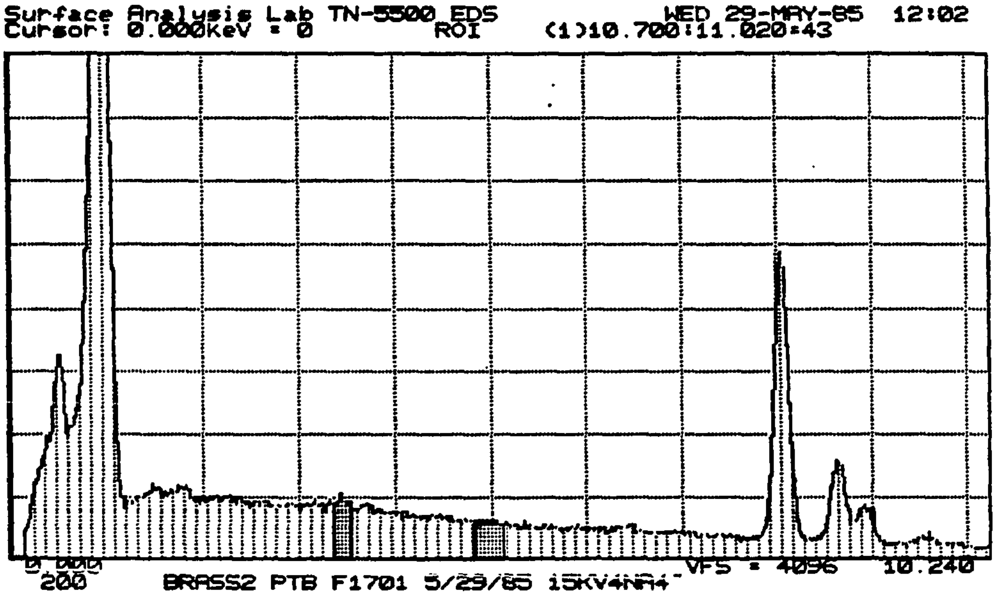

Figure 50. Energy dispersive x-ray (EDAX) analysis of crack surface (near initiation region) in αβ'-brass loop specimen cracked in 1 M NH_4NO_3 + 0.05 M $Cu(NO_3)_2$ solution. Cu/Zn = 2.51

```
No. of Iterations  1
----     K       [Z]     [A]     [F]     [ZAF]   ATOM.%  WT.%
CU-K  0.567   1.003   1.000   1.000   1.004   57.45   57.03
ZN-K  0.420   0.993   0.999   1.000   0.993   41.40   41.73
O -K  0.000   0.703   1.995   0.999   1.404    0.00    0.00 G *
FE-K  0.008   0.955   1.007   0.848   0.816    0.78    0.68
SN-L  0.004   1.257   1.036   0.994   1.295    0.29    0.53
S -K  0.000   0.795   1.428   0.999   1.135    0.00    0.00 G *
SI-K  0.000   0.774   2.020   0.999   1.563    0.08    0.04  *
 * - High Absorbance
```

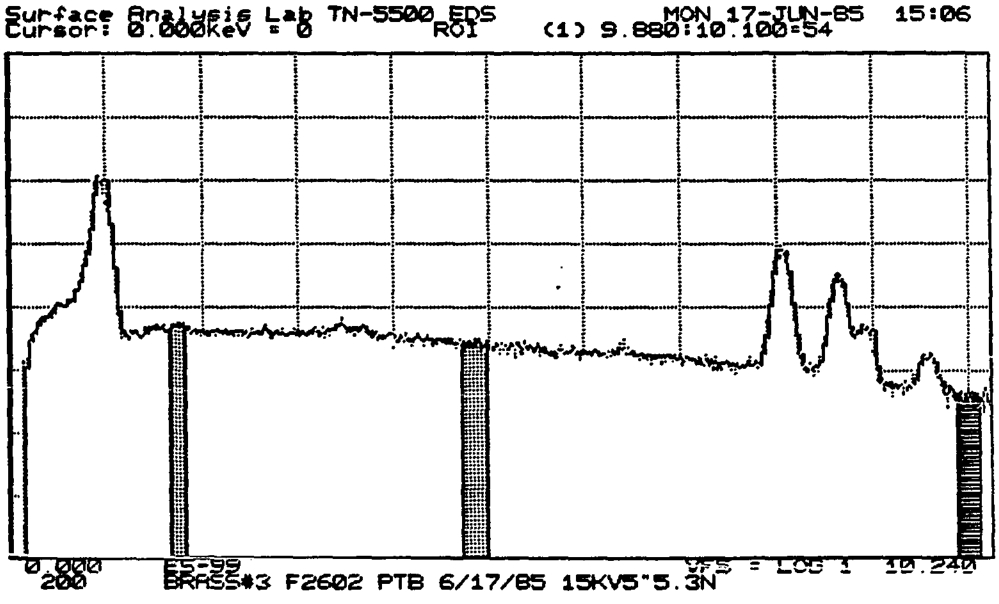

Figure 51. Energy dispersive x-ray (EDAX) analysis of crack surface in αβ'-brass loop specimen cracked in 1 M NH_4NO_3 solution. Cu/Zn = 1.39

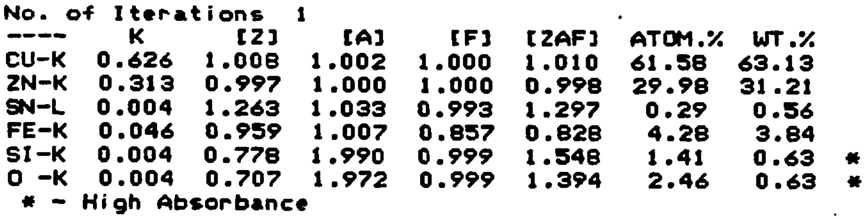

```
No. of Iterations  1
----     K      [Z]     [A]     [F]    [ZAF]   ATOM.%  WT.%
CU-K  0.626   1.008   1.002   1.000   1.010   61.58  63.13
ZN-K  0.313   0.997   1.000   1.000   0.998   29.98  31.21
SN-L  0.004   1.263   1.033   0.993   1.297    0.29   0.56
FE-K  0.046   0.959   1.007   0.857   0.828    4.28   3.84
SI-K  0.004   0.778   1.990   0.999   1.548    1.41   0.63  *
O -K  0.004   0.707   1.972   0.999   1.394    2.46   0.63  *
 * - High Absorbance
```

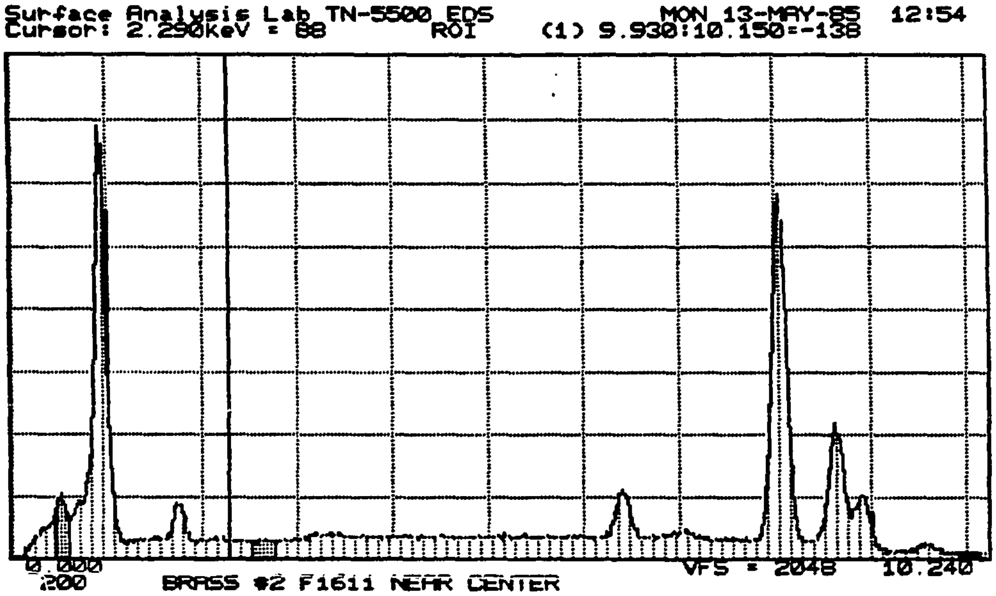

Figure 52. Energy dispersive x-ray analysis of crack surface in αβ'-brass loop specimen cracked in 1 M $(NH_4)_2SO_4$ + 0.05 M $CuSO_4$ solution. Cu/Zn = 2.05

Scanning electron microscopy (SEM) results Two micrographs of the crack surface $\alpha\beta'$-brass (60/39) in 1 M NH_4OH + 0.05 M $CuSO_4$ solution, are shown in Figures 53 and 54. The presence of two different regions, the SCC surface and the post-test mechanical fracture surface region, is clearly shown. The details of the mechanical fracture surface are shown in Figure 53, where the ductile fracture character can be easily recognized.

The SCC surface together with the post-test mechanical fracture surface are shown in Figure 54. The SCC surface is free of true cleavage features or genuine fatigue striations [124], and more nearly resembles an etched surface as might be expected in the dissolution mechanism.

Optical microscopy results Two phases were identified under optical microscope, which is consistent with the phase diagram for Cu-Zn alloy at (60/39) composition. The cracks in all solutions were transgranular and branching. Figure 55 shows a cracking sample in 1 M NH_4OH + 0.05 M $CuSO_4$ solution, at 400X. It is noteworthy that this is the only sample where chemical deposits were detected on the crack surface. The same results were obtained for a cracking sample in 1 M NH_4OH solution; however, a small crack (other than the main one) showed a discontinuous type of propagation, Figure 56 at 400X. The main crack had the same features as the last sample. In 1 M NH_4NO_3 solution, the cracking began on the outer surface and propagated longitudinally along the

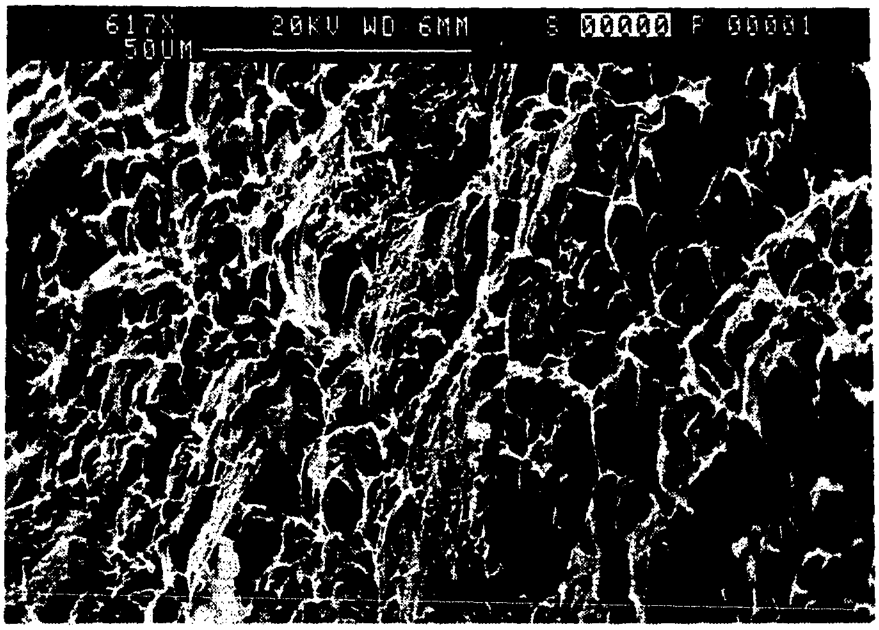

Fig. 53. Scanning electron micrograph of the mechanically-fractured (post-test) surface on $\alpha\beta'$-brass (60/39) loop sample in I M NH_4OH + 0.05 M $CuSO_4$ solution at 25° C

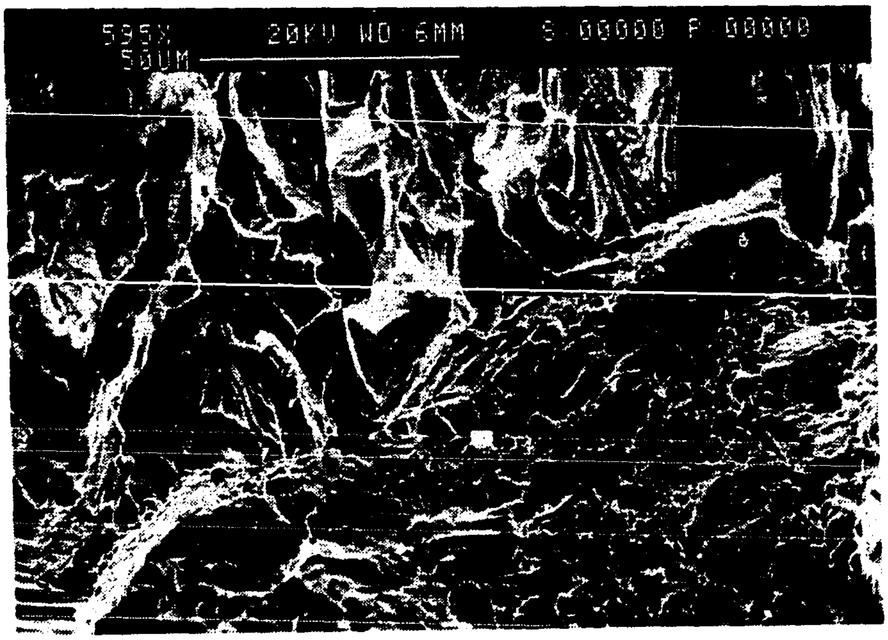

Fig. 54. Scanning electron micrograph showing the difference between the post-test and the SCC surfaces on $\alpha\beta'$-brass (60/39) loop sample in 1 M NH_4OH + 0.05 M $CuSO_4$ solution at 25° C

Fig. 55. Optical micrograph of transgranular SCC on αβ'-brass (60/39) loop sample in 1 M NH_4OH + 0.05 M $CuSO_4$ solution at 25° C

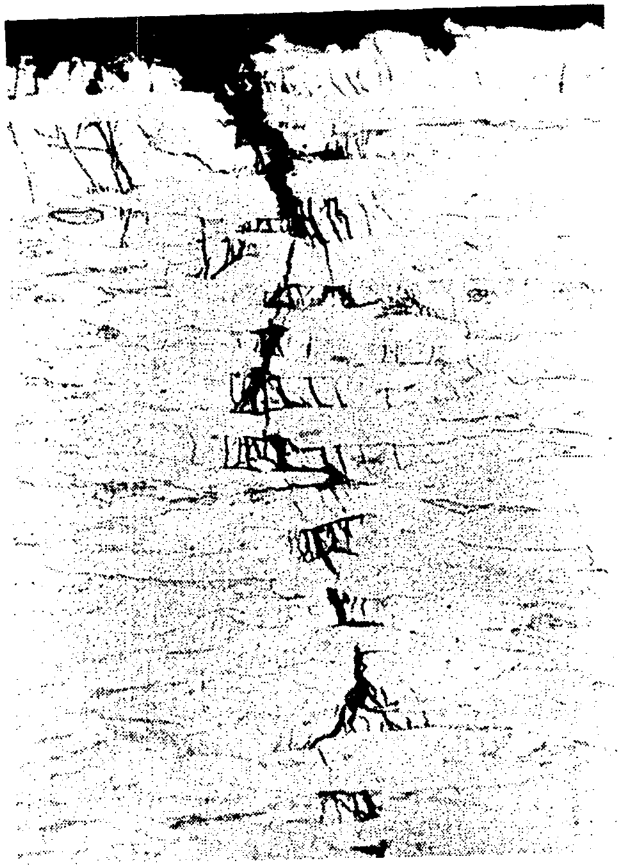

Fig. 56. Optical micrograph of transgranular SCC on αβ'-brass (60/39) loop sample in 1 M NH_4OH solution at 25° C

inner surface. It is noteworthy that many small cracks were detected on the inner surface where stresses were compressive. The cracking in 1 M $(NH_4)_2SO_4$ + 0.05 M $CuSO_4$ is also transgranular with considerable branching.

In general, the surface analysis results support the conclusions drawn from the electrochemical tests. The agreement between EDAX and Tafel plot results is clear in Table 5. When copper dissolution is the main reaction, then the crack tip is zinc-rich and vice versa. The analysis of the initiation region is also in harmony with the calculated secondary reaction, if present. So, if the secondary reaction is zinc dissolution, then the initiation region is copper-rich. The only exception to this generalization is the case of 1 M NH_4NO_3 solution, where the secondary reaction is zinc dissolution, but the initiation region analysis is Zn-rich. However, the composition changes all over the fracture surface are very small, which is in accordance with the observed small i_{cor}, and suggests that cracking in this solution does not propagate by a dissolution mechanism as will be discussed later.

In other solutions, dezincification seems to be a characteristic of the whole surface except at the cracking tip in two solutions, namely, hydroxide solutions, where the crack tip was Zn-rich, indicating more Cu-dissolution. Pinchback et al. [44] observed "preferential Zn dissolution on the SCC surface produced by the nontarnishing solution" for α-brass in Pugh's solution. This result is in accordance

Table 5. Electrochemical and EDAX results for $\alpha\beta'$-brass (60/39) in ammoniacal and ammonium salts solutions

Solution	Electrochemical predictions			$\bar{t}_f$ (hrs)	EDAX results		
	Anodic reactions						
	Main	Secondary	SCC		Crack tip	Initiation point	Surface
1 M NH_4OH + 0.05 M $CuSO_4$	Cu-dissolution	Zn-dissolution	√	5.25	Zn-rich	Cu-rich	Cu-rich
1 M NH_4OH	"	"	√	48.00	"	"	"
1 M NH_4NO_3 + 0.05 M $Cu(NO_3)_2$	Zn-dissolution	-	√	2.75	Cu-rich	Cu-rich (less)	Cu-rich
1 M NH_4NO_3	Cu-dissolution (slight)	Zn-dissolution (slight)	√	48.00	Zn-rich (slight)	Zn-rich (slight)	Zn-rich (slight)
1 M $(NH_4)_2SO_4$ + 0.05 M $CuSO_4$	Zn-dissolution	-	√	31.50	Cu-rich	Cu-rich (more)	Cu-rich

with the observed dezincification in the present work. Moreover, the same authors reported that the "composition of the SCC fracture surface is such that the Cu/Zn atomic ratio is 3 to 5, compared to a value of 2.4 : 1 for the bulk alloy composition," which represents a Zn-rich state. If this state is near the crack tip, then it is in agreement with the Zn-rich crack tip found in the present work for NH_4OH with and without $CuSO_4$ solutions. The authors also observed that the SCC surface was cleavage-like, which is hard to reconcile with the dissolution mechanism. The cleavage-like features of SCC surface in nontarnishing solutions were later reported again by Kermani and Scully [31] and also by Beavers and Pugh [57]. In the present work, no signs of true cleavage features were detected on the SCC surface in 1 M NH_4OH + 0.05 M $CuSO_4$ solution, Figure 54.

This may not be in contradiction to the earlier reported results since in all cases reported before [31,44,57] the nontarnishing solution was Pugh's solution (15 N NH_4OH + 1 g/L of dissolved Cu), while in the present work the nontarnishing solution is Mattsson's solution (1 M NH_4OH + 0.05 M $CuSO_4$). The absence of cleavage features in the present work favors the dissolution mechanism, once accepted by many authors [12,15,16,19,23,106] as the main mechanism for SCC in nontarnishing solutions. The transgranular mode of cracking is observed in all the solutions under consideration as evidenced by electron microscopy (Figures 55-56).

Brass in Nonammoniacal Aqueous Solutions

Stress corrosion cracking tests

$\alpha\beta'$-brass (60/39) loops were tested in different nonammoniacal solutions using the loop sample method. Table 6 shows the cracking time in each solution. It is noteworthy that cracking time is always shorter in solutions containing Cu^{2+} ions than in other solutions. There is also a striking analogy between nonammoniacal and ammonium salt solutions having the same anion, namely nitrate, chloride and sulfate solutions with only one exception, the sodium nitrate solution where no cracking was observed. On the other hand, cracking time observed in ammonium nitrate solution was the longest among the ammonium salt solutions.

Tensile stress specimens of α-brass (80/20) were tested in several nonammoniacal solutions at constant load. The results, Table 7, show that α-brass (80/20) is immune to SCC in all solutions tested. The results in Mattsson's solution are included for comparison.

Electrochemical tests

Corrosion potential, E_{cor}, measurements The corrosion potentials of $\alpha\beta'$-brass (60/39) in different nonammoniacal solutions are shown in Table 6. In solutions containing Cu^{2+} ions, the corrosion potential is close to or less noble than that predicted from the Nernst potential of a pure Cu electrode, indicating less corrosion of copper. The solution of NaCl + $CuCl_2$ is an exception, since the corrosion potential is more noble than the Nernst potential of pure Cu, indicating higher dissolution of copper. This is supported by the fact that dis-

Table 6. Time-to-crack and corrosion potential of αβ'-brass (60/39) in nonammoniacal solutions

Solution	t_c (hrs)	E_{cor} (mV_{SHE})
0.05 M $Cu(NO_3)_2$	2	292
1 M $NaNO_3$ + 0.05 M $Cu(NO_3)_2$	5	303
1 M $NaNO_3$	NC	226
1 M $NaClO_3$ + 0.05 M $Cu(NO_3)_2$	5	294
1 M $NaClO_3$	8	272
1 M $NaNO_2$ + 0.05 M $Cu(NO_3)_2$	5	329
1 M $NaNO_2$	16	52
1 M NaCl + 0.05 M $CuCl_2$	NC	102
1 M NaCl	NC	-98
1 M Na_2SO_4 + 0.05 M $CuSO_4$	62	231
1 M Na_2SO_4	NC	208

solution products, Cu^+ ions, are stabilized in chloride solutions. In Cu^{2+}-free solutions, the comparison between the measured corrosion potentials and the calculated Nernst potential for pure Cu indicates negligible Cu-dissolution when Cu-concentration is 10^{-4}-10^{-3} g atom/L.

The corrosion potential vs. time curves for α-brass 80/20 are shown in Figure 57. The less noble potentials are observed in complexing solu-

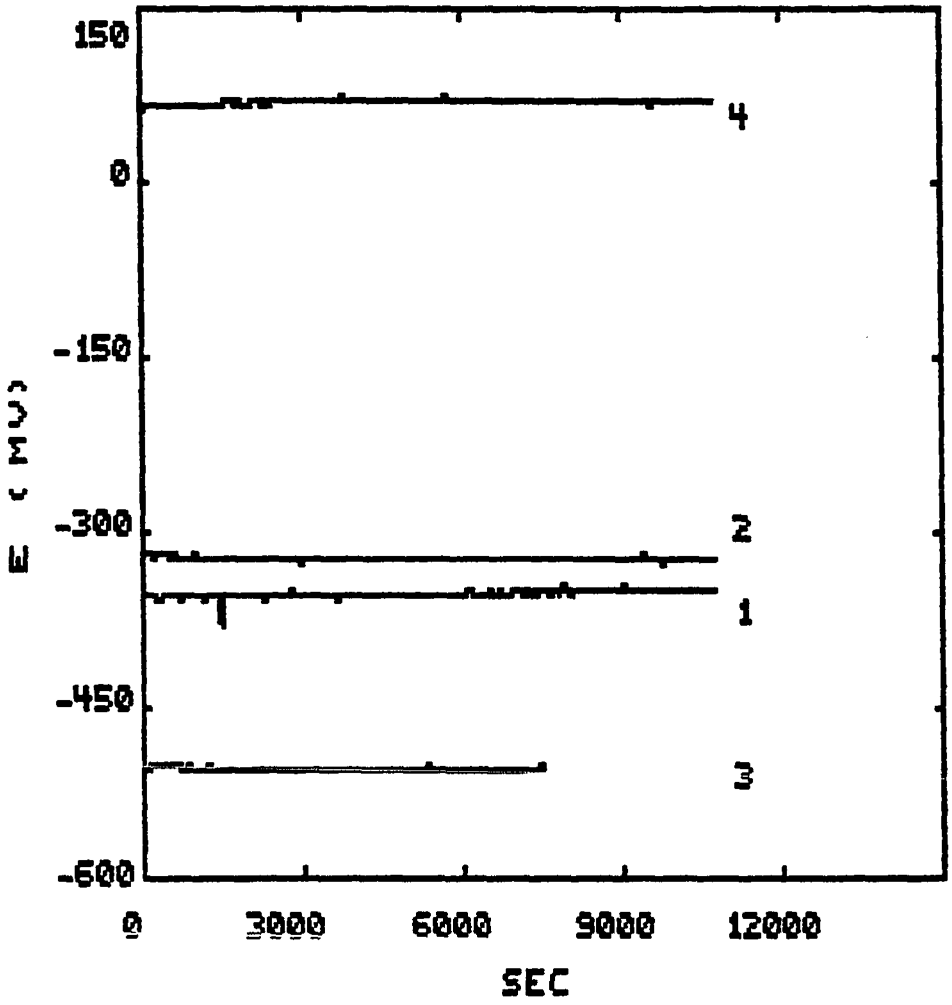

1. 1 M NH_4OH + 0.05 M $CuSO_4$
2. 1 M pyrophosphate + 0.05 M $CuSO_4$
3. 1 M ethylenediamine + 0.05 M $CuSO_4$
4. 0.1 M H_2SO_4 + 0.5 M $CuSO_4$

Figure 57. Corrosion potential vs. time for α-brass (80/20) electrode in various aqueous solutions, containing Cu^{2+} ions, at 25°C

Table 7. Time-to-failure of α-brass (80/20) in aqueous solutions

Solution	pH	t_f (hrs)
1 M NH_4OH + 0.05 M $CuSO_4$	10.9	30
1 M $K_4(P_2O_7)$ + 0.05 M $CuSO_4$	10.1	NF
0.5 M $CuSO_4$ + 0.1 M H_2SO_4	-	NF
1 M $NaNO_3$	2.5	NF
	8.4	NF
	11.4	NF
1 M $NaClO_3$	8.4	NF

tions, where in noncomplexing solutions the corrosion potential is close to that predicted from the Nernst equation for a pure copper electrode.

Tafel measurements results Tafel plots, measured at a scan rate of 0.05 mV/s, are shown in Figures 58-63, together with the Parcalc calculations, for αβ'-brass (60/39) in some of the solutions under test. The results show clearly the effect of Cu^{2+} ions on the increased corrosion rate. The most probable cathodic reactions taking place in these solutions, along with their standard reduction potentials, are:

Reaction	Potential (V_{SHE})
$O_2 + 2H_2O + 4e \rightleftarrows 4OH^-$	0.401
$NO_3^- + H_2O + 2e \rightleftarrows NO_2^- + 2OH^-$	0.010

```
=======================================
            PARCALC TAFEL MENU
=======================================
EXP. NAME:TAF CUNIT 11*        DATA:120
TECHNIQUE:TAFEL                [E VS I]
---------------------------------------

                 RESULTS

E(I=O) (MV)               48.09

CATHODIC TAFEL (MV)       173.08

ANODIC TAFEL (MV)         152.29

I-CORR (UA/CM^2)          1130.34

CORR RATE (MPY)           554.96

CHI ^2                    228.47
```

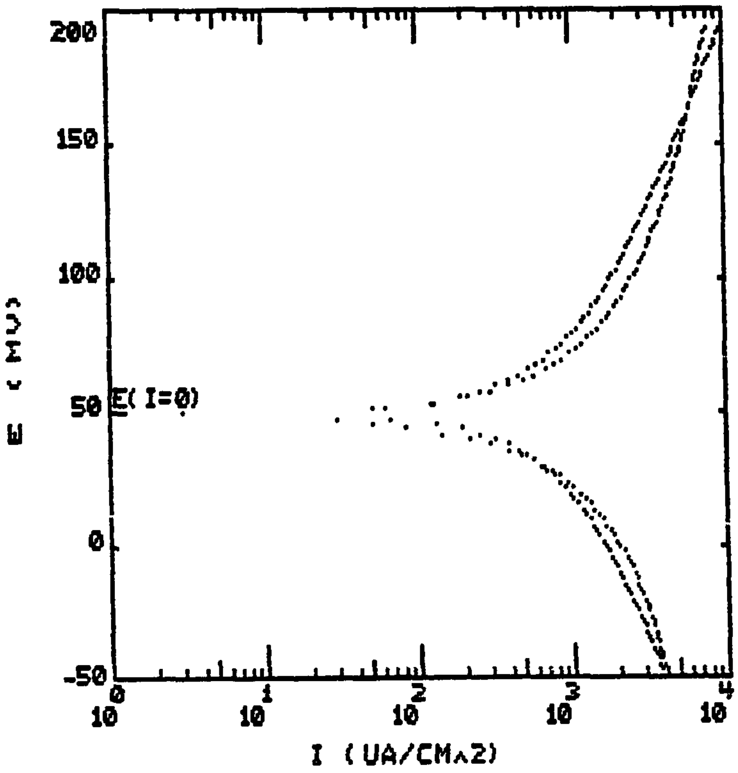

Figure 58. Tafel plot and Parcalc results for αβ'-brass (60/39) electrode in 0.05 M $Cu(NO_3)_2$ solution at 25°C

```
======================================
           PARCALC TAFEL MENU
======================================
EXP. NAME:TAFST SODNIT!*      DATA:128
TECHNIQUE:TAFEL               [E VS I]
--------------------------------------

               RESULTS

E(I=0) (MV)               103.01

CATHODIC TAFEL (MV)       54.98

ANODIC TAFEL (MV)         50.55

I-CORR (UA/CM^2)          845.545454

CORR RATE (MPY)           419.92

CHI ^2                    283.54
```

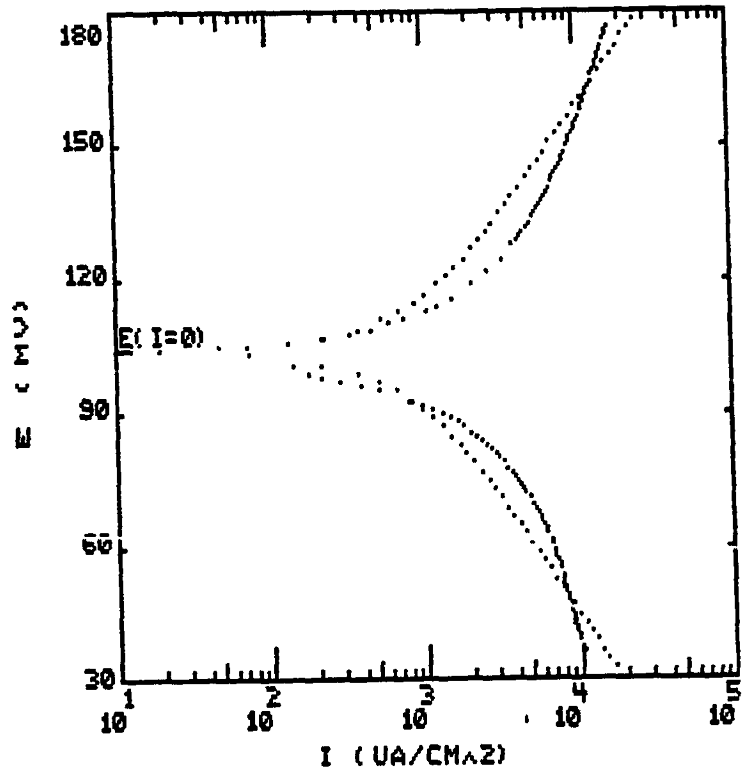

Figure 59. Tafel plot and Parcalc results for αβ'-brass (60/39) electrode in 1 M $NaNO_3$ + 0.05 M $Cu(NO_3)_2$ solution at 25°C

```
======================================
          PARCALC TAFEL MENU
======================================
EXP. NAME:TAFST SODCL+*        DATA:149
TECHNIQUE:TAFEL                [E VS I]
--------------------------------------

               RESULTS

E(I=0) (MV)              57.42

CATHODIC TAFEL (MV)      190.77

ANODIC TAFEL (MV)        55.13

I-CORR (UA/CM^2)         2778.44445

CORR RATE (MPY)          1379.86

CHI ^2                   14.49
```

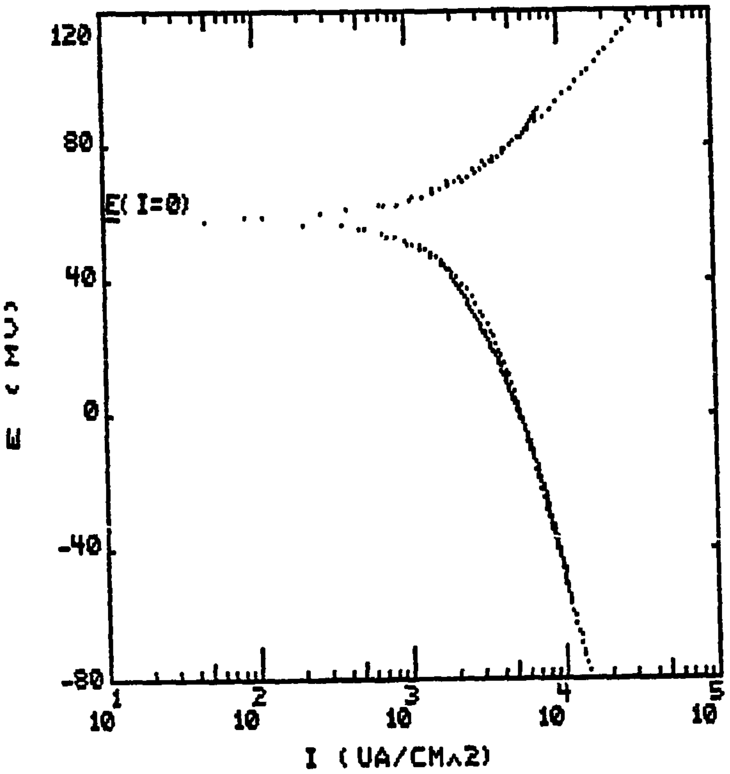

Figure 60. Tafel plot and Parcalc results for αβ'-brass (60/39) electrode in 1 M NaClO$_3$ + 0.05 M Cu(NO$_3$)$_2$ solution at 25°C

```
========================================
           PARCALC TAFEL MENU
========================================
EXP. NAME:TAFST SODNI+*        DATA:189
TECHNIQUE:TAFEL                [E VS I]
----------------------------------------

                RESULTS

E(I=0) (MV)              75.54

CATHODIC TAFEL (MV)      241.04

ANODIC TAFEL (MV)        44.06

I-CORR (UA/CM^2)         179.046512

CORR RATE (MPY)          88.92

CHI ^2                   15.8
```

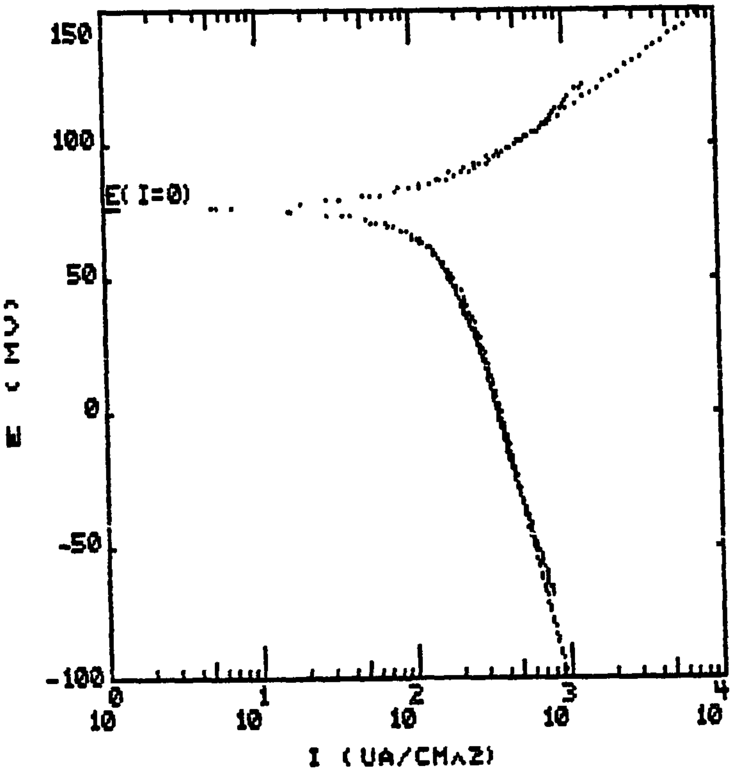

Figure 61. Tafel plot and Parcalc results for αβ'-brass (60/39) electrode in 1 M $NaNO_2$ + 0.05 M $Cu(NO_3)_2$ solution at 25°C

```
=======================================
          PARCALC TAFEL MENU
=======================================
EXP. NAME:TAFST SODC+*          DATA:202
TECHNIQUE:TAFEL                 [E VS I]
---------------------------------------

                RESULTS

E(I=0)  (MV)              -108.53

CATHODIC TAFEL  (MV)      303.38

ANODIC TAFEL  (MV)        132.92

I-CORR  (UA/CM^2)         10889.625

CORR RATE  (MPY)          5408.12

CHI ^2                    7.87
```

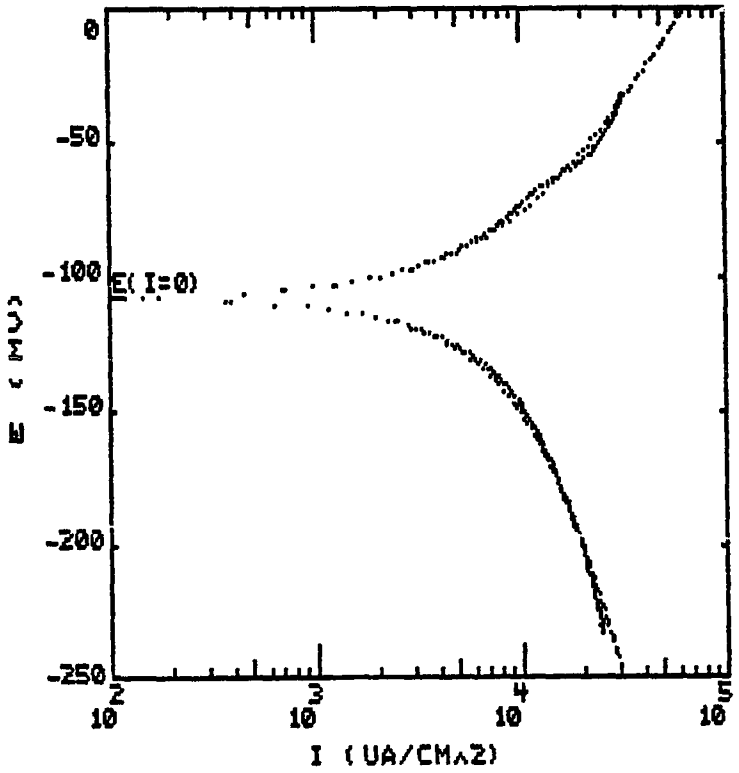

Figure 62. Tafel plot and Parcalc results for αβ'-brass (60/39) electrode in 1 M NaCl + 0.05 M $CuCl_2$ solution at 25°C

```
=======================================
          PARCALC TAFEL MENU
=======================================
EXP. NAME:TAFST SODC           DATA:192
TECHNIQUE:TAFEL                [E VS I]
---------------------------------------

               RESULTS

E(I=0) (MV)               -341.33

CATHODIC TAFEL (MV)       211.91

ANODIC TAFEL (MV)         77.49

I-CORR (UA/CM^2)          28.3529412

CORR RATE (MPY)           14.08

CHI ^2                    39.41
```

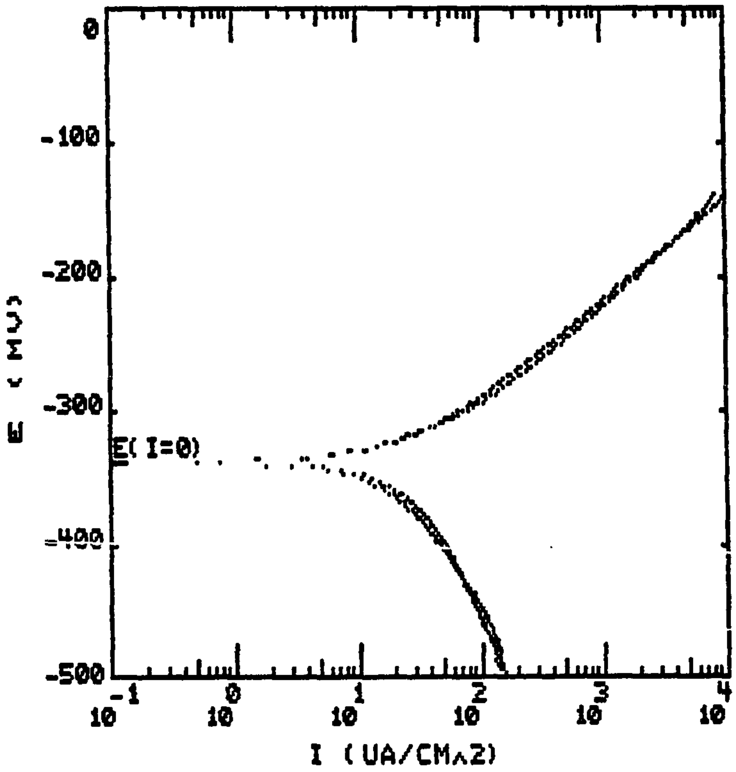

Figure 63. Tafel plot and Parcalc results for αβ'-brass (60/39) electrode in 1 M NaCl solution at 25°C

Reaction	Potential (V_{SHE})
$Cu^{2+} + 2e \rightleftharpoons Cu$	0.340
$CuCl_2 + e \rightleftharpoons CuCl_2^-$	0.300

On the other hand, the most probable anodic reactions are:

$Zn^{2+} + 2e \rightleftharpoons Zn$	-0.76
$Cu^{2+} + 2e \rightleftharpoons Cu$	0.34
$CuCl_2^- + e \rightleftharpoons Cu + 2Cl^-$	-0.026

To predict the electrochemical reactions in each solution, the above potentials are adjusted according to the solution pH and dissolved ions. Table 8 summarizes the proposed anodic and cathodic reactions in each solution, along with the corresponding values of the corrosion potential and corrosion current. The Tafel plots of pure Cu and pure Zn in two noncomplexing solutions (Figures 64-67) support the predicted selective dissolution of Zn in these solutions.

The Tafel plot measurements and Parcalc results, for α-brass (80/20) in some of the solutions, are shown in Figures 68-71. The most probable anodic and cathodic reactions in these solutions (according to potential values) are summarized in Table 9. The small corrosion current in $NaNO_3$ solution, and the subsequent large increase upon Cu^{2+} ion addition, are noteworthy. No SCC was observed in either solution. The very low corrosion rate in pyrophosphate + $CuSO_4$ is attributed to the formation of

```
=======================================
            PARCALC TAFEL MENU
=======================================
EXP. NAME:TAFCU NACLO*         DATA:98
TECHNIQUE:TAFEL                [E VS I]
---------------------------------------

                RESULTS

E(I=0) (MV)               122.25

CATHODIC TAFEL (MV)       286.79

ANODIC TAFEL (MV)         149.05

I-CORR (UA/CM^2)          7026.71739

CORR RATE (MPY)           3238.96

CHI ^2                    236.7
```

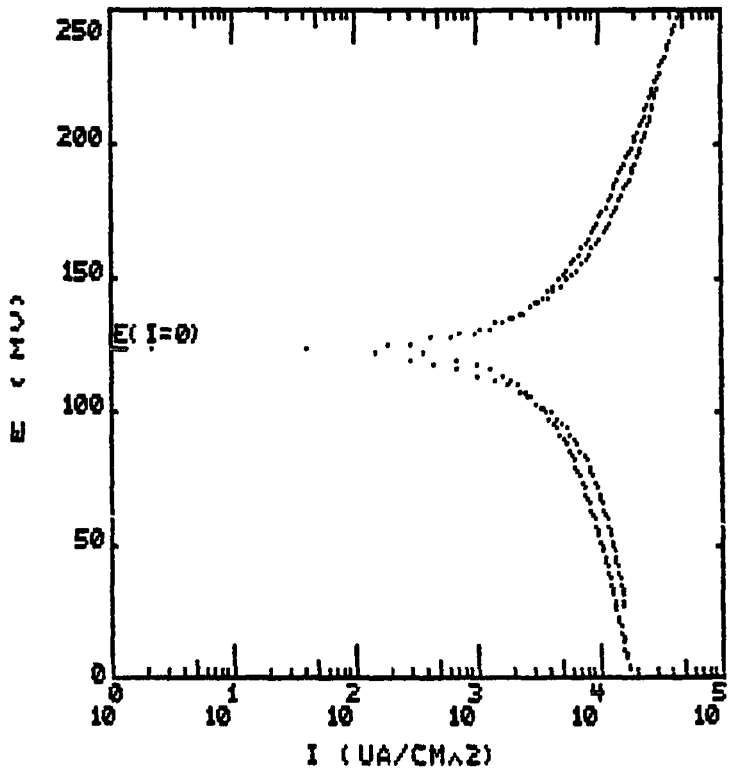

Figure 64. Tafel plot and Parcalc results for pure copper electrode in 1 M $NaNO_3$ + 0.05 M $Cu(NO_3)_2$ solution at 25°C

```
=====================================
           PARCALC TAFEL MENU
=====================================
EXP. NAME:TAFZN NACLO*         DATA:231
TECHNIQUE:TAFEL                [E VS I]
-------------------------------------

                RESULTS

E(I=0)  (MV)              -534.65

CATHODIC TAFEL  (MV)      74560.02

ANODIC TAFEL  (MV)        130.02

I-CORR  (UA/CM^2)         14302.0392

CORR RATE  (MPY)          8512.52

CHI ^2                    66.02
```

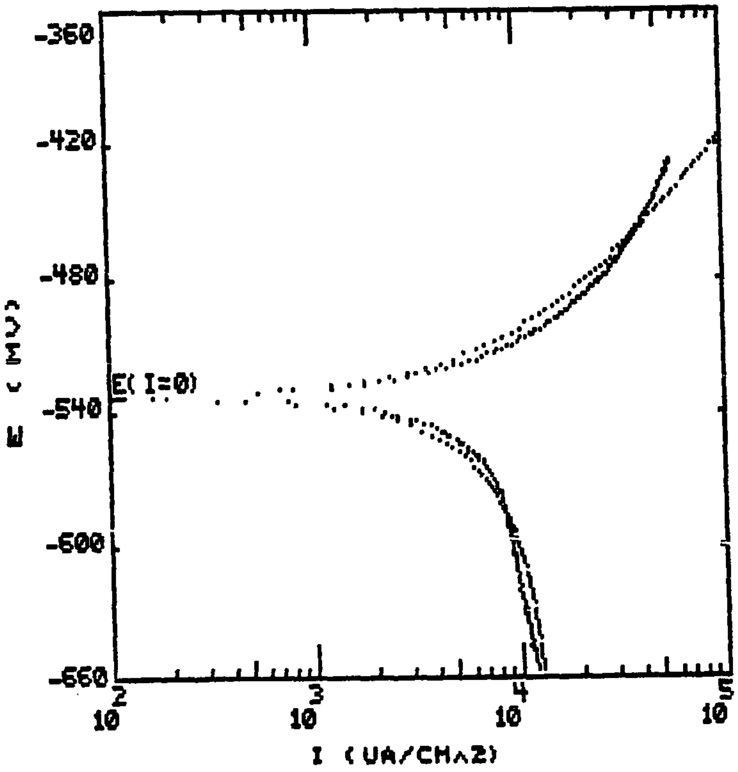

Figure 65. Tafel plot and Parcalc results for pure zinc electrode in 1 M $NaNO_3$ + 0.05 M $Cu(NO_3)_2$ solution at 25°C

```
======================================
           PARCALC TAFEL MENU
======================================
EXP. NAME:TAFCU SODCL*        DATA:123
TECHNIQUE:TAFEL               [E VS I]
--------------------------------------

                RESULTS

E(I=0) (MV)              154.31

CATHODIC TAFEL (MV)      225.76

ANODIC TAFEL (MV)        120.17

I-CORR (UA/CM^2)         4135.12727

CORR RATE (MPY)          1906.08

CHI ^2                   8.76
```

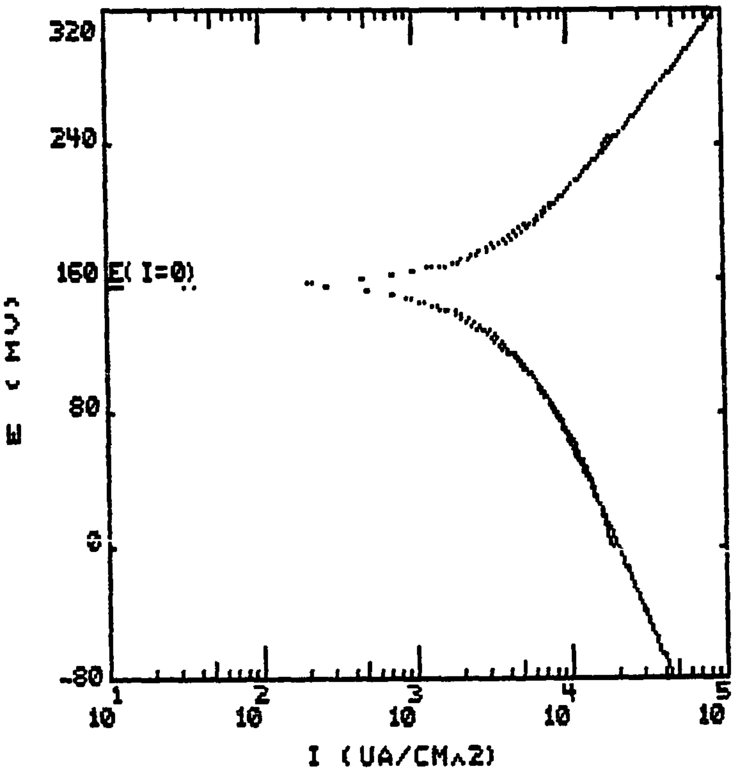

Figure 66. Tafel plot and Parcalc results for pure copper electrode in 1 M $NaClO_3$ + 0.05 M $Cu(NO_3)_2$ solution at 25°C

```
========================================
           PARCALC TAFEL MENU
========================================
EXP. NAME:TAFZN SODCL*           DATA:157
TECHNIQUE:TAFEL                  [E VS I]
----------------------------------------

                RESULTS

E(I=O) (MV)                  -619.32

CATHODIC TAFEL (MV)          388.05

ANODIC TAFEL (MV)            137.16

I-CORR (UA/CM^2)             14766.9821

CORR RATE (MPY)              8789.25

CHI ^2                       20.1
```

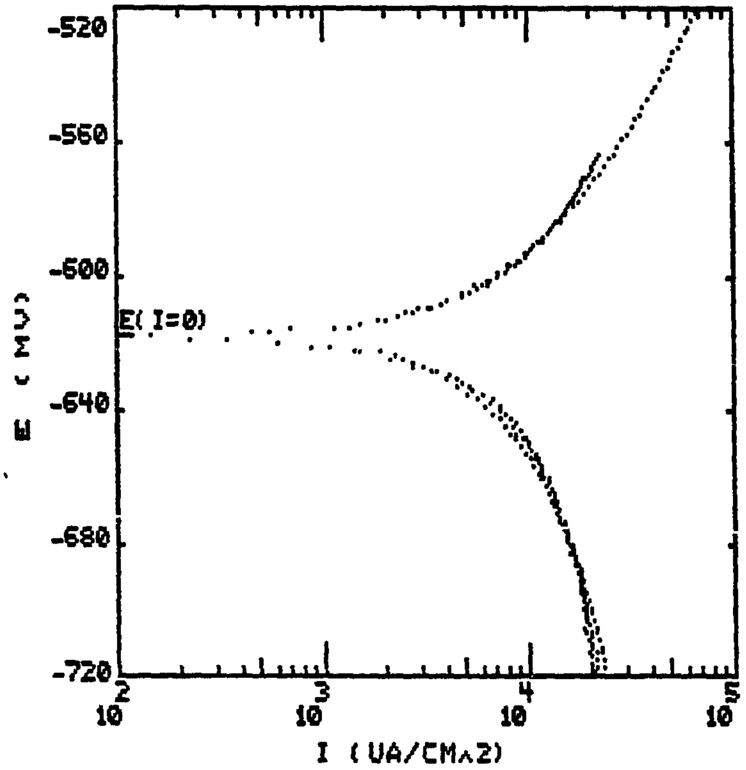

Figure 67. Tafel plot and Parcalc results for pure zinc electrode in 1 M $NaClO_3$ + 0.05 M $Cu(NO_3)_2$ solution at 25°C

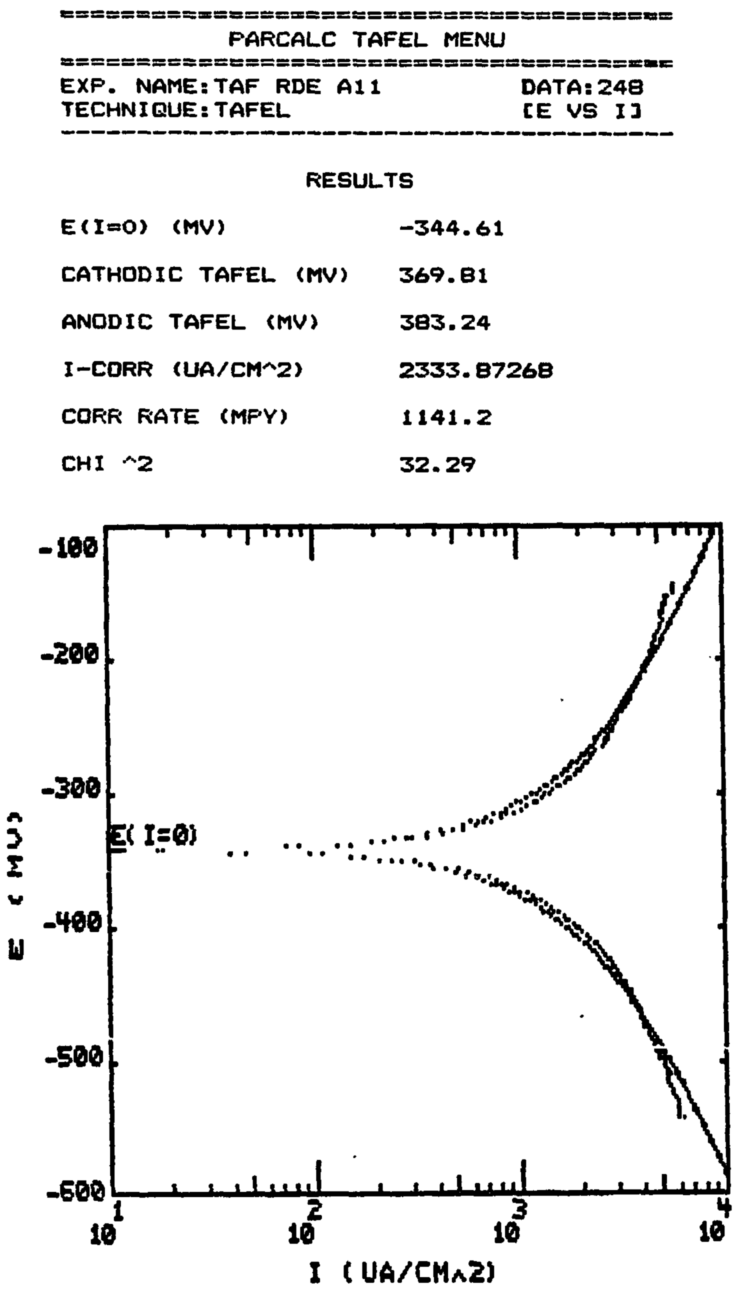

```
=====================================
           PARCALC TAFEL MENU
=====================================
EXP. NAME:TAF RDE A11          DATA:248
TECHNIQUE:TAFEL                [E VS I]
-------------------------------------

                RESULTS

E(I=0) (MV)               -344.61

CATHODIC TAFEL (MV)       369.81

ANODIC TAFEL (MV)         383.24

I-CORR (UA/CM^2)          2333.87268

CORR RATE (MPY)           1141.2

CHI ^2                    32.29
```

Figure 68. Tafel plot and Parcalc results for α-brass (80/20) rotating disc electrode at 100 rpm in 1 M NH_4OH + 0.05 M $CuSO_4$ solution at 25°C

```
=======================================
          PARCALC TAFEL MENU
=======================================
EXP. NAME:TAF RDE P11*         DATA:122
TECHNIQUE:TAFEL                [E VS I]
---------------------------------------

               RESULTS

E(I=0) (MV)                -320

CATHODIC TAFEL (MV)        763.19

ANODIC TAFEL (MV)          56.6

I-CORR (UA/CM^2)           57.6392573

CORR RATE (MPY)            28.18

CHI ^2                     57.33
```

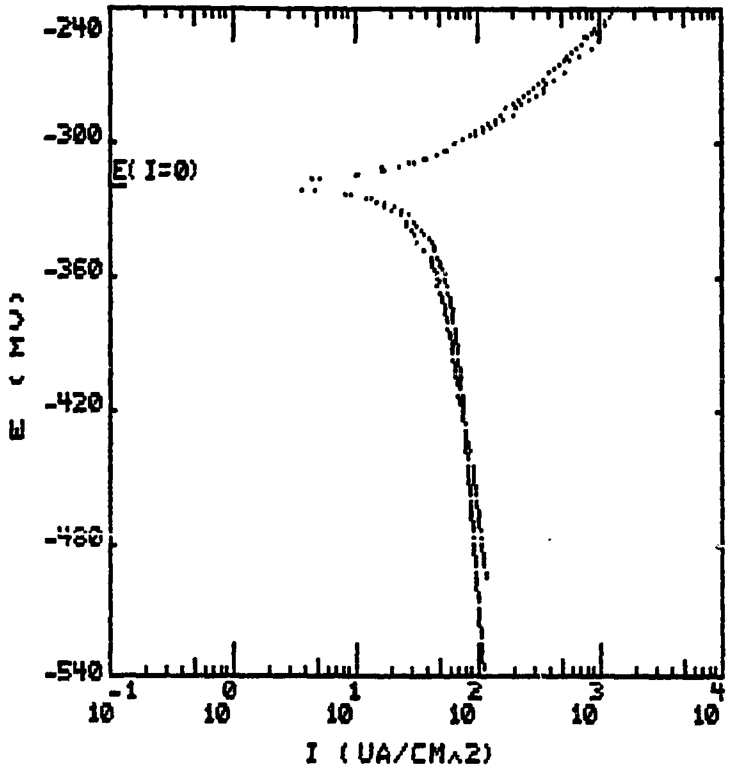

Figure 69. Tafel plot and Parcalc results for α-brass (80/20) rotating disc electrode at 100 rpm in 1 M pyrophosphate + 0.05 M $CuSO_4$ solution at 25°C

```
=====================================
           PARCALC TAFEL MENU
=====================================
EXP. NAME:TAF RDE 18*          DATA:95
TECHNIQUE:TAFEL                [E VS I]
-------------------------------------

              RESULTS

E(I=0) (MV)              -119.14

CATHODIC TAFEL (MV)      197.87

ANODIC TAFEL (MV)        314.81

I-CORR (UA/CM^2)         24.2175066

CORR RATE (MPY)          11.84

CHI ^2                   26.63
```

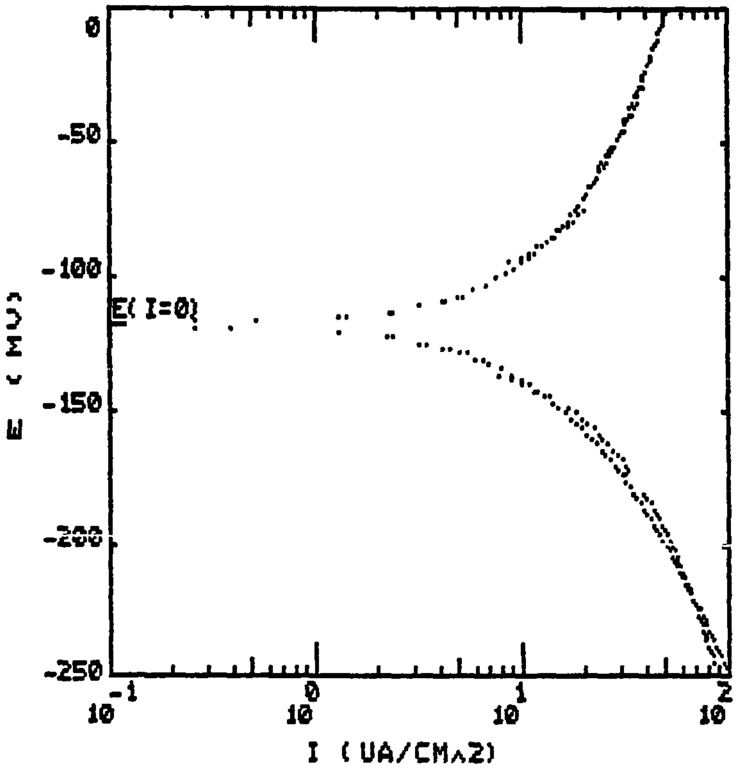

Figure 70. Tafel plot and Parcalc results for α-brass (80/20) rotating disc electrode at 100 rpm in 1 M $NaNO_3$ solution at 25°C

```
=====================================
          PARCALC TAFEL MENU
=====================================
EXP. NAME:TAF RDE 12 CU*      DATA:191
TECHNIQUE:TAFEL               [E VS I]
-------------------------------------

               RESULTS

E(I=O) (MV)               47.79

CATHODIC TAFEL (MV)       371.89

ANODIC TAFEL (MV)         199.13

I-CORR (UA/CM^2)          9562.46684

CORR RATE (MPY)           4675.78

CHI ^2                    18.3
```

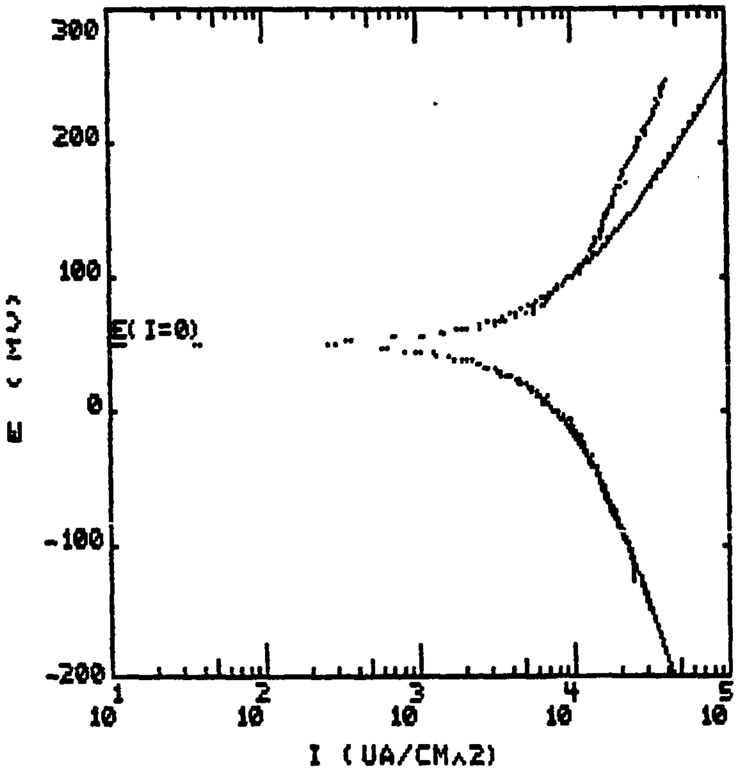

Figure 71. Tafel plot and Parcalc results for α-brass (80/20) rotating disc electrode at 100 rpm in 1 M $NaNO_3$ + 0.05 M $Cu(NO_3)_2$ solution at 25°C

Table 8. Electrochemical reactions of $\alpha\beta'$-brass (60/39) in nonammoniacal solutions at 25°C

Solution	E_{cor} (mV_{SHE})	i_{cor} ($\mu A/cm^2$)
1 M $NaNO_3$ + 0.05 M $Cu(NO_3)_2$	345.01	845.00
1 M $NaClO_3$ + 0.05 M $Cu(NO_3)_2$	299.42	2778.44
1 M $NaNO_2$ + 0.05 M $Cu(NO_3)_2$	317.54	179.05
1 M NaCl	-99.33	28.35
1 M NaCl + 0.05 M $CuCl_2$	133.47	10889.63

[a] Average time-to-crack.

[b] No cracking.

$\bar{t}_c$ [a] (hrs)	Anodic reaction (species to be oxidized)	Tafel slope (mV)	Cathodic reaction (species to be reduced)	Tafel slope (mV)
5	Zn	50.5	NO_3^-	54.9
5	Zn	55.1	Cu^{2+}	190.7
5	Zn	44.0	O_2	241.0
NC[b]	Zn	77.5	O_2	211.91
NC	Cu Zn	132.9	$CuCl_2$	303.3

$[Cu(P_2O_7)]^{-2}$ and $[Cu(P_2O_7)_2]^{-6}$ complexes which do not provide the necessary reducible cationic species as in the case of ammonia solution, where moderate corrosion current is observed and consequently SCC. Results in Mattsson's solution are included for comparison.

Table 9. Electrochemical reactions of α-brass (80/20) in nonammoniacal solutions at 25°C

Solution	E_{cor} (mV_{SHE})	i_{cor} ($\mu A/cm^2$)	Anodic reaction (species to be oxidized)	Cathodic reaction (species to be reduced)
1 M NH_4OH + 0.05 M $CuSO_4$	-102.6	2333.8	Cu Zn	$[Cu(NH_3)_4]^{2+}$
1 M pyrophosphate + 0.05 M $CuSO_4$	-78	57.6	Zn	O_2
1 M $NaNO_3$	122.8	24.2	Zn	O_2
1 M $NaNO_3$ + 0.05 M $Cu(NO_3)_2$	289.7	9562.4	Zn	Cu^{2+}

Cyclic polarization measurements The cyclic polarization curves of αβ'-brass (60/39) are shown in Figures 72-79. The same features found before in ammoniacal and ammonium salt solutions are noticed in the present solutions. In $NaNO_3$ solution, where SCC is predicted according

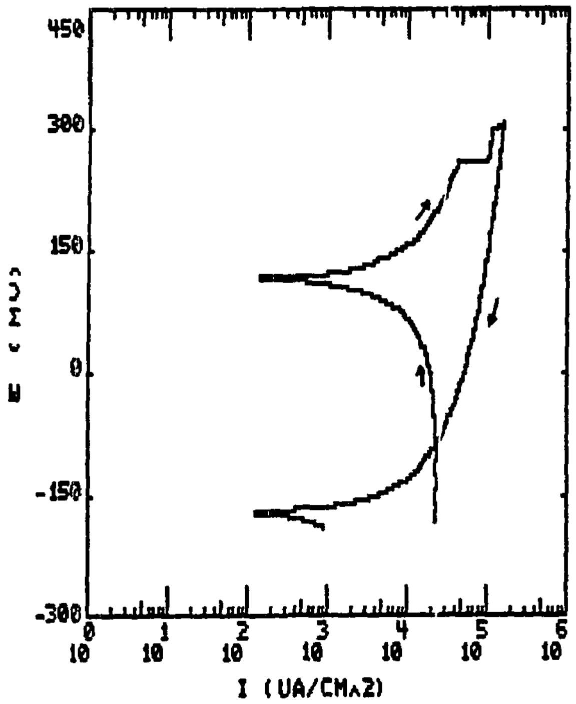

Figure 72. Cyclic polarization curve for αβ'-brass (60/39) electrode in 1 M $NaNO_3$ + 0.05 M $Cu(NO_3)_2$ solution at 25°C

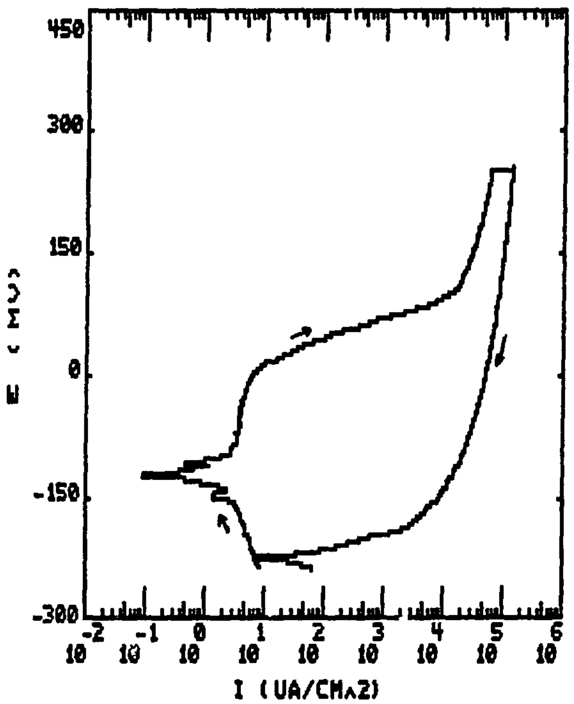

Figure 73. Cyclic polarization curve for αβ'-brass (60/39) electrode in 1 M $NaNO_3$ solution at 25°C

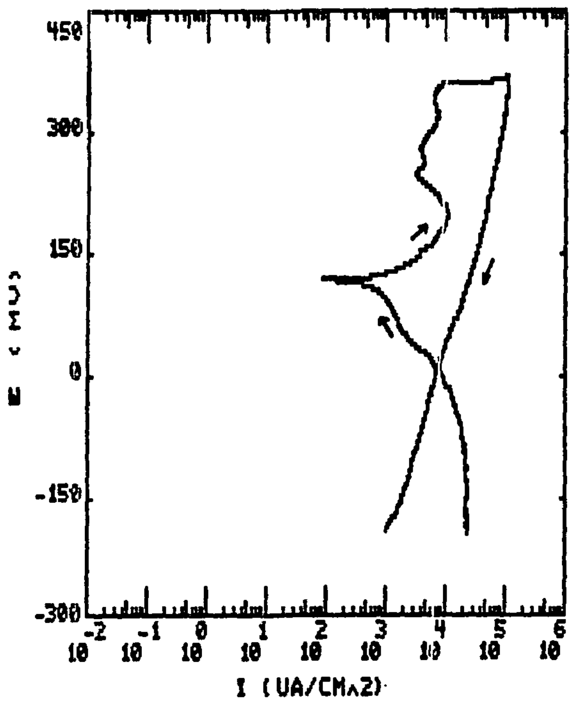

Figure 74. Cyclic polarization curve for αβ'-brass (60/39) electrode in 1 M $NaClO_3$ + 0.05 M $Cu(NO_3)_2$ solution at 25°C

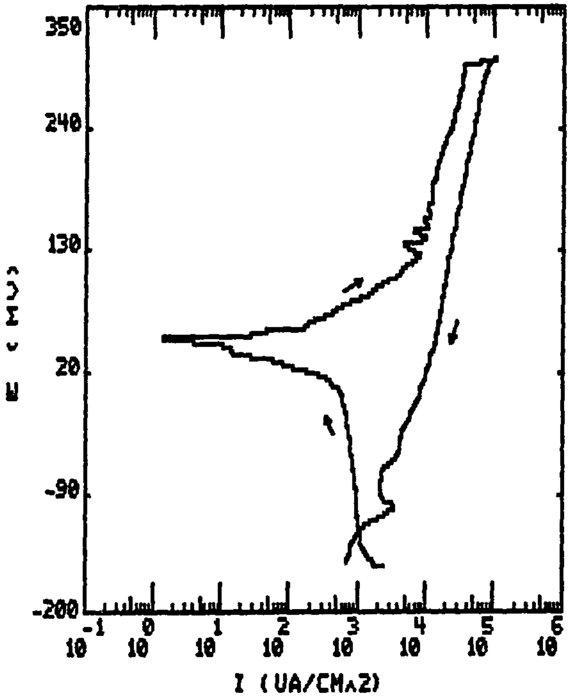

Figure 75. Cyclic polarization curve for αβ'-brass (60/39) electrode in 1 M $NaNO_2$ + 0.05 M $Cu(NO_3)_2$ solution at 25°C

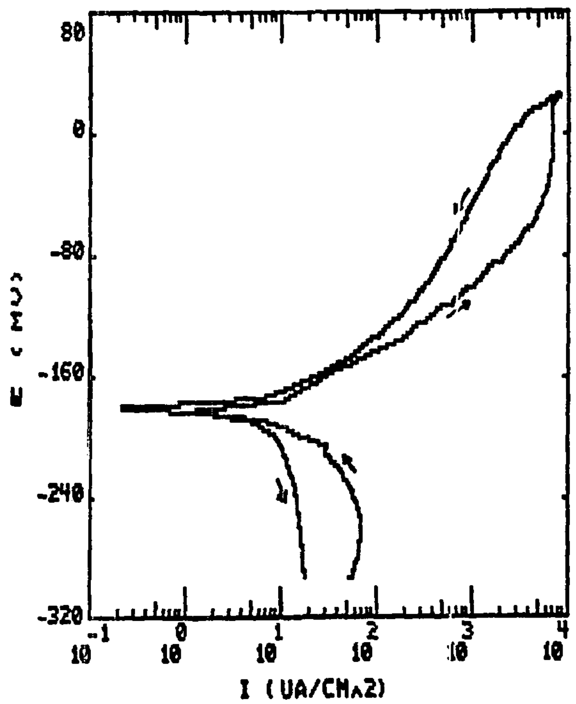

Figure 76. Cyclic polarization curve for αβ'-brass (60/39) electrode in 1 M $NaNO_3$ + 0.05 M $Cu(NO_3)_2$ solution at 25°C

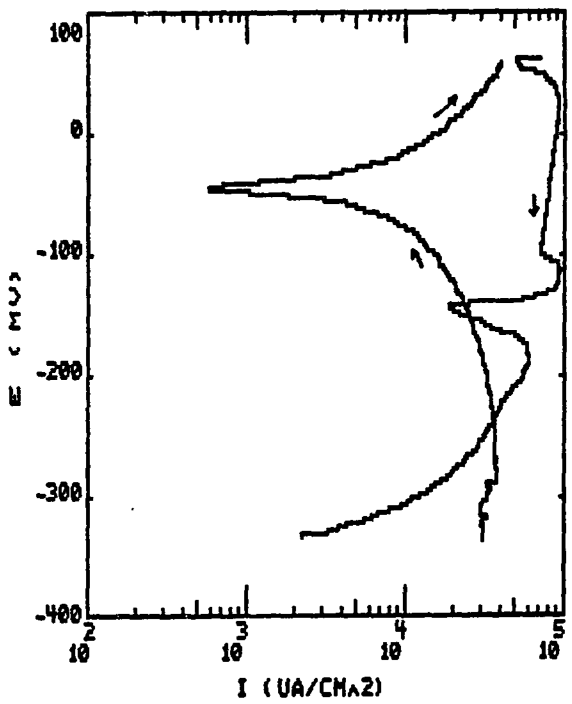

Figure 77. Cyclic polarization curve for αβ'-brass (60/39) electrode in 1 M NaCl + 0.05 M $CuCl_2$ solution at 25°C

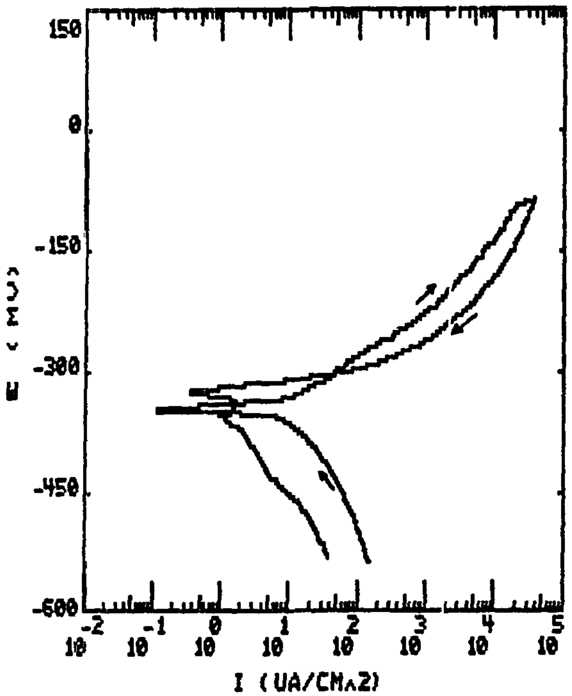

Figure 78. Cyclic polarization curve for $\alpha\beta'$-brass (60/39) electrode in 1 M NaCl solution at 25°C

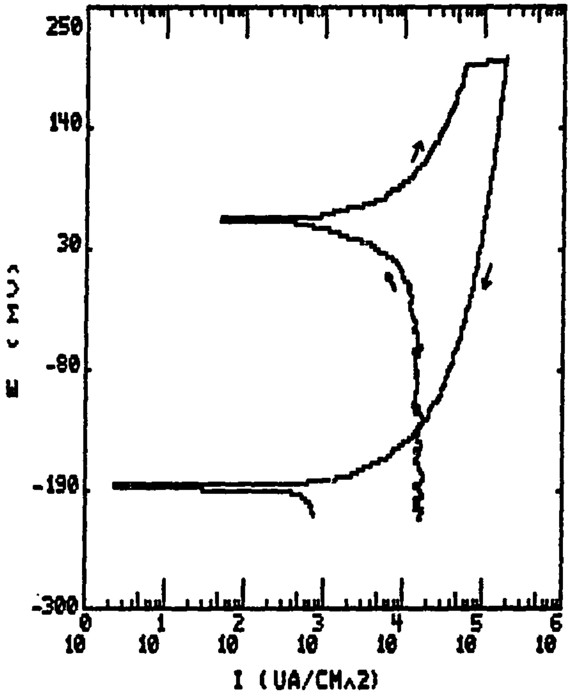

Figure 79. Cyclic polarization curve for $\alpha\beta'$-brass (60/39) electrode in 1 M Na_2SO_4 + 0.05 M $CuSO_4$ solution at 25°C

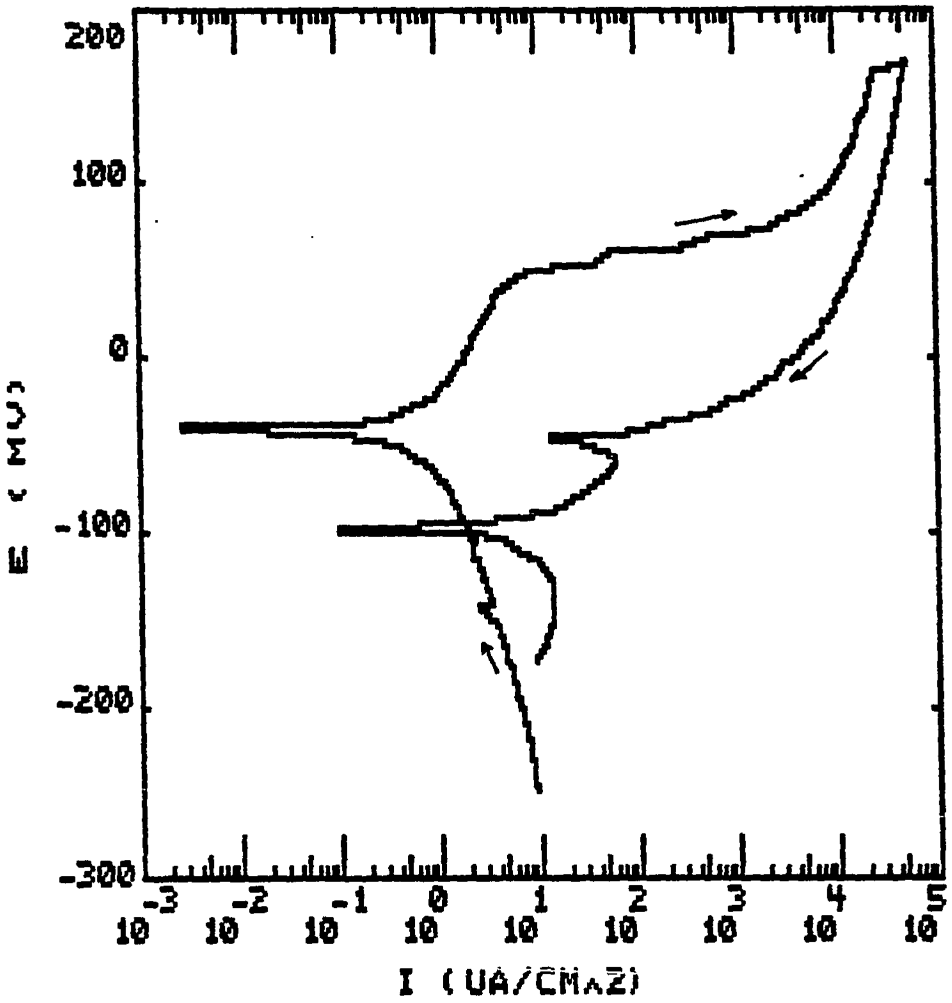

Figure 80. Cyclic polarization curve for α-brass (80/20) electrode in 1 M $NaNO_3$ solution at 25°C

to the cyclic polarization curves, the corrosion current is very small. So, the dissolution mechanism, and accordingly SCC susceptibility, are excluded. On the other hand, the lack of the required features in $NaNO_2$ solution, where SCC occurred, supports the adsorption model mechanism. In NaCl + 0.05 M $CuCl_2$ solution, general corrosion takes place due to the high corrosion rate.

The cyclic polarization curves for α-brass (80/20) in Mattsson's ammoniacal and sodium nitrate solutions are shown in Figures 39 and 80. The same features mentioned before can easily be noticed in the first curve, where cracking was also observed. The absence of these features in the case of sodium nitrate is supported by the fact that no SCC was observed in this solution.

Surface analysis tests

A sample of the optical microscopy results of αβ'-brass (60/39) in different solutions is shown in Figures 81,82.

The results show the following features:

1. In solutions containing Cu^{2+} ions, wide branching cracks are observed, indicating more dissolution in these solutions (Figure 81). It should be noted that the lowest time-to-crack values are observed in these solutions.
2. In Cu^{2+}-free solutions, narrow and nonbranching cracks are observed (Figure 82).

Generally, the transgranular cracking mode is observed in all nonammoniacal solutions under test, which is in accordance with previously reported results, and also with the fact that the solutions are nontarnishing.

The cracking of brass in nitrite, nitrate, chlorate, and sulfate

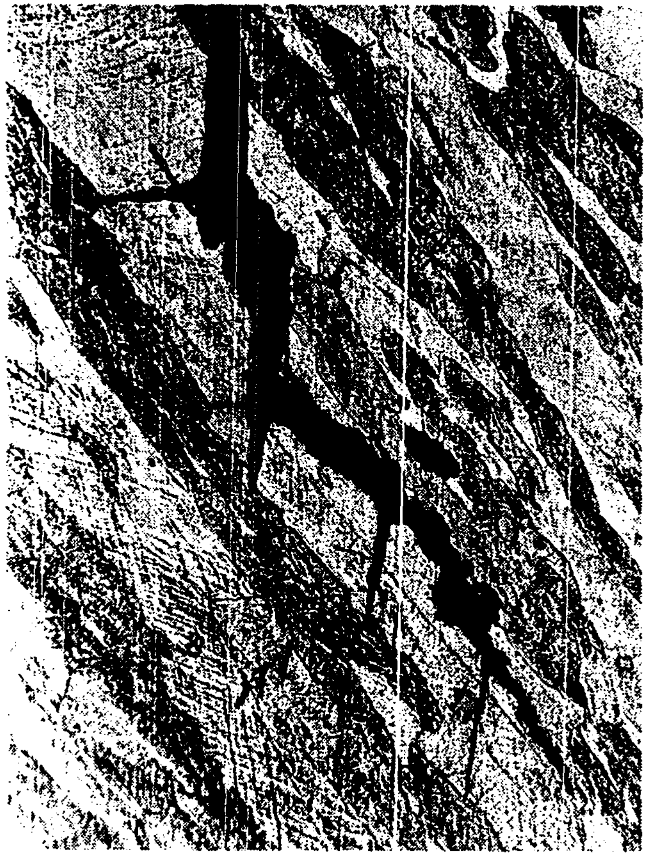

Fig. 81. Optical micrograph of transgranular SCC on $\alpha\beta'$-brass (60/39) loop sample in 1 M $NaClO_3$ + 0.05 M $CuSO_4$ solution at 25° C

Fig. 82. Optical micrograph of transgranular SCC on $\alpha\beta'$-brass (60/39) loop sample in 1 M $NaClO_3$ solution at 25° C

solutions was reported before [60,61,66,67]; however, at least one of the experimental conditions (open circuit potential and static load technique) was always missing. Under these conditions, α-brass (80/20) proved again to be more resistant to SCC than αβ'-brass (60/39). The immunity of α-brass in nonammoniacal solutions tested can be attributed to either general corrosion or very little dissolution rates.

In αβ'-brass (60/39), the similarity between the results obtained in ammoniacal and ammonium salt solutions and those obtained in nonammoniacal solutions is striking. The SCC results (in the sense of occurrence or nonoccurrence) are the same in all tested ammonium salts and nonammoniacal solutions having the same anion except the nitrate anion, with higher time-to-crack in the case of nonammoniacal solutions. The cracking in ammonium nitrate, and not in sodium nitrate solution, and the shorter time-to-crack in ammonium salt solutions than in nonammoniacal solutions, emphasize the fact that NH_4^+ ion has a stimulating effect in SCC. On the other hand, the cracking in cupric nitrate solution supports the importance of Cu^{2+} ions which furnish an efficient cathodic reaction and consequently SCC in most of Cu^{2+}-containing solutions. Consequently, the previously reported cracking in nitrate and sulfate solutions was not proved in the present work, and electrochemical results show very little dissolution in these solutions. In chloride solutions, no cracking was observed due to the same reasons in ammonium chloride solutions, as supported by electrochemical results. The results support a SCC dissolution mechanism (except in cases where corrosion rate is very low which will be discussed later), and preferential zinc dissolution, which is to be expected in solutions not leading to Cu^{+}- or Cu^{2+}-complexes. Moreover, SCC can be predicted using the cyclic polarization curves as was discussed before for the case of ammoniacal and ammonium salt solutions.

Pure Copper in Aqueous Solutions

Stress corrosion cracking tests

Pure copper (99.9%) loop specimens were tested for cracking in two groups of solutions. The first group includes solutions which were reported in literature to cause SCC of pure copper. Table 10 summarizes the results of the present work along with the previously reported results.

Table 10. SCC results of pure copper in various aqueous solutions at 25°C (first group)

Solution	Present study	Previous work	
15 N NH_4OH + 2.5 g/L of Cu	NC[a]	F[b]	[73]
0.4 N $CuSO_4$	"	NF[c]	[76]
1 M $NaNO_2$	"	F	[77]
0.03 M NH_4OH	"	F	[78]
0.05 M NH_4OH	"	F	[78]
0.07 M NH_4OH	"	F	[78]

[a] No cracking.

[b] Failure.

[c] No failure.

It is noteworthy that an $\alpha\beta'$-brass (60/39) sample, tested in the first solution, suffered cracking after only two hours.

The second group includes some of the solutions tested before in the case of $\alpha\beta'$-brass (60/39). Although brass was found to crack in most of these solutions, pure copper showed no sign of cracking after more than two weeks.

Results for both pure copper and $\alpha\beta'$-brass (60/39) are summarized in Table 11. The present study shows that pure copper is not susceptible to SCC in different tarnishing and nontarnishing solutions. The results support the previously reported conclusions that pure metals are not susceptible to SCC. The failure reported before may be due to general corrosion [73,78], or the use of dynamic load technique [77].

Electrochemical tests

Corrosion potential measurements In noncomplexing solutions, the corrosion potential is close to that predicted from the Nernst equation, indicating that little copper dissolution occurs in these solutions. On the other hand, in complexing solutions, the corrosion potential is more noble than the predicted pure copper potential according to the potential/pH diagrams, indicating more dissolution of copper in these solutions. The corrosion potentials of pure copper, along with $\alpha\beta'$-brass (60/39) are shown in Table 11. It is noteworthy that the corrosion potential of brass is less noble but close to that of pure copper, which is in accordance with the fact that the behavior, of brass alloys with copper content higher than 40%, approaches that of pure

Table 11. SCC results and corrosion potentials of copper and αβ'-brass (60/39) in various aqueous solutions at 25°C (second group)

Solution	Scc results		E_{cor} (mV_{SHE})	
	Pure Cu	Brass	Pure Cu	Brass
1 M NH_4OH + 0.05 M $CuSO_4$	NC[a]	C[b]	-83	-129
1 M NH_4NO_3 + 0.05 M $Cu(NO_3)_2$	NC	C	299	292
1 M $(NH_4)_2SO_4$ + 0.05 M $CuSO_4$	NC	C	267	257
1 M $(NH_4)_2CO_3$ + 0.05 M $CuSO_4$	NC	NC	26	-38
1 M NH_4Cl + 0.05 M $CuCl_2$	NC	NC	127	105
1 M NH_4OH	NC	C	-202	-233
1 M $NaNO_3$ + 0.05 M $Cu(NO_3)_2$	NC	C	302	303
1 M $NaNO_2$ + 0.05 M $Cu(NO_3)_2$	NC	C	-	329
1 M $NaClO_3$ + 0.05 M $Cu(NO_3)_2$	NC	C	322	294
1 M NaCl + 0.05 M 0.05 M $CuCl_2$	NC	NC	-	102

[a] No cracking.

[b] Cracking.

copper more rapidly than it approaches that of pure zinc [125].

Tafel plots results   Tafel plots of pure Cu, in some of the solutions investigated, are shown in Figures 11, 16, 64, 66, and 83. In solutions where copper potential is close to Nernst potential, i_{cor}

```
======================================
          PARCALC TAFEL MENU
======================================
EXP. NAME:TAFCU AMCAR 2*       DATA:90
TECHNIQUE:TAFEL                [E VS I]
--------------------------------------

               RESULTS

E(I=O)  (MV)                -185.18

CATHODIC TAFEL  (MV)        167.24

ANODIC TAFEL  (MV)          93.14

I-CORR  (UA/CM^2)           5397.97917

CORR RATE  (MPY)            2488.19

CHI ^2                      24.5
```

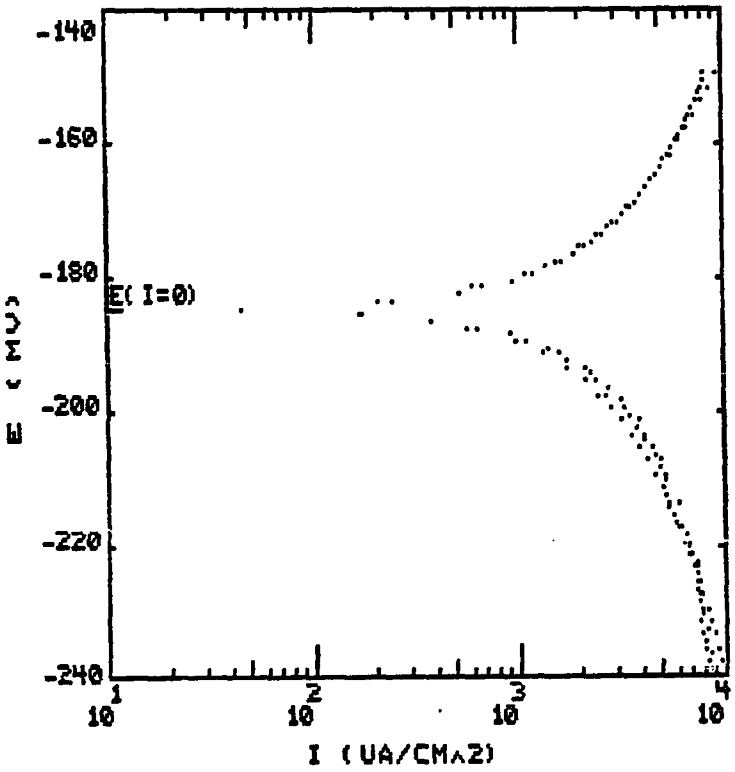

Figure 83. Tafel plot and Parcalc results for pure copper electrode in 1 M $(NH_4)_2CO_3$ + 0.05 M $CuSO_4$ solution at 25°C

is equal to the exchange current of the reaction $Cu \rightarrow Cu^{2+} + 2e$. The results show more dissolution of copper (than zinc) in complexing solutions, which is in favor of selective dissolution discussed before.

Cyclic polarization results The cyclic polarization curves for pure copper in some of the solutions are shown in Figures 84-87. The curves have the same features required before to predict SCC, in spite of the absence of cracking in all of the solutions. This indicates that cyclic polarization curves (in the present form) can't be used to predict SCC of pure copper as it was used for brass.

In conclusion, it is believed that the previously reported SCC of pure Cu [73,77-78] was probably due to general corrosion [73,78] as discussed by Uhlig and Duqette [75], commercial impurities [78] or application of dynamic load techniques [77].

Stress Corrosion Cracking Mechanisms

The present results of SCC, electrochemical, and surface analysis tests indicate the presence of more than one mechanism for transgranular SCC of brass in nontarnishing solutions.

Dissolution mechanism

This mechanism applies in aqueous solutions where the corrosion rate has an intermediate value ($0.1 < i_{cor} < 5$ mA/cm^2). Preferential dissolution of zinc takes place in noncomplexing solutions, while preferential copper dissolution occurs in complexing solutions, as evidenced by electrochemical and surface analysis tests. The shape of cyclic polarization curves supports the assumption that pit formation is the

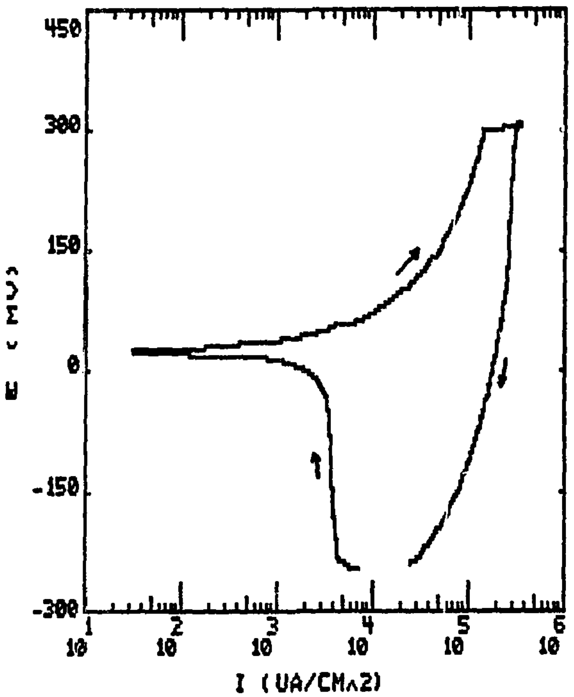

Figure 84. Cyclic polarization curve for pure copper electrode in 1 M $(NH_4)_2SO_4$ + 0.05 M $CuSO_4$ solution at 25°C

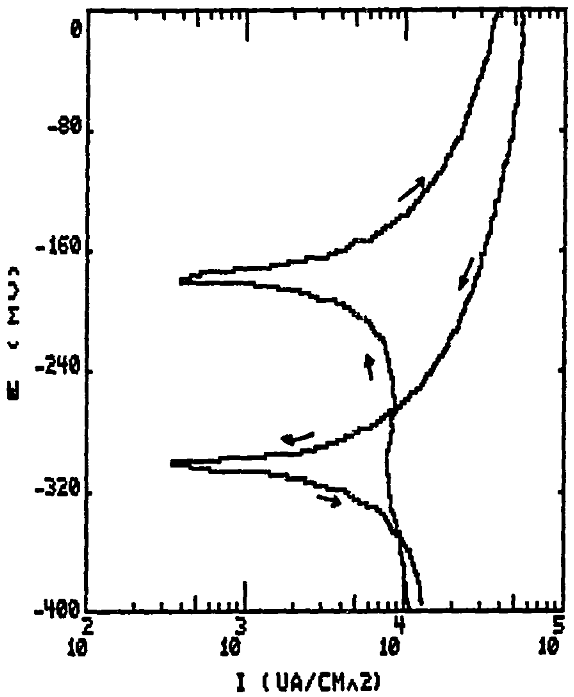

Figure 85. Cyclic polarization curve for pure copper electrode in 1 M $(NH_4)_2CO_3$ + 0.05 M $CuSO_4$ solution at 25°C

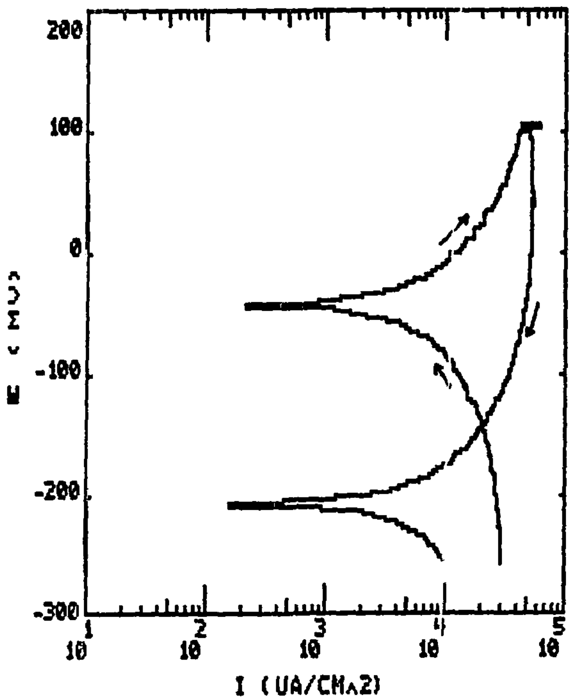

Figure 86. Cyclic polarization curve for pure copper electrode in 1 M NH_4Cl + 0.05 M $CuCl_2$ solution at 25°C

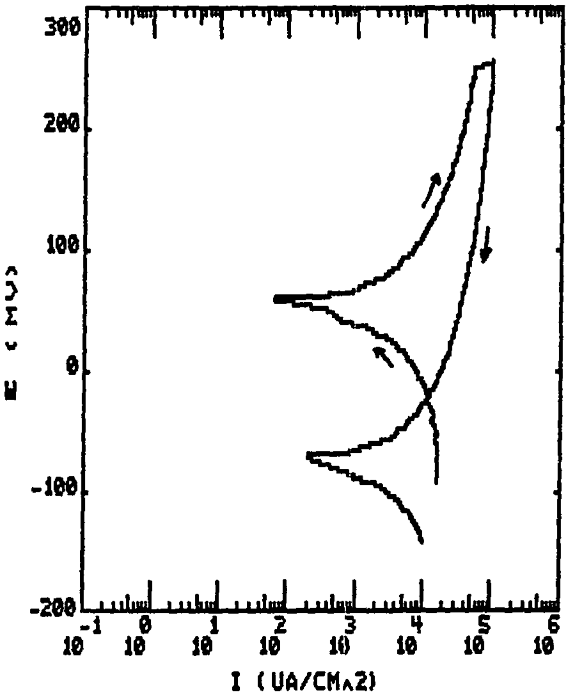

Figure 87. Cyclic polarization curve for pure copper electrode in 1 M $NaNO_3$ + 0.05 M $Cu(NO_3)_2$ solution at 25°C

initiation stage in SCC process. Recently, Gouda et al. [126] supported the anodic dissolution model, and concluded that the SCC of α-brass (in nonammoniacal solutions) is critically influenced by the oxidizing power of the solution. In the present work, the time-to-crack in nonammoniacal solutions decreases with the increasing oxidizing power of the solution.

The stress corrosion cracking in nontarnishing solutions will be initiated when very narrow zones of stressed "disarranged metal" dissolve anodically in preference to stressed "well-ordered metal" to produce sub-microscopic fissures which act as local stress raisers [12]. The grain boundaries represent regions of highest dislocation density in strained alloys containing cellular dislocation structures (Zn<18%); thus, the SCC mode is intergranular. On the other hand, when planar dislocation arrays are formed, the dislocation pile-ups represent the paths of greatest dislocation density (Zn>18%), and the SCC mode is transgranular, which corresponds to the present case of $\alpha\beta^{1}$-brass (60/39) in nontarnishing solutions. The dislocation pile-ups will be the anode in the dissolution process while other surrounding surfaces will be the cathode. The existence of a large unstressed area next to a small stressed one favors the advance of the crack. Moreover, stress intensification at the crack tip increases the atomic separation and consequently reduces the activation polarization energy required for anodic dissolution. The corrosion at the crack tip will be favored over attack elsewhere. The mechanism shows clearly the importance of dissolution process for both initiation and propagation stages.

Brittle mechanical failure by adsorption model

This mechanism applies in solutions where the corrosion rate is too small to satisfy the dissolution mechanism requirements, as in nitrite and ammonium nitrate solutions. The transgranular SCC of brass in nitrite solution was studied by several authors [69-71]. Gouda et al. [127] and Jones [125] found that nitrite is a corrosive inhibitor for zinc dissolution. Accordingly, SCC in nitrite solution cannot occur by any mechanism based on electrochemical dissolution [128]. The present detailed study of SCC of $\alpha\beta'$-brass (60/39) in ammonium nitrate solution reveals the following features:

1. Very low corrosion rate, as proved by Tafel plot calculations
2. Lack of conditions required for cyclic polarization curve to predict SCC by a dissolution mechanism
3. Slight change in the SCC fracture surface, as revealed by EDAX results

These features may be in favor of the brittle mechanical failure mechanism. Failure can be attributed to the adsorption model, where specific species adsorb on and interact with strained bonds at the crack tip, causing a reduction in bond strength and permitting brittle fracture [45]. The adsorption model was adopted strongly by Sircar et al. [129], who suggested that cracking pattern is dependent mainly on the situation existing at the surface or the interfaces of a corroding material and the environment, and that the conventional reactions of dissolution are of secondary importance in the cracking process, while adsorption plays a major role. Moreover, the production of NH_4^+ ions, by cathodic reduction of nitrite and nitrate anions, was reported before [69,130]. Consequently, it can be assumed that NH_4^+ ions are the specific species being adsorbed on the surface during the SCC process.

Finally, it should be noted that there is no sharp boundary between the two mechanisms discussed above. Instead, there might be a region (of corrosion rate values) where a conjoint action of both mechanisms can be assumed.

SUMMARY

The stress corrosion cracking (SCC) susceptibility of pure copper and two brass (copper-zinc alloy) compositions (80/20 and 60/39), was studied in several ammoniacal and nonammoniacal aqueous solutions at open circuit potential applying a constant load technique. The SCC tests, using tensile stress and loop specimens, showed pure copper to be immune in all solutions tested, the $\alpha\beta'$-brass (60/39) alloy to be most susceptible to SCC, and the (80/20) alloy to have intermediate SCC susceptibility. The electrochemical tests (corrosion potential and Tafel plots) have been utilized to prove the validity of the dissolution mechanism for the SCC propagation in solutions with intermediate corrosion rates ($\sim 0.1 < i_{cor} < \sim 5$ mA/cm^2). The electrochemical tests were also used to predict the preferential dissolution of zinc (dezincification) in noncomplexing solutions, and the higher dissolution of copper (than that of zinc) in complexing solutions. The formation of intermediate cuprous complexes was detected using a rotating ring disc electrode (RRDE) composed of a brass (80/20) disc and platinum ring, in ammonium chloride-cupric chloride solution. Moreover, a mathematical model for the role of cuprous complexes in copper corrosion was developed for the proposed autocatalytic oxidation mechanism. Finally, the predictions of dezincification and decuprification were confirmed by energy dispersive x-ray analysis (EDAX). The dissolution mechanism was further supported by the scanning electron microscopy (SEM) results which showed the absence of any true cleavage features on the SCC frac-

ture surface in ammoniacal copper sulfate solution (Mattsson's solution) at pH=10.9.

At very low corrosion rates, the stress corrosion cracking (if present) is assumed to operate by the brittle mechanical fracture mechanism in solutions where ammonium ions (NH_4^+) can be generated, as in cathodic reduction of nitrite solution. The cracking is assumed to propagate by adsorption and interaction of these ions with the strained bonds at the crack tip, causing reduction in bond strength and permitting brittle fracture.

The cyclic polarization technique proved to be an efficient tool to predict the SCC of brass (but not of pure copper) alloys. The hysteresis loop, in cyclic polarization curves, indicates the formation of surface pits which represent the initiation stage in the SCC process.

The optical microscopy results show that the cracking mode, in all solutions, is transgranular, which is expected for brass alloys with zinc content >18% in nontarnishing solutions.

CONCLUSIONS

1. Pure copper is immune to stress corrosion cracking (SCC) in several ammoniacal and nonammoniacal solutions, and the susceptibility of brass to SCC increases with increasing zinc content.
2. Corrosion potentials alone are insufficient to identify, predict, or monitor SCC; complete Tafel plots generating not only corrosion potentials but also anodic and cathodic polarization curves, are useful in estimating the probable cathodic and anodic reactions at the electrode surface.
3. Preferential dissolution is a requirement for SCC in nontarnishing solutions. Preferential zinc dissolution (dezincification) occurs in noncomplexing solutions, while higher dissolution of copper (than that of zinc) occurs in complexing solutions. These conclusions were predicted by the electrochemical results, and further confirmed by the surface analysis (EDAX) measurements.
4. Stress corrosion cracking, at open circuit potential in nontarnishing solutions, can be predicted from cyclic polarization measurements.
5. Stress corrosion cracking of $\alpha\beta'$-brass (60/39), in nontarnishing solutions, is transgranular. No signs of true cleavage features were observed in ammoniacal copper sulfate solution (pH=10.9) which is in accordance with dissolution mechanism.
6. A model is presented to show the role of catalytic oxidation of cuprous complexes in brass corrosion.

7. Two SCC mechanisms are assumed to operate under different conditions. The dissolution mechanism is supposed to operate when the corrosion rate is moderate. The brittle mechanical failure due to adsorption phenomena is assumed when the corrosion rate is very low and the generation of ammonium ions is possible.

LITERATURE CITED

1. Bassett, W. H. Proc. ASTM 1918, 18, 153.
2. Webster, W. R. Proc. ASTM 1918, 18, 163.
3. Merica, P. D.; Woodward, R. W. Proc. ASTM 1918, 18, 165.
4. Price, W. B. Proc. ASTM 1918, 18, 179.
5. Thompson, D. H.; Tracy, A. W. Trans AIME 1949, 185, 100.
6. Mattsson, E. Electrochimica Acta 1961, 3, 279.
7. Pourbaix, M. "Atlas of Electrochemical Equilibria in Aqueous Solutions", 1st ed.; Pergamon: London, 1966.
8. Thompson, D. H. Materials Research and Standards 1961, 1, 108.
9. Hoar, T. P.; Scully, J. C. J. Electrochem. Soc. 1964, 111, 348.
10. Takano, M.; Shimodaira, S. Trans. Jpn. Inst. Met. 1966, 7, 193.
11. Evans. U. R. "The corrosion and oxidation of metals", 6th ed.; Arnold: London, 1960, p. 899.
12. Hoar, T. P.; Booker, C. J. L. Corros. Sci. 1965, 5, 821.
13. Logan, H. L. "Stress Corrosion, NACE Basic Corrosion Course"; Brasunas, A. S., Ed.; NACE: Houston, 1978.
14. Johnson, H. E.; Leja, J. J. Electrochem. Soc. 1965, 112, 638.
15. Lahiri, A. K. Br. Corros. J. 1968, 3, 289.
16. Hoar, T. P.; Podesta, J. J.; Rothwell, G. P. Corros. Sci. 1971, 11, 231.
17. Verink, E. D., Jr.; Parrish, P. A. Corrosion 1970, 26, 214.
18. Lennox, T. J., Jr. Corrosion 1970, 26, 397.
19. Pugh, E. N.; Westwood, A. R. C. Phil. Mag. 1966, 13, 167.
20. Pugh, E. N.; Craig, J. V.; Sedriks, A. J. Proc. Conf. "Fundamental Aspects of SCC"; NACE: Houston, 1969, p. 118.

21. Booker, C. J. L. Proc. Conf. "Fundamental Aspects of SCC"; NACE: Houston, 1969, p. 178.

22. Bhakta, U. C.; Lahiri, A. K. Br. Corros. J. 1973, 8, 182.

23. Pugh, E. N. "The Theory of Stress Corrosion Cracking in Alloys"; Scully, J. C., Ed.; NATO Sci. Aff. Div., Brussels, 1971, p. 418.

24. Forty, A. J.; Humble, P. Phil. Mag. 1963, 8, 247.

25. McEvily, A. J., Jr.; Bond, A. P. J. Electrochem. Soc. 1965, 112, 131.

26. Pickering, H. W.; Wagner, C. J. Electrochem. Soc. 1967, 114, 698.

27. Graf, L. Proc. Conf. "Fundamental Aspects of SCC"; NACE: Houston, 1969, p. 187.

28. Shimodaira, S.; Takano, M. Proc. Conf. "Fundamental Aspects of SCC"; NACE: Houston, 1969, p. 202.

29. Pickering, H. W. Proc. Conf. "Fundamental Aspects of SCC"; NACE: Houston, 1969, p. 159.

30. Green, J. A. S.; Mengelberg, H. D.; Yolken, H. T. J. Electrochem. Soc. 1970, 117, 433.

31. Kermani, M.; Scully, J. C. Corros. Sci. 1978, 18, 883.

32. Kermani, M.; Scully, J. C. Corros. Sci. 1979, 19, 89.

33. Kermani, M.; Scully, J. C. Corros. Sci. 1979, 19, 111.

34. Heidersbach, R. H., Jr.; Verink, E. D., Jr. Corrosion 1972, 28, 397.

35. Parkins, R. N. Br. Corros. J. 1972, 7, 15.

36. Burstein, G. T.; Hoar, T. P. Corros. Sci. 1978, 18, 75.

37. Jenkins, L. H.; Durham, R. B. J. Electrochem. Soc. 1970, 117, 768.

38. Leidheiser, H.; Kissinger, R. Corrosion 1972, 28, 218.

39. Brown, B. F.; Fujii, C. T.; Dahlberg, E. P. J. Electrochem. Soc. 1969, 116, 218.

40. Procter, R. P. M.; Islam, M. Corrosion 1976, 32, 267.

41. Polan, N. W.; Popplewell, J. M.; Pryor, M. J. J. Electrochem. Soc. 1979, 126, 1299.

42. Pinchback, T. R.; Clough, S. P.; Heldt, L. A. Metall. Trans., A 1975, 6A, 1479.

43. Gabel, H.; Beavers, J. A.; Woodhouse, J. B.; Pugh, E. N. Corrosion 1976, 32, 253.

44. Pinchback, T. R.; Clough, S. P.; Heldt, L. A. Metall. Trans., A 1976, 7A, 1241.

45. Pugh, E. N. "The Stress Corrosion Cracking of Copper Alloys", NATO ASI Ser. E., Appl. Sci., No. 30; Sijthoff and Noordhoff: The Netherlands, 1979, p. 177.

46. Burstein, G. T.; Newman, R. C. Corrosion 1980, 36, 225.

47. Roberts, E. F. I. Corros. Sci. 1981, 21, 177.

48. Parthasarathi, A.; Polan, N. W. Metall. Trans., A 1982, 13A, 2027.

49. Newman, R. C.; Burstein, G. T. Corrosion 1984, 40, 201.

50. Blanchard, W. K.; Koss, D. A.; Heldt, L. A. Corrosion 1984, 40, 101.

51. Bertocci, U.; Thomas, F. I.; Pugh, E. N. Corrosion 1984, 40, 439.

52. Johnson, H. E.; Leja, J. Corrosion 1966, 22, 178.

53. Uhlig, H. H. Proc. Conf. "Fundamental Aspects of SCC"; NACE: Houston, 1969, p. 86.

54. Uhlig, H. H.; Gupta, K.; Liang, W. J. Electrochem. Soc. 1975, 122, 343.

55. Mai, Y. W. Corrosion 1976, 32, 336.

56. Meletis, E. I.; Hochman, R. F. Corros. Sci. 1984, 24, 843.

57. Beavers, J. A.; Pugh, E. N. Metall. Trans., A 1980, 11A, 809.

58. Bertocci, U. "Embrittlement by the localized crack environment", Gangloff, R. P., Ed.; AIME: New York, 1984, p. 49.

59. Green, J. A. S.; Pugh, E. N. Metall. Trans. 1971, 2, 1379.

60. Pickering, H. W.; Byrne, P. J. Corrosion 1973, 29, 325.

61. Kawashima, A.; Agrawal, A. K.; Staehle, R. W. J. Electrochem. Soc. 1977, 124, 1822.

62. Pinchback, T. R.; Clough, S. P.; Heldt, L. A. Corrosion 1976, 32, 469.

63. Vértes, A.; Pchelnikov, A. P.; Losev, V. V.; Suba, M.; Lakatos, M. V.; Nagy, I. C. Radiochem. Radioanal. Lett. 1982, 53, 167.

64. Polunin, A. V.; Pchelnikov, A. P.; Zakharin, D. S.; Losev. V. V.; Marshakov, I. K. Zasch. Met. 1982, 18, 402.

65. Syrett, B. C.; Parkins, R. N. Corros. Sci. 1970, 10, 197.

66. Kawashima, A.; Agrawal, A. K.; Staehle, R. W. "Stress Corrosion Cracking - The Slow Strain Rate Technique," Ugiansky, G. M.; Payer, J. H., Eds.; ASTM: Philadelphia, 1979, p. 266.

67. Gouda, V. K.; El-Sayed, H. A.; Sayed, S. M.; Sherbini, G. M. Corrosion 1982, 38, 609.

68. Maria, M. S. S.; Scully, J. C. Corros. Sci. 1983, 23, 753.

69. Burstein, G. T.; Newman, R. C. Proc. Int. Symp., "Corrosion and Corrosion Protection," Frankenthal, R. P.; Mansfeld, F., Eds.; The Electrochem. Soc.: Manchester, 1981, p. 176.

70. Newman, R. C.; Sieradzki, K. Scripta Metall. 1983, 17, 621.

71. Alvarez, M. G.; Manfredi, C.; Giordano, M.; Galvele, J. R. Corros. Sci. 1984, 24, 769.

72. Parkins, R. N.; Holroyd, N. J. H. Corrosion 1982, 38, 245.

73. Pugh, E. N.; Montague, W. G.; Westwood, A. R. C. Corros. Sci. 1966, 6, 345.

74. Pugh, E. N.; Craig, J. V.; Montague, W. G. Trans. ASM 1968, 61, 468.

75. Uhlig, H. H.; Duqette, D. J. Corros. Sci. 1969, 9, 557.

76. Escalante, E.; Kruger, J. J. Electrochem. Soc. 1971, 118, 1062.

77. Pednekar, S. P.; Agrawal, A. K.; Chaung, H. E.; Staehle, R. W. J. Electrochem. Soc. 1979, 126, 701.

78. Suzuki, Y.; Hisamatsu, Y. Corros. Sci. 1981, 21, 353.

79. Brown, B. F. "Stress Corrosion Cracking Control Measures," Natl. Bur. Stand. (U.S.), 1977, No. 2616.

80. Raicheff, R. G.; Damjanovic, A.; Bockris, J. O'M. J. Chem. Phys. 1967, 47, 2198.

81. Despic, A. R.; Raicheff, R. G.; Bockris, J. O'M. J. Chem. Phys. 1968, 49, 926.

82. Haruyama, S.; Asawa, S. Corros. Sci. 1973, 13, 395.

83. Scully, J. C. Corros. Sci. 1980, 20, 997.

84. Takano, M; Teramoto, K.; Nakayama, T. Corros. Sci. 1981, 21, 459.

85. Niwa, H.; Asawa, S.; Haruyama, S.; Mori, T. Corros. Sci. 1983, 23, 959.

86. Parkins, R. N. "Proc. Conf. on SCC and H_2-Embrittlement of Iron-Base Alloys", Staehle, R. W., Ed.; NACE: Houston, 1973, 601.

87. Wagner, C.; Traud, W. Z. Elektrochemie 1938, 44, 391.

88. Stern, M. Corrosion 1958, 14, 440t.

89. Makrides, A. C. Corrosion 1973, 29, 148.

90. Bailey, J. M.; Ritchie, I. M. J. Electrochem. Soc. 1979, 126, 2285.

91. Jankowski, J.; Juchniewicz, R. Corros. Sci. 1980, 20, 841.

92. Bandy, R. Corros. Sci. 1980, 20, 1017.

93. Ishikawa, Y.; Mikada, K. Corrosion 1980, 36, 649.

94. McLaughlin, B. D. Corrosion 1981, 37, 723.

95. Lorenz, W. J.; Mansfeld, F. Corros. Sci. 1981, 21, 647.

96. Taylor, R. J.; Williams, L. F. G. Corrosion 1980, 36, 41.

97. Devereux, C. F.; Kim, K. Y. Corrosion 1980, 36, 262.

98. Greene, N. D.; Gandhi, R. H. Mat. Perform. 1982, 21, 34.

99. Barnartt, S.; Donaldson, M. Corrosion 1983, 39, 33.

100. Edeleanu, C.; Hines, J. G. Br. Corros. J. 1983, 18, 6.

101. Hines, J. G. Br. Corros. J. 1983, 18, 10.

102. Cleland, J. H.; Edeleanu, C. Br. Corros. J. 1983, 18, 15.

103. Nuttall, D. F.; Linton, A.; Stevens, R. L. Corros. Sci. 1984, 24, 863.

104. Stern, M.; Geary, A. L. J. Electrochem. Soc. 1957, 104, 56.

105. Britz, D.; Hougaard, P. Corros. Sci. 1983, 23, 987.

106. Pugh, E. N.; Green, J. A. S. Metall. Trans. 1971, 2, 3129.

107. Sircar, S. C.; Chatterjee, U. K.; Sherbini, G. M. Corros. Sci. 1983, 23, 777.

108. Sedzimir, J.; Bujanska, M. Corros. Sci. 1980, 20, 1029.

109. Lees, D. J.; Hoar, T. P. Corros. Sci. 1980, 20, 761.

110. Chatterjee, U. K.; Goswami, S. K.; Sircar, S. C. Trans. Ind. Inst. Met. 1980, 33, 76.

111. Skoulikidis, T. N.; Vassilious, P. G. Br. Corros. J. 1982, 17, 142.

112. Stern, M. J. Electrochem. Soc. 1957, 104, 645.

113. Smyrl, W. H. "Comprehensive Treatise of Electrochemistry", Bockris, Conway, Yeager, White, eds.; Plenum: New York, 1981, Vol. 4, p. 108.

114. Bockris, J. O'M.; Reddy, A. K. N. "Modern Electrochemistry"; Plenum: New York, 1970, Vol. 2, p. 1293.

115. Verink, E. D., Jr. "Electrochemical Techniques for Corrosion", Baboian, R., Ed.; NACE: Houston, 1978, p. 43.

116. Corapcioglue, M. O. Ph.D. Dissertation, University of Delaware, Newark, 1984.

117. Mattsson, E.; Bockris, J. O'M. Trans. Farad. Soc. 1959, 55, 1586.

118. Bjerrum, J. "Stability Constants of Metal Ion Complexes"; The Chemical Soc.: London, 1958, part II.

119. Hansen, R. S. Department of Chemistry, Iowa State University, unpublished communication.

120. Wilde, B. E. *Corrosion* 1972, 28, 283.

121. Walker, M. S.; Rowe, L. C. "Electrochemical Techniques for Corrosion", Baboian, R., Ed.; NACE: Houston, 1978, p. 79.

122. Parkins, R. N. *Corros. Sci*. 1980, 20, 147.

123. Holroyd, N. J. H.; Parkins, R. N. *Corros. Sci*. 1980, 20, 707.

124. Broek, D. "Elementary Engineering Fracture Mechanics", 2nd ed.; Sijthoff & Noordhoff: The Netherlands, 1978, Chapter 2.

125. Jones, D. A. *Corrosion* 1984, 40, 181.

126. Gouda, V. K.; El-Sayed, H. A.; Sherbini, G. M. *Br. Corros. J*. 1983, 18, 40.

127. Gouda, V. K.; Khedr, M. G. A.; Shams Eldin, A. M. *Corros. Sci*. 1967, 7, 221.

128. Gouda, V. K.; Ramadan, A. A.; Youssef, G. I. *Br. Corros. J*. 1983, 18, 76.

129. Sircar, S. C.; Chatterjee, U. K.; Zamin, M.; Vijayendra, H. G. *Corros. Sci*. 1972, 12, 217.

130. Newman, R. C.; Burstein, G. T. *J. Electrochem. Soc*. 1980. 127, 2527.

ACKNOWLEDGMENTS

I owe a host of debts to many people for their help with this work.

I am very grateful to Professor R. S. Hansen for counsel and guidance in this work.

It is a pleasure to acknowledge helpful discussions with Professor Dennis Johnson and Professor Otto Buck. Special acknowledgment is made to Professor B. C. Gerstein and Professor C. Y. Ng.

I am particularly grateful to Dr. K. G. Baikerikar for his continuous and effective help during the work. My thanks are also due to Dr. Al Bevolo for performing the EDAX analysis.

I would like to thank Mr. J. Wheelock, Mr. H. Amenson, Mr. L. Reed, and Mr. H. Baker, in the metal development department, for casting, machining and metallographic services.

I thank friends R. Ranjan, P. Kayima, Tom Lloyd, and Linda Siemsen for their help, interest and companionship.

I also thank Maggie Wheelock for her fast, neat and excellent typing.

My thanks also are due to Ames Laboratory for providing the full financial support for the work.

Finally, I am indebted to my family for all that they are and do.

APPENDIX A.

THEORETICAL BASICS OF POTENTIAL/pH DIAGRAM CONSTRUCTION

According to Pourbaix [7], chemical reactions are written in the form: $\Sigma\nu_iM_i=0$, where the stoichiometric coefficients, ν, are positive for the reacting substances, M, on the right-hand side of the reaction equation and negative for those on the left-hand side. Similarly, the electrochemical reactions are written in the form: $\Sigma\nu_iM_i + ne^- = 0$. The condition for thermodynamic equilibrium of a chemical reaction is:

$$\Sigma\nu_i\mu_i = 0, \text{ where } \mu_i = \mu_i{}^\circ + RT\ \ln(M_i)$$

μ_i: chemical potential of reacting substance, M_i
$\mu_i{}^\circ$: standard chemical potential of M_i
(M_i): activity or fugacity of M_i

So,

$$\Sigma\nu_i\mu_i = 0 = \Sigma\nu_i\mu_i^\circ + RT\ \Sigma\nu_i\ln(M_i)$$

$$= \Sigma\nu_i\mu_i^\circ + 4.575\ T\ \Sigma\nu_i\ \log\ (M_i)$$

So,

$$\Sigma\nu_i\ \log\ (M_i) = -\frac{\Sigma\nu_i\mu_i{}^\circ}{4.575T}$$

if $\Sigma\nu_i\ \log\ (M_i) = \log K$, then: $\log K = \frac{-\Sigma\nu_i\mu_i{}^\circ}{4.575\ T}$

At T = 298.1°K:

$$\log K = \frac{-\Sigma\nu_i\mu_i^\circ}{1363} \ldots \qquad (1)$$

where μ_i°: standard chemical potential at 25°C, in cal.

K: equilibrium constant.

Similarly, for electrochemical reaction, the condition for thermodynamic equilibrium will be:

$$E_o = E_o^\circ + \frac{0.0591}{n}\Sigma\nu_i\log(M_i) \ , \qquad E_o^\circ = \frac{\Sigma\nu_i\mu_i^\circ}{23060n} \qquad (2)$$

where E_o = equilibrium potential of the reaction

E_o° = standard equilibrium potential at 25°C.

To construct the potential/pH diagram of a metal (e.g., copper) in some system (e.g., water), all the possible reactions of copper with water are written down, then the condition for thermodynamic equilibrium of each reaction is expressed in the form of equation (1) or (2) according to the reaction nature. Substituting the numerical values of μ_i° and E_o°, the derived equations will be expressed in potential and/or pH terms and can be represented graphically on a potential/pH diagram.

APPENDIX B

CHEMICAL REACTIONS OF $Cu-NH_3-H_2O$ AND $Zn-NH_3-H_2O$ SYSTEMS [6]

Copper. The basic standard electrode potentials and the equilibrium constants used in the calculations are:

$$Cu^{2+} + 2e^- = Cu; \qquad E_H^0 = 0{\cdot}337\ V$$

$$Cu^{+} + e^- = Cu; \qquad E_H^0 = 0{\cdot}521\ V$$

$$Cu^{2+} + e^- = Cu^{+}; \qquad E_H^0 = 0{\cdot}153\ V$$

$$\frac{[NH_3][H^+]}{[NH_4^+]} = 5{\cdot}50 \times 10^{-10}$$

$$\frac{[Cu^+][NH_3]^2}{[Cu(NH_3)_2^+]} = 1{\cdot}38 \times 10^{-11}$$

$$\frac{[Cu^{2+}][NH_3]^4}{[Cu(NH_3)_4^{2+}]} = 2{\cdot}35 \times 10^{-13}$$

$$[Cu^+][OH^-] = 1{\cdot}26 \times 10^{-15}$$

$$[Cu^{2+}][OH^-]^2 = 1{\cdot}52 \times 10^{-20}$$

$$[Cu^{2+}][SO_4^{2-}]^{0{\cdot}25}[OH^-]^{1{\cdot}5} = 1{\cdot}30 \times 10^{-16}$$

From these constants the following equilibrium equations are obtained:

(1) $Cu^{2+} + e^- = Cu^+$

$$E_H = 0{\cdot}153 + 0{\cdot}0591 \log \frac{[Cu^{2+}]}{[Cu^+]}$$

(2) $Cu^{2+} + 2NH_4^+ + e^- = Cu(NH_3)_2^+ + 2H^+$

$$E_H = -0{\cdot}300 + 0{\cdot}118 \log [NH_4^+] + 0{\cdot}118\ pH + 0{\cdot}0591 \log \frac{[Cu^{2+}]}{[Cu(NH_3)_2^+]}$$

(3) $Cu(NH_3)_4^{2+} + 4H^+ = Cu^{2+} + 4NH_4^+$

$$pH = 6{\cdot}10 - \log [NH_4^+] - 0{\cdot}25 \log \frac{[Cu^{2+}]}{[Cu(NH_3)_4^{2+}]}$$

(4) $Cu(NH_3)_4^{2+} + 2H^+ + e^- = Cu(NH_3)_2^+ + 2NH_4^+$

$$E_H = 1{\cdot}143 - 0{\cdot}118 \log [NH_4^+] - 0{\cdot}118\ pH + 0{\cdot}0591 \log \frac{[Cu(NH_3)_4^{2+}]}{[Cu(NH_3)_2^+]}$$

(5) $Cu(NH_3)_2^+ + 2H^+ = Cu^+ + 2NH_4^+$

$$pH = 3{\cdot}83 - \log [NH_4^+] - 0{\cdot}50 \log \frac{[Cu^+]}{[Cu(NH_3)_2^+]}$$

(6) $Cu^{2+} + 2e^- = Cu$

$$E_H = 0{\cdot}337 + 0{\cdot}0295 \log [Cu^{2+}]$$

(7) $Cu^{2+} + 0{\cdot}5H_2O + e^- = 0{\cdot}5Cu_2O + H^+$

$$E_H = 0{\cdot}206 + 0{\cdot}0591\ pH + 0{\cdot}0591 \log [Cu^{2+}]$$

(8) $Cu(SO_4)_{0{\cdot}25}(OH)_{1{\cdot}5} + 1{\cdot}5H^+ = Cu^{2+} + 0{\cdot}25SO_4^{2-} + 1{\cdot}5H_2O$

$pH = 3{\cdot}41 - 0{\cdot}67 \log [Cu^{2+}] - 0{\cdot}17 \log [SO_4^{2-}]$

(9) $Cu(SO_4)_{0{\cdot}25}(OH)_{1{\cdot}5} = CuO + 0{\cdot}25SO_4^{2-} + 0{\cdot}5H^+ + 0{\cdot}5H_2O$

$pH = 6{\cdot}14 + 0{\cdot}50 \log [SO_4^{2-}]$

(10) $Cu(SO_4)_{0{\cdot}25}(OH)_{1{\cdot}5} + 4NH_4^+ = Cu(NH_3)_4^{2+} + 0{\cdot}25SO_4^{2-} + 2{\cdot}5H^+ + 1{\cdot}5H_2O$

$pH = 7{\cdot}73 - 1{\cdot}6 \log [NH_4^+] + 0{\cdot}40 \log [Cu(NH_3)_4^{2+}] + 0{\cdot}10 \log [SO_4^{2-}]$

(11) $CuO + 4NH_4^+ = Cu(NH_3)_4^{2+} + 2H^+ + H_2O$

$pH = 8{\cdot}11 - 2 \log [NH_4^+] + 0{\cdot}50 \log [Cu(NH_3)_2^+]$

(12) $Cu(SO_4)_{0{\cdot}25}(OH)_{1{\cdot}5} + 0{\cdot}5H^- + e^- = 0{\cdot}5Cu_2O + 0{\cdot}25SO_4^{2-} + H_2O$

$E_H = 0{\cdot}449 - 0{\cdot}0295pH - 0{\cdot}0149 \log [SO_4^{2-}]$

(13) $CuO + H^+ + e^- = 0{\cdot}5Cu_2O + 0{\cdot}5H_2O$

$E_H = 0{\cdot}690 - 0{\cdot}0591pH$

(14) $0{\cdot}5Cu_2O + H^+ + e^- = Cu + 0{\cdot}5H_2O$

$E_H = 0{\cdot}468 - 0{\cdot}0591pH$

(15) $0{\cdot}5Cu_2O + 2NH_4^+ = Cu(NH_3)_2^+ + H^+ + 0{\cdot}5H_2O$

$pH = 8{\cdot}56 - 2 \log [NH_4^+] + \log [Cu(NH_3)_2^+]$

(16) $Cu(NH_3)_2^+ + 2H^+ + e^- = Cu + 2NH_4^+$

$E_H = 0{\cdot}974 - 0{\cdot}118 \log [NH_4^+] - 0{\cdot}118pH + 0{\cdot}0591 \log [Cu(NH_3)_2^+]$

Zinc. The basic standard electrode potential and the equilibrium constants used in the calculations are:

$$Zn^{2+} + 2e^- = Zn; \qquad E_H^0 = -0{\cdot}763 \text{ V}$$

$$\frac{[Zn^{2+}][NH_3]^4}{[Zn(NH_3)_4^{2+}]} = 9{\cdot}8 \times 10^{-10}$$

$$[Zn^{2+}][OH^-]^2 = 1{\cdot}2 \times 10^{-17}$$

From these constants the following equilibrium equations are derived:

(17) $Zn^{2+} + 2e^- = Zn$

$E_H = -0{\cdot}763 + 0{\cdot}0295 \log [Zn^{2+}]$

(18) $Zn(OH)_2 + 2H^+ = Zn^{2+} + 2H_2O$

$pH = 5{\cdot}54 - 0{\cdot}50 \log [Zn^{2+}]$

(19) $Zn(OH)_2 + 4NH_4^+ = Zn(NH_3)_4^{2+} + 2H^+ + 2H_2O$

$pH = 8{\cdot}48 - 2 \log [NH_4^+] + 0{\cdot}50 \log [Zn(NH_3)_4^{2+}]$

(20) $Zn(OH)_2 + 2H^+ + 2e^- = Zn + 2H_2O$

$E_H = -0{\cdot}436 - 0{\cdot}0591pH$

(21) $Zn(NH_3)_4^{2+} + 4H^+ + 2e^- = Zn + 4NH_4^+$

$E_H = 0{\cdot}065 - 0{\cdot}118 \log [NH_4^+] - 0{\cdot}118pH + 0{\cdot}0295 \log [Zn(NH_3)_4^{2+}]$

APPENDIX C.

STABILITY CONSTANTS OF Cu^{+}, Cu^{++}, AND Zn^{++} IONS IN VARIOUS COMPLEXING SOLUTIONS AT 25°C [118]

Ligand	log (stability constant)		
	Cu^{+}	Cu^{++}	Zn^{++}
NH_4^{+}	$B_2 = 8.74$	$B_4 = 14.14$	$B_4 = 9.58$
$P_2O_7^{-4}$	$B_2 = 26.72$	$B_2 = 11.87$	$B_2 = 7.24$
CN^{-}	$B_4 = 27.30$	$B_4 = 25.00$	$B_4 = 16.90$
SCN^{-}	$B_4 = 10.09$	$B_4 = 6.52$	$B_4 = 1.30$

where:

$$B_2 = \frac{[(ML_2)]^{m-2n}}{[M^{+m}][L^{-n}]^2}$$

$$B_4 = \frac{[ML_4]^{m-4n}}{[M^{+m}][L^{-n}]^4}$$

M^{+m} = metal ion with m charge

L^{-n} = ligand with n charge

APPENDIX D.

MATHEMATICAL SOLUTION OF THE DIFFERENTIAL EQUATIONS OF Cu^{+} - AND Cu^{++}-COMPLEXES GROWTH RATES

$$\frac{d[Cu^{+}]}{dt} = 4R_1 - 4k_a[Cu^{+}] + 2k_3[Cu^{++}] \tag{1}$$

$$\frac{d[Cu^{++}]}{dt} = 4k_a[Cu^{+}] - k_3[Cu^{++}] \tag{2}$$

where $[Cu^{+}] = [Cu^{++}] = 0$, when $t=0$.

Let x be the Laplace transform of $[Cu^{+}]$, and

y be the Laplace transform of $[Cu^{++}]$, then

$$Sx = \frac{4R_1}{S} - 4k_a x + 2k_3 y \tag{3}$$

$$Sy = 4k_a x - k_3 y \tag{4}$$

Solving equations (3) and (4) for x and y, then

$$x = \frac{4R_1(s+k_3)}{s[s^2 + (k_3+4k_a)s - 4k_3k_a]} , \tag{5}$$

$$y = \frac{16\ k_a R_1}{s[s^2 + (k_3+4k_a)s - 4k_3k_a]} \tag{6}$$

Define α and β by

$$(S-\alpha)(s-\beta) = s^2 + (k_3+4k_a)s - 4k_3k_a$$

i.e.,

$$\begin{matrix}\alpha \\ \beta\end{matrix} = -\frac{1}{2}\,[k_3 + 4k_a \pm \sqrt{(k_3+4k_a)^2 + 16k_3k_a}$$

let $u = \dfrac{4k_a}{k_3}$, then

$$\begin{matrix}\alpha \\ \beta\end{matrix} = \frac{-k_3}{2}\,[1 + u \pm \sqrt{1+6u+u^2} \tag{7}$$

and

$$x = \frac{4R_1(s+k_3)}{s(s-\alpha)(s-\beta)} = 4R_1\left[\frac{k_3}{\alpha\beta s} + \frac{(\alpha+k_3)}{\alpha(\alpha-\beta)(s-\alpha)} + \frac{(\beta+k_3)}{\beta(\beta-\alpha)(s-\beta)}\right] \tag{8}$$

$$y = 16\ k_aR_1\,\frac{1}{s(s-\alpha)(s-\beta)} =$$

$$= 16\ k_aR_1\left[\frac{1}{\alpha\beta s} + \frac{1}{\alpha(\alpha-\beta)(s-\alpha)} + \frac{1}{\beta(\beta-\alpha)(s-\beta)}\right] \tag{9}$$

therefore, inverting the Laplace transformations,

$$[Cu^+] = 4R_1\left[\frac{k_3}{\alpha\beta} + \frac{(\alpha+k_3)e^{\alpha t}}{\alpha(\alpha-\beta)} + \frac{(\beta+k_3)e^{\alpha t}}{\beta(\beta-\alpha)}\right], \tag{10}$$

$$[Cu^{++}] = 16\ k_aR_1\left[\frac{1}{\alpha\beta} + \frac{e^{\alpha t}}{\alpha(\alpha-\beta)} + \frac{e^{\beta t}}{\beta(\beta-\alpha)}\right. \tag{11}$$

using

$$e^{\alpha t} = 1 + \alpha t + \frac{(\alpha t)^2}{2!} + \ldots$$

and similarly for $e^{\beta t}$, then

$$[Cu^+] = 4R_1[t + \frac{1}{2}(\alpha+\beta+k_3t^2+ \ldots)] \ , \qquad (12)$$

$$[Cu^{++}] = 8k_aR_1[t^2 + \frac{1}{3}(\alpha+\beta)t^3+ \ldots] \qquad (13)$$

i.e., $[Cu^+]$ is dependent on t, while
$[Cu^{++}]$ is dependent on t^2.

For

$$\begin{matrix}\alpha\\ \beta\end{matrix} = -\frac{k_3}{2}[1+u \pm \sqrt{(1+u)^2+4u}]$$

we can write

$$\begin{matrix}\alpha\\ \beta\end{matrix} = -\frac{1}{2}k_3(1+u)[1 \pm \sqrt{1+\frac{4u}{(1+u)^2}}$$

and choose

$$\alpha = \frac{1}{2}k_3(1+u)[\sqrt{1+\frac{4u}{(1+u)^2}} - 1] \qquad >0 \qquad (14)$$

$$\beta = -\frac{1}{2}k_3(1+u)[\sqrt{1+\frac{4u}{(1+u)^2}} + 1] \qquad <0 \qquad (15)$$

Hence, the $e^{\alpha t}$ terms in $[Cu^+]$ and $[Cu^{++}]$ correspond to exponential growth; this cannot go indefinitely, so the reaction will ultimately become transport limited. The terms in $e^{\beta t}$ decay exponentially and correspond to transients.

Substituting the value of u in equations (14) and (15), then

$$\alpha = \frac{4k_a k_3}{k_3 + 4k_a}$$

and $$\beta = - [k_3 + 4k_a + \frac{4k_a k_3}{k_3+4k_a}]$$

This result can be obtained easily by assuming that:

$$\sqrt{1 + \frac{4u}{(1+u)^2}} = 1 + \frac{2u}{(1+u)^2}$$

which is valid only if $\frac{4u}{(1+u)^2} << 1$.

APPENDIX E. BRIEF DISCUSSION OF ENERGY DISPERSIVE X-RAY ANALYSIS TECHNIQUE FUNDAMENTALS

When an atom is bombarded by a sufficiently energetic electron beam, an inner shell electron is ejected. Consequently, an outer shell electron (of greater energy) will fill the vacancy and an x-ray, having the energy difference, will be released. If the ejected electron is a K-shell electron, and the dropping electron is an L-shell (or M-shell), then the emitted radiation is K_α (or K_β) x-radiation. The x-ray energies (in K eV) for elements of interest in the present work are:

	K_α	K_β	L_α	L_β
Cu	8.040	8.904	9.930	0.950
Zn	8.630	9.570	1.012	1.034
O	0.525			
Fe	6.398	7.057	0.705	0.718
Sn	25.191	28.467	3.443	3.662

In the analysis results, the inner shell is mentioned next to the metal symbol (first column).

For quantitative analysis, the net intensity for each peak of interest is compared with the intensity from a pure element and a K-ratio (second column), or approximate concentration, is determined. Corrections for stopping power (Z), absorption (A) and fluorescence (F) are used to obtain the final concentration, by iteration technique, according to the equation:

$$C' = K\ ZAF$$

The process continues until the estimated concentration, C', is no longer improved by further iteration.